Expanding Thermal Plasma Deposition of Hydrogenated Amorphous Silicon for Solar Cells

Agnès Petit

The work described in this thesis was carried out at the Delft Institute of Microelectronics and Submicron Technology (DIMES), in collaboration with the Department of Applied Physics of the Eindhoven University of Technology. It was part of the research program entitled *Helianthos*, supported through the Dutch 'Economy, Ecology and Technology' program under contract EETK01019, and by Senter-Novem.

Copyright © 2006 by Agnès Petit
All rights reserved. No part of this publication may be reproduced, stored in a retrieval system, or transmitted in any form or by any means without the prior written permission of the copyright owner.

ISBN: 90-9020794-5

Printed by Febodruk B.V., Enschede, the Netherlands.

Expanding Thermal Plasma Deposition of Hydrogenated Amorphous Silicon for Solar Cells

PROEFSCHRIFT

ter verkrijging van de graad van doctor
aan de Technische Universiteit Delft,
op gezag van de Rector Magnificus prof. dr. ir. J. T. Fokkema,
voorzitter van het College voor Promoties,
in het openbaar te verdedigen

op maandag 26 juni 2006 om 10:00 uur

door

Agnès Marie Henriette Noëlle PETIT

Ingénieur Matériaux
van het 'Institut des Sciences et Techniques de l'Ingénieur de Lyon', Frankrijk
geboren te Cavaillon, Frankrijk

Dit proefschrift is goedgekeurd door de promotoren:
Prof. dr. C. I. M. Beenakker
Prof. dr. ir. D. C. Schram

Toegevoegd promotor: Dr. R. A. C. M. M. van Swaaij

Samenstelling promotie commissie:

Rector Magnificus, voorzitter
Prof. dr. C. I. M. Beenakker, Technische Universiteit Delft, promotor
Prof. dr. ir. D. C. Schram, Technische Universiteit Eindhoven, promotor
Dr. R.A.C.M.M. van Swaaij, Technische Universiteit Delft, toegevoegd promotor
Prof. dr. V. L. Dalal, Iowa State University (United States of America)
Prof. dr. P. M. Sarro, Technische Universiteit Delft
Prof. dr. R. E. I. Schropp, Universiteit Utrecht
Dr. G. J. Jongerden, Akzo Nobel

Prof. dr. M. C. M. van de Sanden heeft als begeleider in belangrijke mate aan de totstandkoming van dit proefschrift bijgedragen.

Agnès Petit,
Expanding Thermal Plasma Deposition of Hydrogenated Amorphous Silicon for Solar Cells.
Ph.D. Thesis, Delft University of Technology.

Keywords: Hydrogenated amorphous silicon, expanding thermal plasma, chemical vapor deposition, solar cells.

A mes parents,
à Erik-Jan et Mathilde

Contents

1. Introduction
1.1 Renewable energy: a response to climate change 1
1.2 Solar energy: the hydrogenated amorphous silicon case 2
1.3 Goal and outline of this thesis 8

2. ETP deposition technique, samples preparation and analysis
2.1 ETP-CVD 11
2.1.1 CASCADE deposition set-up and ETP deposition principle . . . 12
2.1.2 External rf biasing on substrate during ETP-CVD 14
2.2 Material characterization 21
2.2.1 Sample preparation 21
2.2.2 Reflection-transmission spectroscopy (RT) 21
2.2.3 Dual Beam Photoconductivity (DBP) 22
2.2.4 Activation energy and dark conductivity 23
2.2.5 Photoconductivity 24
2.2.6 Fourier Transform Infrared absorption spectroscopy (FTIR) . . . 25
2.3 Solar cell characterization 26
2.3.1 Current-voltage characterization under illumination 26
2.3.2 Spectral response measurements 28
2.3.3 Degradation experiments 28

3. Reproducibility of a-Si:H properties deposited with an expanding thermal plasma
3.1 Introduction 31
3.2 Experimental details 32
3.3 Results 33
3.3.1 Deposition history 33
3.3.2 Temperature control 35
3.3.3 Reproducibility study 38
3.4 Conclusions 40

A brief introduction to a-Si:H growth mechanism 41

4. Hydrogen injection in ETP plasma jet for fast-deposition of high-quality a-Si:H

4.1 Introduction 45
4.2 Experiment 47
4.3 Results and discussion 49
4.3.1 Comparison between a-Si:H deposited with and without H_2 in the nozzle 49
4.3.2 Pressure series 51
4.3.3 Temperature series 52
4.3.4 H_2 flow series 57
4.3.5 Film density and hydrogen bonding type in the a-Si:H network . 59
4.4 Conclusions 65

5. External rf substrate-biased ETP for deposition of high-quality a-Si:H

5.1 Introduction 69
5.2 Experimental details 70
5.3 Results 71
5.3.1 RF power series 71
5.3.2 Temperature series 76
5.4 Discussion 80
5.5 Conclusions 84

6. Microcrystalline p-type doped layer as window layer of solar cells

6.1 Introduction 87
6.2 Experimental details 88
6.3 p-doped microcrystalline silicon thin films 89
6.3.1 Crystallinity as function of layer thickness 89
6.3.2 Annealing of p-μc-Si:H thin films 90
6.4 Integration of the p-μc-Si:H layer in a solar cell 92
6.4.1 rf PE-CVD solar cells 92
6.4.2 Influence of p-μc-Si:H thickness in solar cells 94
6.4.3 Integration of the p-μc-Si:H layer in an ETP solar cell 95
6.5 Conclusions 97

7. ETP solar cells deposited at high growth rates

7.1 Introduction 101
7.2 Buffer layer 102
7.2.1 Indications of a defect-rich layer (DRL) 103
7.2.2 Simulations of a DRL and buffer layer in a-Si:H solar cells 104

7.2.3 Choice of a buffer layer 109
7.2.4 Buffer layer thickness series 113
7.3 Solar cells prepared with rf-biased ETP-CVD 114
7.3.1 Power series 114
7.3.2 Annealing series 120
7.4 Conclusions 124

8. Illumination of ETP a-Si:H and subsequent material and device degradation
8.1 Introduction 127
8.2 The Staebler-Wronski effect 128
8.3 Experimental details 132
8.4 Results and discussion 134
8.4.1 Degradation of ETP a-Si:H single layers 134
8.4.2 Degradation of solar cells with an ETP intrinsic layer 137
8.5 Conclusions 141

9. General conclusions 145

Summary 149

Samenvatting 151

List of publications related to this work 153

Acknowledgments 155

Biography 157

Chapter 1

Introduction

1.1 Renewable energy: a response to climate change

In 2001 the United Nations' Intergovernmental Panel on Climate Change (IPCC) confirmed in their assessment report that the Earth climate is changing as a result of human activities, particularly from fossil energy use, and that further change is inevitable [1]. In the past 200 years, a 31% increase in carbon dioxide (CO_2) air levels was observed, as well as a global mean surface temperature rise of 0.5°C, with an even stronger increase in night temperature, and a global sea-level increase of 10 to 15 cm. Unusual climatic events, such as El-Niño or cyclones in central America and Japan, are becoming more frequent and more intense. Fauna and flora, adapting to these climate changes, are shifting towards the poles and to elevated areas [2]. These are only few examples of the impact of climate change. As greenhouse gases (GHG) emissions involve time lags, changes resulting from these emissions will continue for many years after the maximum emission peak has been reached. In other words, the level of stabilization of atmospheric concentrations of CO_2 depends on when this peak is reached: the sooner our current dependence on fossil fuels decreases, the lower the end level of CO_2 reached and the less the impact it has on our planet.

The possible human effect on global climate change was in fact already recognized by the international community in 1997 and it led to a legally binding agreement, the

Kyoto protocol [3], which came into force in February 2005. The objective of the Kyoto agreements was to reduce worldwide emissions (among which CO_2) of developed countries in the period of 2008-2012 by at least 5% with respect to 1990 [4]. A way to implement this agreement and to reduce the GHG emissions is to shift from fossil fuel-based energy to renewable energy. The transition from conventional energy to renewable energy would permit to tackle five importance issues:

- to limit the man-induced climate change due to fossil-fuel utilization,
- to have an alternative to the finite fossil fuel supply,
- to diminish dependence on energy import,
- to give access to clean energy to everyone,
- to create global business opportunities for renewable energy and related industry, with a high employment potential.

What are renewable energies? This terminology describes diverse energy sources, which range from biomass from forestry and agricultural residues to wind and solar energy, and including hydro- and geothermal-power. Nuclear energy is not a renewable energy source, although electricity generation from uranium fission leads to no direct GHG emission. The question of radioactive waste, safety and reliability of the plants remains controversial.

In order to stabilize the level of the atmospheric CO_2 to an acceptable level, a collective as well as an individual effort has to be made. Large reductions in GHG emissions can be achieved in sectors such as construction, transport, industry, agriculture and waste management. The stimulation of research and development of renewable energy systems is crucial and several government policies already support the market development by subsidizing 'green projects' (like the 100.000 Solar Roofs programme in Germany since January 1999 [5], or the building integrated PV programs in Japan [6] and Australia [7]). The industry commitment in investing in research and bringing the results to production is necessary to make progress in the development and spreading of renewable energy. Finally, everyone in our society plays a role and small steps, such as recycling to produce less waste, use smaller or more energy efficient cars, or get more expensive but green electricity, help to pollute less and pass on a cleaner world to future generations.

1.2 Solar energy: the hydrogenated amorphous silicon case

Solar energy

The sun is an inexhaustible energy source and each year the earth receives more than 2000 times the actual human energy consumption of the planet. However, photovoltaics, i.e. electricity generated from the sun's radiation, accounts only for 0.01% of this global energy demand. These numbers show that solar energy could

become a major energy source in the future. Moreover, the combination of increasing energy demand, decline of conventional energy resources (e.g., oil and gas) and environmental consciousness raising, have led to increase the general interest in renewable energy sources and in particular in solar energy. However up to now, although extensive research has been carried out and tremendous improvement in conversion efficiency has been achieved, solar electricity production is still too expensive compared to conventional electricity production due to the costs related to solar-module fabrication. Solar panels are not only successful in space applications (satellites), but also in stand-alone applications, like portable consumer electronics, water-pumping facilities in rural areas and local electricity production in developing countries, where no grid connection is available. Ways to reduce the production costs are either to increase the efficiency of the systems or to increase the production capacity, so to reduce the production time of the solar panels. In that view, amorphous silicon (a-Si:H) solar cells are promising and various deposition techniques are being developed to obtain larger growth rates for the fabrication of the active part of thin-film photovoltaic devices. There are often technological difficulties linked to these methods, such as up-scaling or aging of set-up components. However, with expanding thermal plasma chemical vapor deposition (ETP-CVD), high deposition rates can be achieved and large-area applications have already been realized as for instance for deposition of silicon carbide coatings.

The solar spectrum

A solar cell converts the radiation from the sun, blackbody of 6000 K, into electric energy. The solar spectrum, as measured at the earth surface, is shown in figure 1.1. The sun's radiation spectrum peaks in the visible region (~ 400 to 800 nm). Various geometrical factors, such as the tilt of the earth rotational axis, its orbital motion around the sun or the sunlight incident angle, affect the light intensity on the earth surface. Moreover, the atmosphere alters the sun radiation by absorbing and reflecting selected wavelengths. The solar spectrum that strikes the earth surface at the equator at noon at the equinox is called AM1.0 (air mass 1.0), but most of the time and for most locations on the globe, sunlight actually passes through more than one air mass before reaching the earth surface. Therefore solar cells are generally characterized with a normalized spectrum, called AM 1.5 radiation, of 1000 W/m^2 or 1 sun irradiance. The light passes the atmosphere under an angle such that its path is 1.5 times the minimum distance (sun at zenith) [8]. In amorphous silicon, which has a band gap (or forbidden gap) of about 1.75 eV, only wavelengths shorter than 710 nm will be absorbed. Therefore only part of the solar spectrum can be used for conversion into electricity.

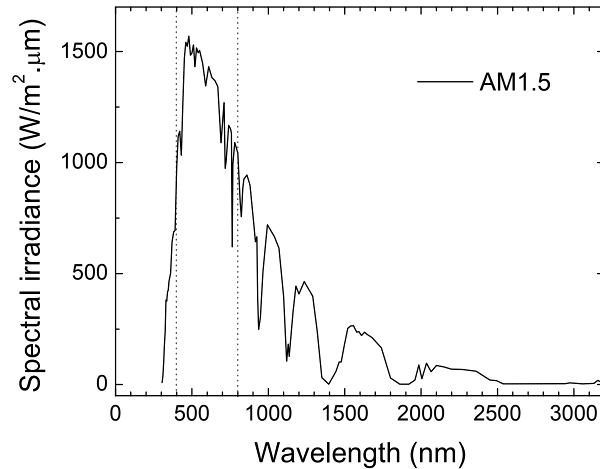

Figure 1.1: Standard terrestrial solar spectrum (AM 1.5, 1000 W/m^2). The dot vertical lines indicate the visible spectrum [9].

Hydrogenated amorphous silicon properties

A-Si:H is mainly characterized by the lack of long-range order. There is, however, still some sort of short-range order, i.e. most silicon atoms have four neighbours in a (nearly) diamond-like structure (see figure 1.2). As a result of the short-range order, a-Si:H has an energy band structure similar to that of monocrystalline silicon (c-Si) and the common semiconductor concept of conduction and valence bands can be used. The absence of long-range order, however, means that the edges of these bands are not well defined and have tails that extent into the band gap. Physically, these band tails represent energy levels of strained silicon-silicon bonds, resulting from bond-angle and/or bond-length distributions. In addition to the band tails there is a quasi-continuum of states throughout the band tails related to broken bonds, usually referred to as dangling bonds. These dangling bonds can capture charge carriers and can seriously limit the conductivity of the material. Fortunately most of these dangling bonds are passivated by hydrogen that is incorporated during the deposition process and the dangling bond density is reduced from about 10^{21} cm^{-3} in pure a-Si (amorphous silicon that contains no hydrogen) to 10^{15} cm^{-3}. However, the tail states and the dangling bonds have a large effect on the electronic properties of a-Si:H, in particular the carrier diffusion length. Another important property of a-Si:H is its direct band gap. As a result the absorption is about 50 to 100 times higher than that of c-Si, which has an indirect band gap.

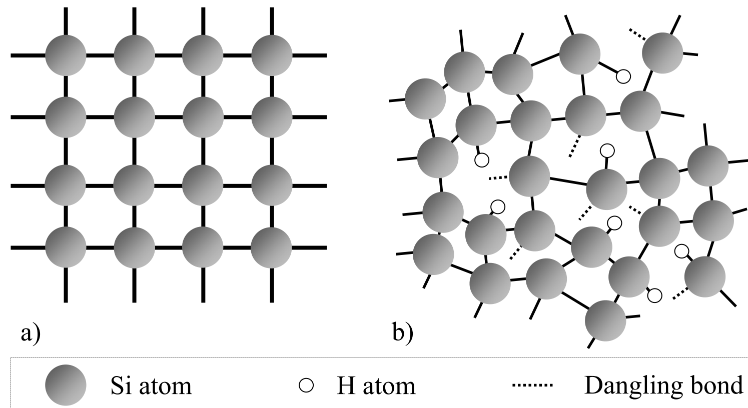

Figure 1.2: Schematic illustration of the atomic structure of crystalline (a) and amorphous (b) silicon.

Degradation and stability of a-Si:H

The creation of metastable defects is inherent to a-Si:H when the material is exposed to illumination. This is believed to originate from the breaking of weak or strained Si-Si bonds and is known as the Staebler-Wronski effect (SWE) [10]. Although the mechanism is not yet fully understood, the recombination of excess carriers as well as hydrogen seem to play a role in bond breaking and thus creation of additional dangling bonds. The newly created mid-gap states act as charge trapping and recombination centres and lead to the degradation of the material properties. The SWE is undesirable for solar cells, because these metastable defects will trap photo-generated charge carriers. As a result of this trapping process, a space charge region develops and the internal electric field is distorted, leading to a lower collection efficiency and thus to a lower solar cell performance. The conversion efficiency will eventually stabilise, at a lower value than initial. This degradation process is reversible by thermally annealing the cell at temperatures above 150°C.

Solar cell operation principle

Solar cell operation is based on the photovoltaic effect, which consists of three steps: the absorption of light (photons) that generate electron-hole pairs in the semiconductor material, the separation of the free charge carriers (electrons and holes) and finally the collection of these charge carriers. Typically, one absorbed photon leads to the generation of one electron-hole pair. The collection of the electrons and holes results in a current generation through the semiconductor device.

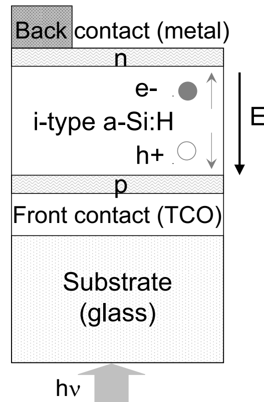

Figure 1.3: Schematic of an a-Si:H solar cell in superstrate configuration (p-i-n). The substrate used is Corning glass covered with a transparent conductive oxide (SnO_2:F). The internal electric field and the movement of the electrons and holes in the device are indicated.

A crystalline silicon solar cell consists of a p- and an n-type layer that form a p-n junction. In this case electrons are generated in the 100 to 300 μm thick and electrically neutral p-layer and diffuse towards the junction. In the depletion region near the junction the electrons drift to the n-layer under the influence of an internal electric field. Such a solar cell is called a diffusion device as the carriers reach the junction by diffusion.

An a-Si:H solar cell consists of three layers: a p-type layer, an intrinsic (undoped) layer and an n-type layer. In this case, electron-hole pairs are generated in the intrinsic layer and immediately separated by the internal electric field created by the doped layers. An a-Si:H solar cell is therefore called a drift device. In principle an a-Si:H solar cell can be made of an n-type layer on top of a p-type layer. However, the diffusion length of minority carriers (i.e., electrons in p-type material) is too low for practical operation. On the other hand, an a-Si:H solar cell can be much thinner than a c-Si cell, about 0.5 μm compared to 300 μm. This is due to the direct band gap of this material. An a-Si:H solar cell can be deposited in two ways: in the p-i-n sequence (in a superstrate configuration) or in n-i-p sequence (in a substrate configuration). A schematic drawing of the p-i-n cell is presented in figure 1.3. The substrate the most used for p-i-n devices is glass covered with a textured transparent conductive oxide (TCO). However, flexible substrates, such as plastic foils, can be used as well, depending on the process temperatures needed during the cell production. This is a major advantage of thin film technology as it opens new production modes (roll-to-roll instead of batch processing) and new application potentials for solar cells (for non-planar support). For n-i-p cells,

it is more usual to use either glass or plain stainless steel as substrate, with as front oxide an indium tin oxide (ITO) layer . In both cases, the cell will be illuminated from the p-side. As the mobility and lifetime of holes is shorter than that of electrons, it is indeed better to generate the electron-hole pairs closer to the hole-collecting electrode (p-side). Then the electrons have to travel the longest path to be collected on the n-side of the device.

The choice of a-Si:H single junction solar cells

At this time, the commercially available solar systems are, for more than 90%, from the so-called first generation technology, meaning silicon wafer-based (single or multi crystalline silicon) [11]. However, the second-generation technology, the thin film approach, is projected to have an important impact on the market in the coming decade [11]. In this technology, a thin layer of photovoltaic active material is deposited on an inexpensive substrate. In the perspective of future large-scale energy application, the choice of hydrogenated amorphous silicon (a-Si:H) as semiconductor material for solar cell applications is motivated by several reasons: silicon is abundantly available, it is not toxic and it is inexpensive as pure Si can be obtained from the microelectronics industry 'waste'. We mention three other main thin-film technologies that are developed commercially: copper-indium-diselenide (CIS), cadmium-telluride (CdTe) and organic dyes combined with nano-crystalline titanium dioxide. However, they all bring issues concerning either the raw material supply or public health and safety.

Since the discovery of a p-n junction silicon photovoltaic device, reported in 1954 by Chapin *et al.* [12], the first amorphous silicon layer deposited by Chittick *et al.* in 1969 [13], followed by the discovery of doping possibility of a-Si:H films, reported in 1975 by Spear *et al.* [14], intensive research has been carried out on silicon material and devices. Silicon is available in many forms, from single crystal to multicrystalline wafers or in ribbon for the non-thin films, and from amorphous to polycrystalline passing by microcrystalline silicon for the thin films. It is not the purpose here to make an extended overview of all these materials, so we will limit ourselves to mention some advantages and disadvantages of a-Si:H technology compared to mono-crystalline silicon technology. To start with, a-Si:H technology is associated with far less CO_2 emission than c-Si [15] because less invested energy is necessary to produce 1 Wp (Watt peak). Further a smaller amount of silicon is needed for a given power rate in comparison with c-Si. On the other hand, due to their higher efficiency, c-Si modules require smaller installed area for a given out-put power. The maximum conversion efficiency obtained so far for c-Si solar cells is 24.7% (against a theoretical maximum of 30%) [16] and that of an a-Si:H, in single junction p-i-n configuration, is 9.47% (against 24.3% in theory depending on the intrinsic layer band gap) [17]. Therefore there is plenty of room for further improvement of this technique. Another minus point related to a-Si:H is the production cost of the transparent conductive oxide (TCO) needed as electrode, the decrease of electrical transport properties upon

illumination and the low deposition rate of a-Si:H. In this thesis, we will concentrate on this last point and explore a fabrication technique, the expanding thermal plasma chemical vapor deposition technique (ETP-CVD), that leads to deposition rates at least five times higher than with conventional radio-frequency plasma enhanced CVD.

1.3 Goal and outline of this thesis

The aim of the research described in this thesis was to investigate the possibilities to grow hydrogenated amorphous silicon (a-Si:H) by expanding thermal plasma chemical vapor deposition (ETP-CVD) at high deposition rates (≥ 10 Å/s) for application in thin-film solar cells. Starting from the results obtained by Korevaar [18], the research efforts were aimed at exploring the correlation between plasma chemistry, material properties and solar cell performance.

The thesis is divided into three sections. The first section deals with the expanding thermal plasma deposition technique. In chapter 2, the deposition set-up is described, as well as the sample preparation and the analysis techniques used to characterize single layers and solar cells. Chapter 3 presents a study on the reproducibility of material deposited with ETP-CVD.

The second section relates to high rate deposition of a-Si:H by the ETP-CVD technique. The material properties are closely related to the plasma chemistry. In particular, the presence of large silicon-related species, such as cluster ions and polysilanes, can be detrimental for the opto-electronic properties of the material. Two routes are considered to reduce the influence of the ion clusters from the plasma and to improve the material properties. The first one, presented in chapter 4, relates to quenching the ion density by introducing additional hydrogen directly in the reactor chamber through the nozzle. Further in this chapter the role of hydrogen bonding in the structural properties of a-Si:H is discussed. The second examined route, investigated in chapter 5, is the application of an external rf bias on the substrate during ETP deposition. The aim is here to generate ion bombardment and therefore as one of the consequences, to increase the surface mobility of the large silicon-related species. The properties of a-Si:H deposited with rf-biased ETP-CVD versus bias voltage generated on the substrate are presented, as well as a correlation between rf bias and substrate temperature. Different processes occurring under ion bombardment are also discussed.

The third and last section concerns single junction solar cells with an ETP a-Si:H intrinsic layer. So far the deposition of high quality a-Si:H at high growth rates required elevated substrate temperatures. In the course of solar cell fabrication, this particular point can be an issue for underlying layers, most of all for the heat-sensitive p-layer. In that view, temperature-resistant microcrystalline p-layers are studied as window-layer of p-i-n junctions. This subject is developed in chapter 6. Another approach to the

problem is to reconsider the cell structure. Chapter 7 concerns the investigation of a buffer layer at the p-i interface, taking also into account that a defect-rich layer may be grown first when depositing the intrinsic layer. A reduction of substrate temperature for i-layer deposition, while maintaining the electro-optical properties of this layer, is achieved by employing an external rf bias on the substrate. The impact of ion bombardment on the solar-cell performance, as well as the implication of an annealing treatment, is studied. In these conditions, a record conversion efficiency is obtained for a single junction a-Si:H solar cell with as i-layer a high-rate ETP-CVD thin film. Finally, a-Si:H is known to be subject to degradation upon light exposure, although the opto-electric properties stabilize after a certain time and can be restored after an annealing step. In chapter 8 a short overview of the Staebler-Wronski effect on a-Si:H is given. The degradation behavior of ETP layers deposited under various conditions and that of solar cells with such a layer incorporated as i-layer is investigated.

Chapter 9 summarizes the main conclusions of this thesis and gives suggestions for future research.

References

[1] IPCC, 2001: Climate Change 2001. United Nations Intergovernmental Panel on Climate Change. Cambridge University Press, UK. Available from http://www.ipcc.ch
[2] R.E.H. Sims, Solar Energy **76** (2004) 9
[3] Kyoto protocol to the United Nations Framework Convention on Climate Change, 1-10 December 1997
[4] Internet site of the secretariat of the UNFCCC (United Nations Framework Convention on Climate Change), available from http://www.unfccc.de
[5] I.B. Hagemann, Prog. Photovolt.: Res. Appl. **12** (2004) 461
[6] J. Ohno, Prog. Photovolt.: Res. Appl. **12** (2004) 471
[7] D.K. Prasad and M. Snow, Prog. Photovolt.: Res. Appl. **12** (2004) 477
[8] R. Hulstrom, R. Bird and C. Riordan, Solar Cells **15** (1985) 365
[9] http://www.pv.unsw.edu.au
[10] D.L. Staebler and C.R. Wronski, Appl. Phys. Lett. **31** (1977) 292
[11] M.A. Green, Solar Energy **76** (2004) 3
[12] D.M. Chapin, C.S. Fuller and G.L. Pearson, J. Appl. Phys. **25** (1954) 676
[13] R. Chittick, J.H. Alexande and H.F. Sterling, J. Electrochem. Soc. **116** (1969) 77
[14] W.E. Spear and P.G. Le Comber, Solid State Com. **17** (1975) 1193
[15] R. Frischknecht, P. Hofstetter, I. Knoepfel, R. Dones and E. Zollinger, Ökoinventare für Energiesysteme, Bundesamt für Energiewirtschaft (1994)
[16] K.L.Chopra, P.D. Paulson and V. Dutta, Prog. Photovolt.: Res. Appl. **12** (2004) 69

[17] A.V. Shah, H. Schade, M. Vanecek, J. Meier, E. Vallat-Sauvain, N. Wyrsch, U. Kroll, C. Droz and J. Bailat, Prog. Photovolt.: Res. Appl. **12** (2004) 113
[18] B.A. Korevaar, Ph.D. thesis, Eindhoven University of Technology (2002)

Chapter 2

ETP deposition technique, samples preparation and analysis

In this chapter, the experimental methods and settings used throughout this thesis are presented. In the first section, a description of the CASCADE set-up and the principle of expanding thermal plasma chemical vapour deposition (ETP-CVD) are given. Section 2.2 describes the analytical techniques used to characterize hydrogenated amorphous silicon (a-Si:H) layers, while section 2.3 aims at the presentation of the device characterization techniques.

2.1 ETP-CVD

The ETP-CVD technique was originally developed by the group Equilibrium and Transport in Plasmas of the Eindhoven University of Technology (TU/e) in order to make depositions at high rates and to study the plasma chemistry [1]. It has been demonstrated that this deposition technique is suitable for the deposition of amorphous silicon nitride [2], amorphous carbon [3] and a-Si:H at high rates [4]. In particular, it appeared that the material properties of the a-Si:H layers deposited using ETP-CVD at high deposition rates (≥ 1 nm/s) were sufficiently good for implementation in thin-film solar cells. Therefore, a three-chamber deposition set-up was built in a co-operation between the solar-cell group of DIMES and TU/e. Using this deposition set-up called CASCADE (Cascaded Arc Solar Cell Apparatus Delft

Eindhoven), the feasibility of utilizing ETP-CVD for the fabrication of the intrinsic part of a-Si:H solar cells was investigated.

2.1.1 CASCADE deposition set-up and ETP deposition principle

The CASCADE deposition set-up consists of three vacuum chambers: an ETP-CVD chamber for the growth of the intrinsic layers, a radio-frequency plasma-enhanced CVD (rf PE-CVD) chamber for the deposition of doped layers and a load-lock chamber for sample (un)loading and transport between the two deposition chambers under vacuum. The ETP reaction chamber is schematically depicted in figure 2.1. The set-up has been extensively described earlier [5,6] and therefore only a short presentation will be given here.

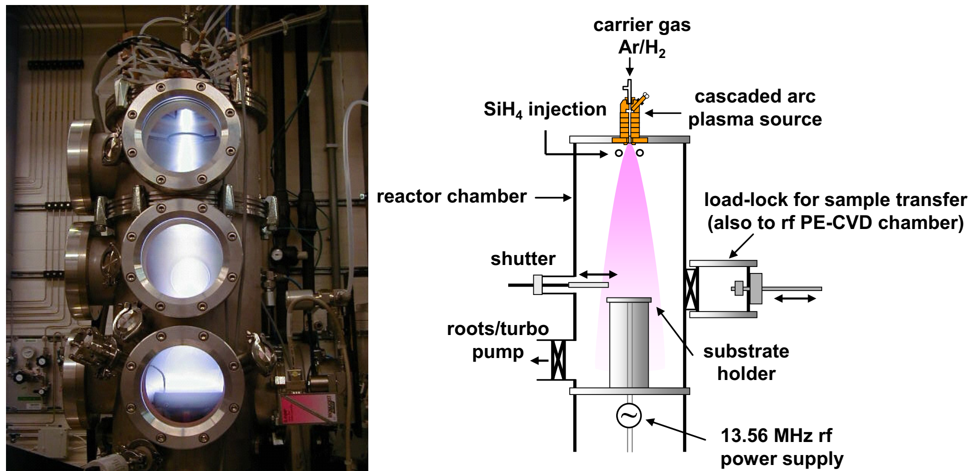

Figure 2.1: Picture and schematic of an expanding thermal plasma of pure argon at relative large pressure (~0.5 bar).

The two main parts of the ETP set-up are the high-pressure plasma source, the so-called cascaded arc, and the low-pressure deposition chamber (see figure 2.1). In ETP-CVD, the creation of the plasma, the transport, and the deposition occur separately in different parts of the set-up, which makes this technique a remote plasma technique. The dc thermal arc plasma source consists of six copper plates with a 2.5-mm diameter orifice in the centre, forming a channel for the arc discharge (see figure 2.2). The plates are water-cooled and are electrically isolated from each other by boron-nitride discs and O-rings. The plasma is created between three cathodes positioned symmetrically at the top of the arc and the grounded anode copper plate at the bottom of the arc. Non-depositing gases, such as argon and hydrogen, are used to create the plasma and the current, usually 40 A, controls the discharge. The power dissipated in the arc is typically within 5 and 8 kW. The plasma emanates from the high-pressure cascaded arc

(~ 0.5 bar) through a conical nozzle and expands into the deposition chamber, which is at a pressure of typically 0.2 mbar. Due to the large pressure difference between the arc and the chamber, the plasma is accelerated leading to a supersonic expansion. At a few centimetres from the arc outlet there is a stationary shock, after which the plasma expands sub-sonically. The reactive ionic and atomic species emanating from the arc, such as Ar^+ and H, typically have a velocity after the shock of 1000 m/s, decreasing to zero at the stagnation point.

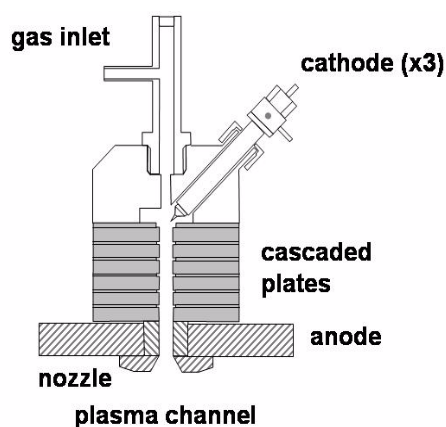

Figure 2.2: Schematic drawing of the cascaded arc, plasma source of the ETP set-up.

Next to hydrogen injection through the arc, H_2 can be also introduced directly into the reactor through the nozzle, where no power is coupled into the plasma. The precursor gas, silane, is injected through a ring located at 4.5 cm from the cascaded arc outlet (Fig. 2.1) and the distance from the source to the temperature-controlled substrate holder (ranging from 100°C to 500°C) is 43 cm. The reactor chamber has a diameter of 33 cm. During processing the system is pumped by a stack of roots blowers, whereas otherwise it is pumped by a turbo pump reaching a base pressure of ~ 10^{-6} mbar.

To induce ion bombardment during film growth, an rf-bias is applied on the substrate in addition to the ETP by means of a 13.56 MHz rf power supply. A matching network is used to match the impedance. The output of this matching network is connected to the substrate holder by the means of a copper strip. The ground of the matching box is coupled to the grounded reactor walls. A ceramic cylinder isolates the substrate holder from the rest of the reactor. Two sets of power supply and matching network were used to generate the rf signal. The first one, a Coaxial Power Systems, model RFE100, was used for the power range 4 to 15 W, while for powers ranging from 15 up to 60 W, either a Kenwood TS 440S HF transceiver, or a RFPP type RF5S. They were all used in combination with an L-type matching

network. We will refer to the former by Generator I, while the later will be called Generator II.

The doped layers are grown in the second chamber, a conventional rf PE-CVD reaction chamber. A turbo pump permits to reach a base pressure of ~ 10^{-7} mbar. The plasma is generated between two parallel electrode plates. The top electrode is grounded and serves as a temperature-controlled substrate holder, while the bottom electrode (13 cm in diameter) is connected to the RF generator via a matching network. In this way it is avoided that dust particles fall on the substrate after the plasma is turned off. Substrates of 10 cm × 10 cm can be mounted on the substrate holder. The distance between the two plates can be varied up to 27 mm.

Finally, a load-lock chamber connects the ETP and rf chambers. Substrates are loaded in the load-lock chamber, which is then pumped down to a pressure of 5 × 10^{-6} mbar before transport of these substrates to one of the deposition chambers. In that way, contamination of the deposition chambers due to atmosphere exposure (moist, oxygen) is avoided and the depositions can be carried out more rapidly as processing pressure is quickly reached. The load-lock chamber is also used as transport chamber between the ETP and the rf reactors, avoiding vacuum breaks between the deposition of the various layers of a solar cell. A more detailed description of the load-lock chamber can be found in reference 6.

2.1.2 External rf biasing on substrate during ETP-CVD

Potential profile

In plasma CVD techniques, the ions present in the plasma are accelerated by the difference between the plasma potential in the plasma bulk and the floating potential on the substrate. As ETP-CVD is a remote plasma technique, this potential difference is quite small (low electron temperature in the plasma, typically 0.1-0.3 eV, so low self-bias during deposition < 2 V) and therefore the ion energy is limited to 2 eV. To increase this ion energy, a negative bias can be applied to the substrate (in contrast to rf PE-CVD, where external substrate rf-biasing is usually used to reduce the ion bombardment [7-9]). In this way the mean energy of the bombarding ions can be controlled independently from gas phase reactions.

Originally employed for etching purposes [10-14], ion bombardment was also used in silicon deposition and ion-beam silicon epitaxy [15]. The control of the ion energy is crucial in order to balance the beneficial effects of ion bombardment from the undesirable ones. Rabalais *et al.* [16] showed that there is an optimal ion-energy window for silicon epitaxial growth depending on the substrate temperature.

In order to understand the influence of rf bias during ETP-CVD, the potential profile on the substrate holder has to be determined. The substrate holder can be considered as a large planar probe immersed in the plasma and its potential changes depending on the plasma conditions. During ETP-CVD, the substrate holder

potential, V_{sub}, equals the floating potential, V_f, and the ions are accelerated when crossing the sheath thanks to the following potential difference:

$$V_{sub} - V_p = V_f - V_p = -\frac{k_B T_e}{2e} \ln\left(\frac{m_i}{m_e}\right) \tag{1}$$

with k_B the Boltzmann constant, T_e the electron temperature and m_i and m_e the mass of the ions and electrons, respectively. Note that this equation implies that the electron and ion temperatures are equal.

When an rf voltage is applied to the substrate in combination with ETP-CVD, the substrate potential consists then of two parts: a dc voltage, V_{dc}, and an ac voltage with amplitude V_{rf} and frequency ω:

$$V_{sub}(t) = V_{dc} + V_{rf} \sin \omega t \tag{2}$$

Due to the much smaller mass and much higher mobility of the electrons compared to those of the ions, the average velocity of electrons is much greater than the average velocity of the ions and the electrons respond much faster to the rf signal than the ions. The electrons and the positive ions are in turn attracted and repelled by the substrate. As the net electrical current on the substrate holder, J, must equal zero and the collecting area being the same, the ion and the electron fluxes, J_{ion} and J_e respectively, are balanced and thus we obtain:

$$\int_0^T J dt = 0 \qquad \Rightarrow \qquad \int_0^T J_e dt = \int_0^T J_{ion} dt \tag{3}$$

with here $J = J_{ion} + J_e = \frac{1}{4} n_e v_{ion} + \frac{1}{4} n_e v_e . \exp[-e\left(V_f - V(t)\right)/kT_e]$ [17] and

$V(t) = V_{dc} + V_{rf} \sin \omega t$.

n_e is the electron density and v_{ion} and v_e are respectively the ion and the electron thermal velocity close to the substrate.

The time needed to collect the positive ion current is much longer than the time needed to collect the negative electron current (see figure 2.3). Therefore, due to this difference in velocity between the electrons and ions in the plasma, combined with the larger effective area of the grounded electrode (i.e., walls of the reactor) compared to the area of the 'powered' electrode (substrate holder), a negative potential, V_{dc}, is built up on the holder with respect to the plasma potential. Coburn *et al.* showed for modulated rf discharge sputtering that the reactor geometry plays an important role in the resulting plasma potential [18]. Confining the discharge by increasing the substrate-to-wall area ratio increases the plasma potential and the energy of the positive ions incident on the substrate.

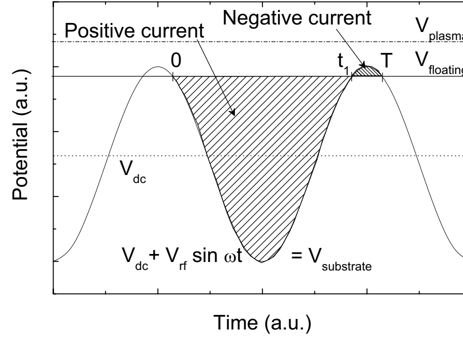

Figure 2.3: ETP potential profile on the substrate holder as a function of time when an external rf bias is applied.

When a plasma is ignited in the reactor, a dark region can be noticed around the substrate holder, called space-charge sheath or dark-plasma sheath. The sheath is divided into two regions: the positive space charge region, where the plasma potential drops rapidly to the substrate potential, and the quasi-neutral transition region at the plasma-sheath boundary (figure 2.4). The electron density drops close to the substrate holder and, as a consequence, the excitation of neutral particles drops as well. As the decay of excited particles is responsible for light generation, this explains the reduced light emission in this region and therefore the name dark-space region. The typical thickness of the space-charge sheath at the substrate holder ranges between 1 and 3 mm for an Ar-H_2-SiH_4 plasma. Figure 2.5 shows the extra plasma that is generated in the region beyond the sheath when an external rf bias is applied to the substrate for an Ar-H_2-SiH_4 plasma. Whitfield *et al.* also reported the presence of a secondary glow close to the substrate during microwave CVD when the substrate was biased [19]. Although they suggested that this glow is generated by secondary electrons arising from ion bombardment of the substrate, we think that the generation of secondary electrons in our case is limited to a few %, as the ions do not possess a very high energy (E_{ion} << 250 eV). We explain it as follows: the electron density increases mainly by electron heating when they pick up energy from the electric field while crossing the sheath.

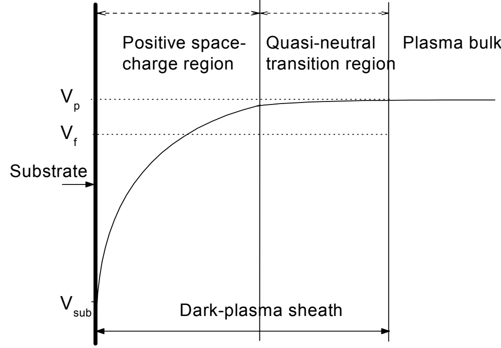

Figure 2.4: Plasma sheath developed close to the substrate holder. V_p is the plasma potential, V_f the floating potential and V_{sub} is the substrate potential.

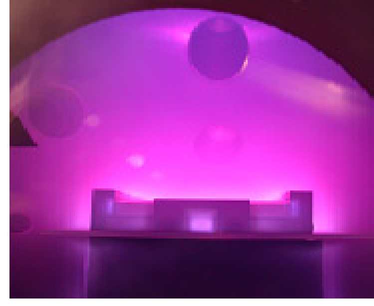

Figure 2.5: Secondary plasma around substrate holder for plasma obtained with an Ar-H_2-SiH_4 gas mixture and an external rf bias additional to ETP-CVD.

If the mean free path of the ions is larger than the sheath thickness, we can consider that the sheath is collisionless for the ions. Therefore the ions will gain an energy, E_{ion}, equal to the difference between the plasma potential, V_p, and the substrate potential, V_{sub}. In our case, knowing that $V_p - V_f$ is very small (< 2 V) and assuming that the ions respond to the time-average substrate potential, the mean ion energy becomes:

$$E_{ion} = e\left(V_p - V_{sub}\right) \approx -eV_{dc} \tag{4}$$

For each deposition condition and rf power applied, the mean ion current density, J_{ion}, can be defined as a function of the rf power and dc voltage on the substrate, with A the current collecting area. Under the assumption of no electron heating (all the power is used for biasing) and no plasma generation, the expression for the average power then becomes:

$$\langle P \rangle = \frac{1}{T}\int_0^T IV\,dt = \frac{1}{T}\int_0^T \left(J_{ion} + J_e\right)A\left(V_{dc} + V_{rf}\sin\omega t\right)dt$$

$$\langle P \rangle = \frac{A}{T}\left(J_{ion}V_{dc}T + \int_{t_1}^{T} J_e V_{rf}\sin\omega t.dt\right)$$

with $\Delta t = \left(T - t_1\right) << 1/\omega$, the second part of the right-hand side of the expression can be neglected and one can derive:

$$\langle P \rangle = J_{ion}AV_{dc} \text{ or, } P_{rf} = J_{ion}AV_{dc}. \tag{5}$$

With an rf bias applied on the substrate holder, the electron temperature increases, thus more ions are generated close to the substrate and the ion current density, J_{ion}, increases as well. The ion current density now becomes:

$$J_{ion} = en_e \sqrt{\frac{T_e}{m_{ion}}} \qquad (6)$$

In the case of a pure Ar plasma, the dc bias, V_{dc}, increases linearly with increasing rf power, P_{rf}, which means that the total rf power is used to accelerate the ions to the substrate (see figure 2.6). J_{ion} is independent from V_{dc}.

In case of a plasma consisting of a mixture of Ar, H_2 and SiH_4, the electron density in the plasma drops considerably, from ~ 10^{19} down to ~ 10^{17} m^{-3} [20]. The addition of an external rf bias on the substrate leads to an efficient heating of the electrons and a cascaded reaction occurs: the electrons lose their energy by ionizing SiH_4 and H close to the substrate, increasing the electron flux that leads to more ionization. A secondary plasma is thus generated due to the relaxation of the excited species. In the case of pure Ar plasma, the electron density was too high to be influenced by ionization and no secondary plasma was observed. When H_2 and SiH_4 are added to Ar in the plasma, V_{dc} is no longer linear with the rf power, J_{ion} depends on V_{dc} and an extra plasma appears around the substrate holder. Part of the rf power is used to generate the secondary plasma and therefore not all energy is gained by the ions. This extra plasma is not desired as it changes the plasma conditions and it reduces the bias voltage. For instance, for an Ar-H_2-SiH_4 plasma, a $|V_{dc}|$ of 39 V is obtained when 20 W are applied to the substrate holder and the calculated $|V_{dc}|$ for the same conditions but with no secondary plasma generated equals 71 V (see figure 2.6).

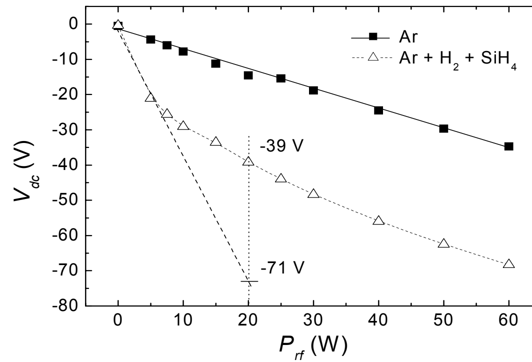

Figure 2.6: Bias voltage V_{dc} versus rf power for a pure Ar and an Ar-H_2-SiH_4 plasma. The dot line indicates the linear theoretical bias voltage that would be obtained if no secondary plasma was generated in the vicinity of the substrate in the Ar-H_2-SiH_4 plasma.

To increase the ion energy and thus the ion bombardment, it is then necessary to apply a higher power to the substrate than if no extra plasma was generated. Nevertheless, for a particular input power and bias voltage, equation (5) is still valid and the ion current density can be calculated. The energy arriving on the substrate surface per deposited atom, E_{perSi}, is obtained from V_{dc}, the ion flux, Γ_{ion}, and the Si growth flux, Γ_{Si} (Si at.cm^{-2}.s^{-1}):

$$E_{perSi} = V_{dc}.\Gamma_{ion}/\Gamma_{Si} \quad (7)$$

The amount of energy that is released at the surface is important in order to understand the effect of ion bombardment in the a-Si:H growth process. It is also important to know the ion-energy distribution. The ion-energy distribution around the average ion-energy, $e|V_{dc}|$, exhibits a series of peaks as shown by Wild *et al.* [21] in radio-frequency glow discharges and their position and intensity strongly depend on process parameters such as self-bias voltage and pressure. The presence of these peaks means that for one set of deposition conditions, high-energy ions can also be present in the plasma. These ions have detrimental effects on the film formation, such as atom displacement or even sputtering.

Influence of substrate material

With the ETP technique, depositions are performed with a floating substrate and the ions emanating from the arc arrive on the substrate with very little energy (< 2 eV, corresponds to the difference between the plasma potential and the floating potential on the substrate [4]). In that case the electrical character of the sample (insulating or conducting) hardly influences the deposition conditions. With the new substrate holder configuration, it is now possible to apply an external rf bias on the substrate to initiate ion bombardment. An rf bias is used rather than a dc bias to avoid accumulation of charge on the substrate surface when an insulating substrate is used or an insulating layer grown. With a dc bias, the surface potential of the insulating sample will differ from the applied voltage in time and finally approach the plasma potential. No acceleration of ions is then possible and the ion energy is not controlled. Therefore it is important to use an rf bias to accelerate ions and electrons in turn, so that no charge is accumulated on the surface.

If an insulating substrate is used, a capacitor is created between the plasma and the substrate holder. This leads to a potential drop across the substrate and if the substrate is too thick, part of the bias potential will not be generated between the top of the substrate and the plasma. The ions will then undergo a lower acceleration and they will not have the expected energy, which is measured on the substrate holder itself from V_{dc}. The capacitance per unit area of a glass substrate is calculated to be 7.3×10^{-8} F.m^{-2}. Considering an ion current density of 2.5 A.m^{-2} (the surface area of the current collection is estimated around 0.14 m^2) and given the frequency of the rf bias of 13.56 MHz, we can estimate a potential drop of 1 to 3 V over the Corning 1737 glass

substrate (thickness of 0.7 mm and relative permittivity of 5.7), for the power range used. For the conditions used in this study, the measured bias voltage, $|V_{dc}|$, on the substrate holder has a value between 14 and 50 V. This means that only a small potential drop occurs over the insulating substrate compared to the potential drop across the sheath, and that still 90% of the bias potential of the substrate holder is obtained on the upper surface of the substrate to accelerate the ions from the plasma. A thinner substrate or an rf power at higher frequency can be used to reduce this potential drop even further.

The c-Si substrate can be considered as conductor, as it has a low specific resistance of 10 to 30 Ω.cm and we can consider that the potential drop occurring on the silicon sample is negligible. Therefore it is possible to use both glass and c-Si substrates when applying rf substrate biasing.

Influence of generator

In figure 2.7, the dc bias voltage measured with two different combinations of rf generator / matching network box is shown versus the rf power. Generator I was used to carry out experiments at low P_{rf} (≤ 20 W), while generator II was used at higher power, namely from 15 up to 60 W.

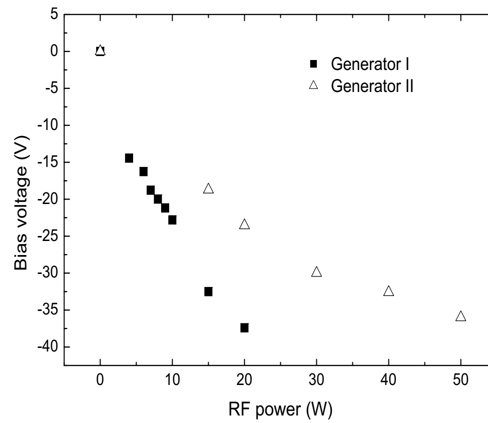

Figure 2.7: Bias voltage V_{dc} versus rf power for an Ar-H_2-SiH_4 plasma, for two different generators and matching power networks.

We can see that an off-set in V_{dc} is obtained for the same input power into the matching network depending on the generator used and the two curves do not overlap. Some power is indeed dissipated in the set-up when generator II is used, because the generator cage could not be properly grounded or shielded. For this reason we think that the bias voltage V_{dc} measured on the substrate is a more representative value of the extra energy applied to the substrate surface than the input rf power. Therefore, in

the results part, the data are plotted against the dc bias appearing on the substrate holder instead of the actual rf power.

2.2 Material characterization

2.2.1 Sample preparation

The thin films are simultaneously deposited on Corning 1737 glass substrates for optical and electric characterizations and on n-type crystalline silicon wafers for structural characterization. Both substrate types are cleaned prior to deposition following the same procedure: at least 10 min cleaning in an ultrasonic acetone bath to remove all fat substances and particles, followed by 10 min in an ultrasonic isopropanol (IPA) bath to rinse the substrates, and finally drying using a nitrogen flow to avoid that any traces of alcohol remain on the sample.

For the electric property measurements of the samples, 300-nm thick aluminium coplanar electrodes are evaporated on the surface of the a-Si:H films deposited on glass. The two rectangular shaped electrodes are 0.5 mm distant. For conductivity measurements, 20-mm long electrodes are used and for dual-beam conductivity measurements, shorter electrodes of 4 mm long are used.

2.2.2 Reflection-transmission spectroscopy (RT)

The purpose of the reflection-transmission measurement is to determine the thickness of the thin films as well as the optical parameters of a-Si:H layers, such as the refractive index, $n(h\nu)$, the absorption coefficient, $\alpha(h\nu)$, and the optical band gap, E_g.

We used a home-built reflection-transmission spectrometer, which consists of a 50 W halogen lamp as light source, a Spex 1680 B monochromator for wavelength selection, filters for suppression of the monochromator higher-order light and reduction of stray light and a beam splitter placed in front of the sample. The light enters the film from the glass side. The reflected light (R) and the transmitted light (T) are detected by two silicon photo-diodes, type K1713-03 Hamamatsu, and the absorption is defined as 1 – R – T. A calibration cycle on a bare Corning 1737 substrate, of which the wavelength-dependent refractive index is known, is carried out prior to measurement. The film thickness is calculated from the interference fringes in the reflection-transmission spectrum. From the spectral absorption of the layers in the energy range $h\nu = 1.1$ to 3.0 eV (i.e., wavelength range ~ 1130 to 420 nm), the refractive index and the absorption coefficient can be extracted [22]. In this thesis, the refractive index at 1.96 eV, n_{2eV}, will be used as an indication for the film density.

The optical band gap, E_g, is defined as the energy difference between the extended states of the valence and conduction bands, using the following expression:

$$\left(\alpha n h\nu\right)^{1/(p+q+1)} = c(h\nu - E_g) \quad (8)$$

where c is a constant and p and q are parameters related to the shape of the band edges. Equation (8) is valid for the spectrum part where α depends linearly on the photon energy. Tauc assumes that the extended states have a parabolic shape ($p = q = ½$) [23], whereas Klazes assumes a linear shape of the band edges ($p = q = 1$) [24]. The optical gap obtained according to Klazes is also called the cubic gap. The E_{04} band gap, the energy at which α reaches 10^4 cm^{-1}, is also used in literature as band gap. Although it is based on an arbitrary criterion, it has the advantage of being independent of the band-edge shape. Typical values for a-Si:H band gap are $E_{Tauc} = 1.78$ eV, $E_{Klazes} = 1.60$ eV and $E_{04} = 1.90$ eV.

2.2.3 Dual Beam Photoconductivity (DBP)

For the measurement of very low absorptions, the sensitivity of RT spectroscopy is not sufficient. These low absorptions are generally found for sub band gap photon energies. Therefore, we have measured the sub band gap absorption by dual-beam photoconductivity (DBP). With this measurement technique, the photoconductivity of a-Si:H is measured as a function of photon energy, which is proportional to the density of states distribution in the mobility gap.

The RT set-up described in the previous section was modified for DBP measurements. The light from the halogen lamp is chopped (13 Hz). The monochromator is used to select the photon energy in the range from 0.7 to 2.1 eV. A red bias light illuminates the film and generates a constant photocurrent. In this way, the recombination in the layer is fixed and the sensitivity of the method is increased. The monochromatic light generates additional carriers and this leads to a small perturbation of the conductivity. Using glass fibers the bias light and the monochromatic light are directed between two coplanar aluminium contacts on the sample surface. On these contacts a constant voltage is applied and the generated current is measured.

As DBP gives relative values for $\alpha(h\nu)$, the DBP spectrum has to be calibrated to the absolute value of $\alpha(h\nu)$ obtained from RT. The two measurements overlap in the range from 1.7 to 1.9 eV (around the optical band gap). A typical absorption coefficient spectrum is shown in figure 2.8.

Two parameters are used as a measure for the disorder: the Urbach energy, E_U, and the defect density at mid-gap, N_d. E_U is the inverse of the slope of the exponential part of the absorption spectrum and is referred to as the Urbach energy and is derived from the relation:

$$\alpha(h\nu) = \alpha_0 e^{-(h\nu - E_1)/E_U} \tag{9}$$

with α_0 and E_1 constants. The energy range in which the absorption varies exponentially represents transitions between extended and localized states in a-Si:H. As the valence band tail is much broader than the conduction band tail, the Urbach

energy is believed to be a characteristic energy for this tail. Device-quality a-Si:H has a typical E_U value of 45-50 meV.

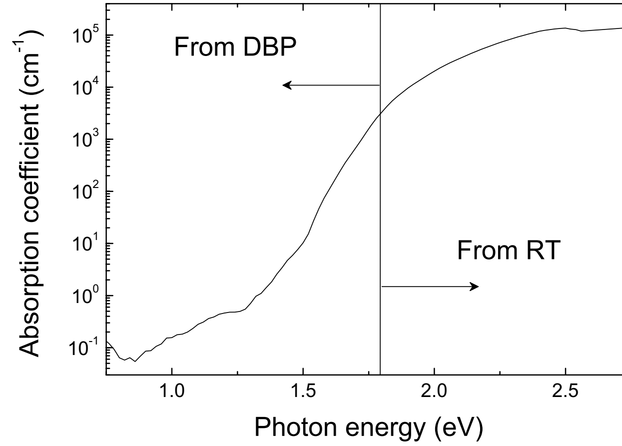

Figure 2.8: Typical absorption spectrum of a-Si:H from RT and DBP measurements.

The integration of $\alpha(h\nu)$ over the photon energy range 0.8 to 1.26 eV (absorption which originates from presumably dangling bonds) is proportional to the defect density in the mid-gap, N_d:

$$N_d = A\int_{0.8}^{1.26} \alpha(h\nu)dh\nu \tag{10}$$

with A a constant found by Jackson [25], $A = 7.9 \times 10^{15}$ eV^{-1}cm^{-2}. The integration range could be slightly extended to higher and lower energies after subtraction of the tail states absorption, but as the difference results in an error smaller than a factor two, the absorption outside the range [0.8-1.26] is neglected.

2.2.4 Activation energy and dark conductivity

The dark conductivity is proportional to the product of the mobility and the concentration of free charge carriers in the material at thermal equilibrium, as given by equation (11):

$$\sigma_D = q\left(\mu_e n + \mu_p p\right) \tag{11}$$

where q is the elementary charge, μ_e and μ_p are the electron and hole mobilities and n and p the free electron and hole concentrations, respectively.

To measure the dark conductivity, we use a Temptronic Thermo-Chuck system in combination with a Keithley 617 electrometer. The measurements are carried out on

the glass samples by applying a voltage (usually 10 V) to the coplanar Al electrodes and by measuring the current. σ_D is then obtained using the relation:

$$\sigma_D = \frac{1}{R} \cdot \frac{d}{tL} \tag{12}$$

with R the resistance of the layer ($V = RI$), d the gap between the two coplanar electrodes ($d = 0.5$ mm), L the length of the electrodes ($L = 20$ mm) and t the thickness of the layer. After a step at 130°C for 30 min to remove the impurities from the surface and anneal the Al contacts, the sample is cooled down to 60°C by steps of 5°C. σ_D is measured at each step during this cooling down, after stabilization of the temperature.

The activation energy of the dark conductivity, E_a, is derived from the temperature dependence of the dark conductivity, according to equation (13):

$$\sigma_D(T) = \sigma_0 \exp(\frac{-E_a}{kT}) \tag{13}$$

with k the Boltzmann's constant and T the temperature. The dark conductivity at room temperature is obtained by extrapolation of the measured curve to 25°C. The activation energy, E_a, is a measure of the energy difference between the Fermi level and the mobility band edge of the majority carriers. In the case of n-type material, $E_a = -(E_F - E_C)$; for p-type materials, $E_a = -(E_V - E_F)$, with E_F the Fermi level and E_C and E_V the conduction and valence band edge, respectively [26]. In doped a-Si:H, the doping efficiency, or the small fraction of the doping concentration that is electrically active, is expressed from the activation energy. For intrinsic material, E_F is supposed to be positioned in the middle of the band gap, although it is often slightly shifted towards E_C due to the asymmetry of the density of states of the valence and conduction band tails or in case of oxygen contamination for instance.

2.2.5 Photoconductivity

The photoconductivity, or light conductivity, represents the excess charge carrier concentration generated under illumination. It is related to the defect density in the material, as the charge carrier density depends on the generation and recombination rates. The photoresponse of the material is defined as the ratio between the light and the dark conductivities. Device-quality intrinsic a-Si:H has typically a photoresponse of 10^5-10^7.

We use an Oriel solar simulator to carry out the measurements on the glass samples with Al coplanar contacts. The 300 W He-Xe lamp provides an AM1.5 spectrum close to the solar spectrum at the surface of the earth and has an intensity of 100 mW.cm^{-2}. A voltage sweep is carried out from –50 V to 50 V by steps of 0.2 V and the conductivity is determined by fitting the J-V curve to a linear relationship.

2.2.6 Fourier Transform Infrared absorption spectroscopy (FTIR)

The infrared absorption properties of the films, such as the content of bonded hydrogen and the silicon-hydrogen bonding configurations, were studied by means of Fourier transform infrared absorption spectrometry. We used a Bruker Vector 22 that can operate in the 370 to 7500 cm^{-1} wave-number range. The samples were deposited on polished c-Si wafer.

From the interference fringes of the background, due to multiple reflections within the deposited film, the refractive index for infrared light and thickness of the film can be calculated. Moreover, each specific chemical bond in the material has an absorption peak in the infrared transmission spectrum, which corresponds to the vibrational mode of this bond. The density of the corresponding chemical bond, N_x, is calculated from the area of the peak, according to equation (14):

$$N_x = A_x . I_x = A_x \int \frac{\alpha(\omega)}{\omega} d\omega \tag{14}$$

with A_x the proportionality constant, I_x the integrated absorption of a given peak and $\alpha(\omega)$ the absorption coefficient.

The data processing procedure is similar to the method proposed by Langeford *et al.* [27]. In this procedure the FTIR spectrum was deconvoluted with Gaussian peaks for each absorption band at a given frequency, ω. The vibration mode at 640 cm^{-1} corresponds to the wagging absorption mode. This peak can be used to determine the total hydrogen density of the material, c_H, as every hydrogen atom bonded to the silicon network contributes to the 640 cm^{-1} peak. c_H is defined as:

$$c_H = \frac{N_H}{N_{Si} + N_H} \tag{15}$$

where N_H and N_{Si} are the hydrogen and silicon densities, respectively, and $N_{Si} + N_H \sim 5 \times 10^{22}$ cm^{-3} as established by Kessels *et al.* from ERD (Elastic Recoil Detection) analysis of ETP a-Si:H material [28].

The vibrational modes centered at ~ 1980-2010 and ~ 2070-2100 cm^{-1} correspond to the low stretching mode (LSM) and high stretching mode (HSM), respectively. These modes provide information on the structure of the amorphous network and the hydrogen bonding configurations. In a-Si:H films, the 2000 cm^{-1} mode corresponds to monohydride SiH bonding [29], whereas the 2100 cm^{-1} mode is usually associated with dihydride SiH_2 bonding [30] or clustered hydrogen and monohydride bonds on internal surfaces of voids [31], although this interpretation is still under discussion. In this way, the monohydride SiH gives rise to stretching modes both at 2000 cm^{-1} and 2100 cm^{-1} depending on its structural environment. A dominant HSM absorption is usually an indication of inferior opto-electric properties of the material. The

microstructure parameter, R^*, is a figure of merit for the structure of a material and is defined as:

$$R^* = \frac{I_{HSM}}{I_{LSM} + I_{HSM}} \quad (16)$$

where I_{LSM} and I_{HSM} are the integrated absorption strength of the low and high stretching modes, respectively. An R^* value below 0.1 is generally found in device-quality a-Si:H. Table 2.1 summarizes the hydrogen bonding types of interest for this thesis, the corresponding wave number in the FTIR spectrum, as well as the vibrational mode and proportionality constant used to calculate the bond density for each mode. These constants were chosen as determined for ETP a-Si:H material by Smets [32].

Bond type	Wave number (cm^{-1})	Vibration mode	Proportionality constant, A_x (cm^{-2})
SiH_x (all H bonded to Si)	640	Wagging	1.6×10^{19}
Isolated SiH	2000	Stretching	9.1×10^{19}
Clustered SiH and SiH_2 on void surfaces	2080-2100	Stretching	9.1×10^{19}

Table 2.1: H bond types used in this thesis and the corresponding modes of vibration

The mass density of the film, ρ, can be determined from the refractive index taken in the infrared, n_∞, and the total hydrogen content, c_H, according equation (17), and is derived from the Clausius-Mossotti relation [33]:

$$\rho = \frac{n_\infty^2 - 1}{n_\infty^2 + 2} \frac{3m_{Si}}{4\pi\left(2\alpha_{Si-Si} + \frac{c_H}{1-c_H}\left(\alpha_{Si-H} - \frac{1}{2}\alpha_{Si-Si}\right)\right)} \quad (17)$$

with m_{Si} the mass of Si atom, α_{Si-Si} the bond polarizability in the amorphous phase ($\alpha_{Si-Si} = 1.96 \times 10^{-24}\ cm^3$) and α_{Si-H} the bond polarizability of the Si-H bond ($\alpha_{Si-H} = 1.36 \times 10^{-24}\ cm^3$), according to [32]. As reference, we can remind that the mass density of crystalline silicon equals 2.33 $g.cm^{-3}$.

2.3 Solar cell characterization

2.3.1 Current-voltage characterization under illumination

The illuminated *J-V* measurements are carried out with an Oriel solar simulator equipped with an He-Xe arc lamp that produces an AM 1.5 spectrum at an intensity of 100 $mW.cm^{-2}$. It is equipped with mirrors and filters to obtain the desired spectrum and intensity. Using a Hewlett Packard 4145B parameter analyzer, the voltage is varied

from −0.5 to +0.85 V and the current is measured. The dark and light characteristics are shown in figure 2.9.

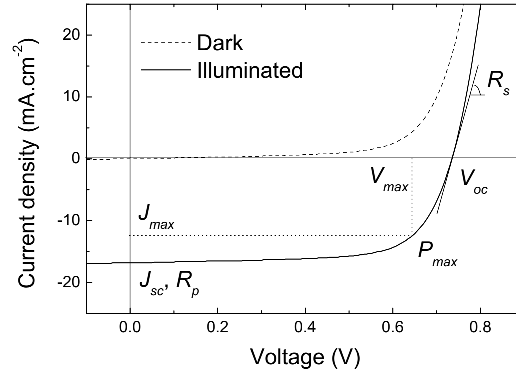

Figure 2.9: *J-V* characteristics of a p-i-n junction in the dark and under illumination.

The most important parameters that are used to characterize a solar cell are the following:

- the short-circuit current density, J_{sc}: this current density is obtained when the voltage across the device is zero;
- the open-circuit voltage, V_{oc}: this voltage is obtained when the total current equals zero. In that case the dark current and the photocurrent (that are opposite) cancel each other out.
- the fill factor, *FF*: this is the ratio of the maximum power deliverable by the cell, to the product of V_{oc} and J_{sc}:

$$FF = \frac{V_{\max} J_{\max}}{V_{oc} J_{sc}}$$

- and the energy conversion efficiency, η: this is the ratio of the maximum power output ($V_{max}.J_{max}$) to the solar power input (i.e., 100 mW/cm^2).

In practice, power losses occur in solar cells due to the resistance at the interfaces between the different layers of the cell or due to shunts. The *J-V* curve is then further characterized by the parallel resistance, R_p, which is equal to the inverse of the slope at J_{sc} and the series resistance, R_s, which is equal to the inverse of the slope at V_{oc} (see figure 2.9). As the temperature of the sample is not controlled during measurement, some inaccuracies in *J-V* measurement (estimated to be about 5%) are obtained.

2.3.2 Spectral response measurements

Spectral response measurements permit to determine the spectral sensitivity of a solar cell when the latter is illuminated under monochromatic light of a given wavelength. This measurement gives the external quantum efficiency (EQE) of the cell, which is the ratio of the number of photo-generated current that is collected, $J_L(\lambda,V)$, per flux of incident photons of energy λ, $\Phi(\lambda)$:

$$QE(\lambda) = \frac{J_L(\lambda,V)}{e\Phi(\lambda)} \tag{19}$$

The internal QE is defined as the fraction of incoming photons that generate an electron-hole pair. The internal QE is more difficult to measure than the external QE, and the latter will be smaller than the internal QE because of losses before current collection, due to e.g. recombination of carriers.

Light from a halogen lamp passes a filter wheel containing 35 band transmission filters and is incident on a solar cell. This filter wheel covers a wavelength range from 381.0 nm to 948.5 nm (3.25 to 1.31 eV). A chopper allows the use of the lock-in technique to enhance the signal-to-noise ratio. The set-up is first calibrated with a photo diode of which the QE is known. The solar cell is biased at a voltage of either −1 V, 0 V or 0.6 V.

As the penetration depth of short wavelengths is shorter than that of the long ones, the photo-carrier collection from different regions of the solar cell can be distinguished by this technique. Light from the blue part of the spectrum will generate carriers at the front of the solar cell, while red light will be absorbed throughout the whole cell and will give information about the bulk of the cell. The QE depends also on the bias voltage applied to the cell. At −1 V, all carriers are supposed to be collected as the internal electric field in the cell is large. The ratio of the external QE at 0 V bias to −1 V bias gives an indication of the depth dependence of the carrier recombination in the i-layer and deviations of this ratio from 100% indicate the amount of recombination losses at a certain wavelength.

2.3.3 Degradation experiments

The degradation of both a-Si:H single layers and p-i-n solar cells is carried out in our home-built light soaking set-up. This set-up consists of a closed box containing a temperature controlled platform at the bottom and four lamps, type Philips CSM-TP, at the top. A set of mirrors covers the walls and the top of the box in order to get an intensity of 1.5 sun +/- 0.1 on an area of ~120 cm^2 for a spectrum close to the solar spectrum. The samples are placed underneath the lamps on the platform and their temperature is maintained at 50°C thanks to a water-bath underneath the platform. The spatial homogeneity of the intensity of the set-up is checked with a calibrated

photodiode, so is also the spectrum uniformity. The solar cells are degraded under open circuit conditions.

After light soaking from several minutes to more than 1000 hours, the single layers or devices are measured again with the help of the techniques described above to establish their stability towards illumination. In our case, light conductivity is monitored for a-Si:H single layers and *J-V* characteristics under illumination is measured for solar cells.

References

[1] D.C. Schram and G.M.W. Kroesen, *Method of treating surfaces and substrates with the aid of a plasma and a reactor for carrying out the method*, American patent 4,871,580 (1989) and European patent 0297637 (1992)

[2] W.M.M. Kessels, J. Hong, F.J.H. van Assche, J.D. Moschner, T. Lauinger, W.J. Soppe, A.W. Weeber, D.C. Schram and M.C.M. van de Sanden, J. Vac. Sci. Technol. A **20** (2002) 1704

[3] J. Benedikt, R.V. Woen, S.L.M. van Mensfoort, V. Perina, J. Hong and M.C.M. van de Sanden, Diamond Relat. Mater. **12** (2003) 90

[4] W.M.M. Kessels, Ph. D. Thesis, Eindhoven University of Technology (2000)

[5] W.M.M. Kessels, R.J. Severens, A.H.M. Smets, B.A. Korevaar, G.J. Adriaenssens, D.C. Schram and M.C.M. van de Sanden, J. Appl. Phys. **89** (2001) 2404

[6] B.A. Korevaar, Ph. D. thesis, Eindhoven University of Technology (2002)

[7] L.S. Sidhu, F. Gaspari and S. Zukotynski, Mat. Res. Soc. Symp. Proc. **467** (1997) 597

[8] G. Ganguly, T. Ikeda, I. Sakata and A. Matsuda, Mat. Res. Soc. Symp. Proc. **420** (1996) 347

[9] T. Ohte, H. Aoyama, M. Goto and M. Sugawara, Jpn. J. Appl. Phys. **33** (1994) 4461

[10] G.I. Bernotas, S.V. Bruzas and A.J. Grigonis, Soviet Physics Collection **22** (1982) 83

[11] K.D. Allen and H.H. Sawin, J. Electrochem. Soc. **133** (1986) 2326

[12] M. Konuma and E. Bauser, J. Appl. Phys. **74** (1993) 62

[13] M.A. Blauw, G. Craciun, W.G. Sloof, P.J. French and E. van der Drift, J. Vac. Science & Technol. B **20** (2002) 3106

[14] T. Ono, H. Miyazaki, T. Mizutani, Y. Goto and T. Kure, Jap. J. Appl. Phys **38** (1999) 5292

[15] D. Marton, K.J. Boyd and J.W. Rabalais, J. Vac. Sci. Technol. A **16** (1998) 1321

[16] J.W. Rabalais, A.H. Al-Bayati, K.J. Boyd, D. Marton, J. Kulik, Z. Zhang and W.K. Chu, Phys. Rev. B **53** (1996) 10781

[17] G.J.H. Brussaard, Ph.D. thesis, Eindhoven University of Technology (1999)
[18] J.W. Coburn and E. Kay, J. Appl. Phys. **43** (1972) 4965
[19] M.D. Whitfield, J.S. Foord, J.A. Savage and R.B. Jackman, Diamond and Related Mat. **9** (2000) 305
[20] W.M.M. Kessels, C.M. Leewis, M.C.M. van de Sanden and D.C. Schram, J. Appl. Phys. **86** (1999) 4029
[21] C. Wild and P. Koidl, J. Appl. Phys. **69** (1991) 2909
[22] M. Trijssenaar, Ph.D. thesis, Delft University of Technology (1995)
[23] J. Tauc, R. Grigorovici and A. Vancu, Phys. Stat. Sol. **15** (1966) 627
[24] R.H. Klazes, M.H.L.M. van den Broek, J. Bezemer and S. Radelaar, Phil. Mag. B **45** (1982) 377
[25] W.B. Jackson and N. M. Amer, Phys Rev B **25** (1982) 5559
[26] W.E. Spear and P.G. Le Comber, Sol. State Comm. **17** (1975) 1193
[27] A.A. Langford, M.L. Fleet, B.P. Nelson, W.A. Langford and N. Maley, Phys. Rev. B **45** (1992) 13367
[28] W.M.M. Kessels, M.C.M. van de Sanden, R.J. Severens, L.J. van IJzendoorn and D.C. Schram, Mater. Res. Soc. Symp. Proc. **507** (1998) 529
[29] J.C. Knights, G. Lucovsky and R.J. Nemanich, J. Non-Cryst. Sol. **32** (1979) 393
[30] G. Lucovsky, R.J. Nemanich and J.C. Knights, Phys. Rev. B **19** (1979) 2064
[31] H. Wagner and W. Beyer, Solid State Commun. **48** (1983) 585
[32] A.H.M. Smets, Ph. D. thesis, Eindhoven University of Technology (2002)
[33] J.C. van den Heuvel, M.J. Geerts and J.W. Metselaar, Sol. Energy Mater. **22** (1991) 185

Chapter 3

Reproducibility of a-Si:H properties deposited with an expanding thermal plasma

3.1 Introduction

Originally, the Expanding Thermal Plasma (ETP) technique was developed by the plasma group of the Eindhoven University of Technology (TU/e) in order to study plasma chemistry. A characteristic feature of this ETP technique is that the plasma can be considered as a remote plasma, which permits plasma studies at a different position from where it is generated. It appeared that the ETP method was suitable for the deposition of hydrogenated amorphous silicon (a-Si:H) and thus could be used for the fabrication of thin-film solar cells. Since 1999, the solar cell group of the Delft University of Technology (TUD), in partnership with the TU/e, has acquired an ETP set-up. The first results were promising and solar cells with an efficiency above 4% could be initially fabricated. However, it appeared that the reproducibility of the layers, so consequently of the solar cells, deposited at the TUD varied over time.

In this chapter, we present the influence of several parameters on the quality of a-Si:H thin films and our measures to control these. In the first part, the experimental details are discussed, presenting the reference deposition conditions and the experimental procedure followed and indicating the characterization methods used. In the second part, we show the influence of unusual parameters on the performance of the ETP, such as the number of plates in the arc. In addition, we analysis the effect of an He back flow and of the heating time before deposition on the substrate

temperature. Finally, in the third part, we show in a reproducibility study that the opto-electronic properties of a-Si:H thin films deposited with the ETP technique are reproducible with a standard deviation of 5%.

3.2 Experimental details

In order to keep track of the performances of the ETP set-up, an amorphous silicon layer, chosen as reference, is regularly deposited to check both the opto-electric properties and the condition of the whole system. The gas flows used are 600 sccm of Ar, 200 sccm of H_2 and 200 sccm of SiH_4. The deposition temperature is kept fixed at 250°C. The current through the arc is 40 A, the typical voltage obtained across the arc is 160 V and the pressure in the arc between 0.41 and 0.43 mbar. The reference sample is deposited at a rate between 0.7 and 0.9 nm/s.

The a-Si:H thin films are deposited on Corning 1737 glass and on n-type crystalline silicon substrates. These substrates were cleaned following the procedure described in the experimental chapter of this thesis (paragraph 2.1).

During the growth of a-Si:H thin films, some deposition occurs not only on the substrate but also on the walls and windows of the reactor. In order to limit out-gasing from the walls and to avoid contamination, an Ar plasma is run with CF_4 injected directly in the reactor to etch the silicon away. After this cleaning run, a mixture of Ar and H_2 is used to condition the reactor. Finally, a dummy and a reference layer are deposited to check that the conditions are back to our reference level.

The samples deposited on Corning glass are used to perform Reflection-Transmission measurements to determine the thickness of the layer and the optical properties, such as the refractive index, n_{2eV}, and the optical band gap, E_{Tauc}. The latter is obtained following Tauc's expression [1]. Dual Beam Photoconductivity (DBP) is carried out in order to determine the sub-bandgap absorption, which is correlated to the density of states distribution in the mobility gap. The Urbach energy, E_U, is the characteristic energy of the exponential slope of the absorption spectrum. Light and dark conductivity measurements are also carried out on these samples. Fourier Transform Infra-Red (FTIR) absorption spectroscopy is performed on the films deposited on crystalline substrates to determine the hydrogen content, c_H, from the wagging mode at 640 cm^{-1}, and the hydrogen content of the low and high stretching modes, c_{LSM} and c_{HSM}, at respectively 2000 cm^{-1} and 2100 cm^{-1}. These parameters give information on the structure of the material. The mass density $\rho_{a\text{-}Si:H}$ of the thin films is determined according to the Clausius-Mossotti equation [2].

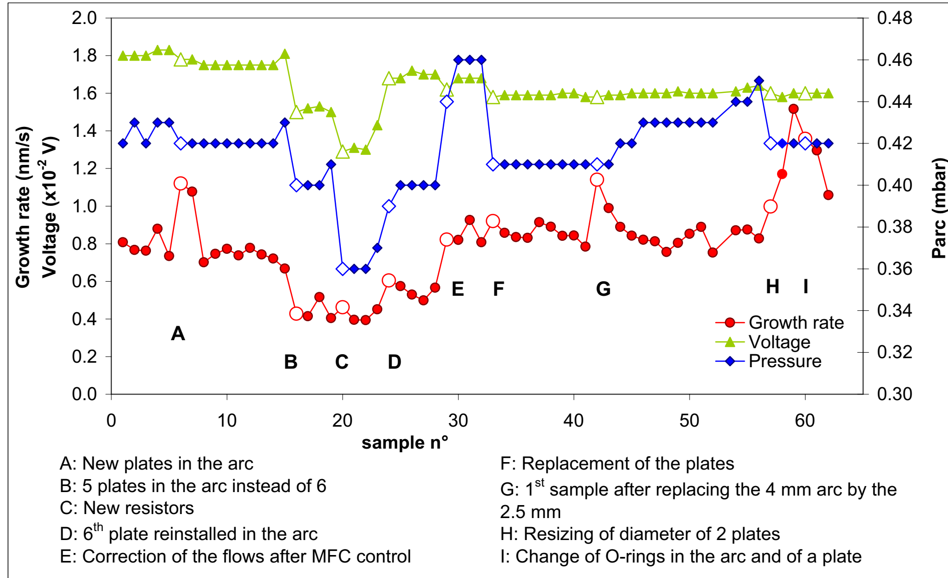

Figure 3.1: History of the reference layer deposition conditions: growth rate (●), voltage (▲) and pressure (◆) in the arc versus sample number. The letters indicate the changes in conditions and correspond to the open signs in the graph.

3.3 Results

3.3.1 Deposition history

We monitored the growth rate, the voltage and the pressure in the arc. Figure 3.1 shows the history of the deposited layers before the reproducibility study.

From figure 3.1, it is clear that several parameters influence the ETP set-up. First of all, we can see that the number of plates forming the arc determines the voltage across the arc. As the voltage increased, a plate was removed from the arc (case B). This had the effect that not only the voltage decreased (~180 V down to 150 V, suggesting 30 V per plate) but also that the growth rate decreased (0.8 nm/s down to 0.4 nm/s). We can see from figure 3.1 that putting back the 6th plate (case D), as well as correcting the gas flows for deviation of the mass flow controllers (case E), permitted us to obtain the standard conditions for our reference settings, namely a growth rate between 0.7 and 0.9 nm/s, a pressure in the arc between 0.41 and 0.43 bar and a voltage around 160 V. When the pressure in the arc increased again, because some extreme settings were tested, e.g. very high H_2 flows, the arc was dismantled and cleaned, or some parts were changed (cases F and H) and the pressure returned within the standard range.

Thus a large pressure increase in the arc is a sign of deterioration of the copper plates, indicating that the inner diameter might have been reduced due to sparking, erosion of the ceramic isolation of the cathode tips and local melting of the copper.

Secondly, when new plates are built in the arc, either because they are dirty or deteriorated (cases A, F and H), or because another arc is used in the meantime (case G), the reference pressure in and the reference voltage across the arc are obtained again. However, the growth rate increases and a dummy run has to be carried out before processing after the arc has been opened. We think indeed that oxygen or water could be trapped in the arc and a dummy run is necessary to 'clean' it out. The increase in growth rate can be due to the growth of less dense material, the particle flux reaching the substrate surface remaining the same.

Another important aspect concerning the arc stability is the inner diameter of the boron-nitride rings. The diameter of the boron-nitride discs that separate the copper plates should be slightly larger than the channel diameter to insulate perfectly one plate from the other. The discs used had an inner diameter of 4.5 mm and their replacement by discs of 3-mm inner diameter allowed achieving stable plasma.

The position of the three cathodes in the housing also influences the voltage in the arc. One should take care that the three tips are positioned symmetrically in the orifice to avoid overloading of one of the cathodes (not shown in figure 3.1). Moreover, these tungsten cathode tips can erode, although it is a quite slow process, and this influences the stability of the plasma. Finally, the copper plates should be scratch-free, as a tiny mark on the plate can lead to some air leak in the system, deteriorating the properties of the grown material.

Finally, it can be noticed that the implementation of extra resistors to sustain the power of the arc for the deposition of microcrystalline silicon (case C) decreased the voltage and the pressure in the arc. This changed our reference voltage from 180 V to 160 V.

In summary, the following aspects determine the arc performance: 1) the number of copper plates forming the arc determines the voltage across the arc when the plasma is on. We found that, when the voltage increased, removing a plate in order to reduce it was not a good solution as the growth rate will decrease. Moreover, the increase in voltage is due to a deterioration of the plates; 2) the narrowing of the inner diameter of the arc results in higher pressure. The inner diameter of the arc channel can be reduced by some melted copper, deposition of eroded ceramic material in the arc channel and in these conditions the plasma is less stable. This can happen when extreme conditions are used (high H_2 flows) and the arc starts to spark; 3) after the replacement of plates, a dummy deposition is required to clean the arc channel; 4) the arc resistors also determine the voltage over the plates.

Some parameters, which are not ETP-related, were found to have their importance for a good reproducibility of the a-Si:H layers. It is indeed essential to control all hardware, such as the gas mass flow controllers that can deviate from their set-point, the

purity of the gases (purifiers have been installed on the SiH_4 and H_2 lines, 6.0 instead of 4.5), the pressure sensors that need to be regularly calibrated and the cleanliness of the substrates.

3.3.2 Temperature control

Before deposition, the sample needs to be heated up to the deposition temperature. It was shown before that a 10 to 15 min heating time was sufficient to do so when a He back flow was used [3]. However, we will show that temperature control, before and during deposition, plays a large role in the reproducibility of the layers properties. It is also important to let the sample cool down for a while in the load-lock before exposing it to the air, otherwise it could undergo a temperature shock, which can result in a strained layer.

In order to control the temperature of the substrate before and during deposition, a study using FTIR spectroscopy was carried out. Three parameters were varied: the He back flow, Φ_{He}, the heating time, t_{heat}, and the substrate temperature, T_{sub}. Applying a He back flow permits to convect the heat from the hot yoke to the sample and so to maintain the sample at the desired temperature. t_{heat} is referring to the time between the loading of the sample on the substrate holder and the beginning of the deposition when the shutter is removed from above the sample. The deposition temperature is kept at 250°C. The films have a thickness of 600 nm.

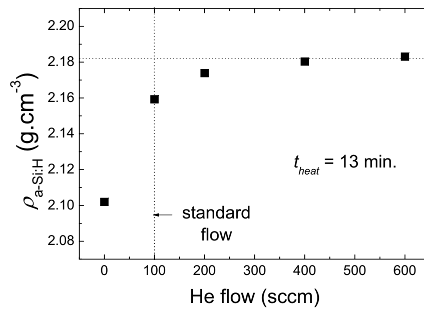

Figure 3.2: Mass density of a-Si:H thin films versus He flow, Φ_{He}.

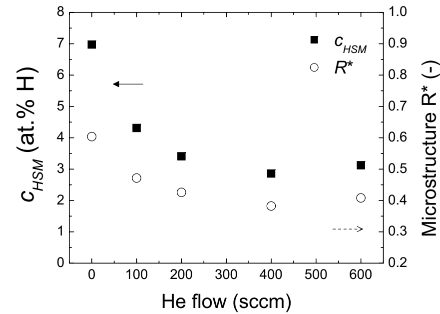

Figure 3.3: Hydrogen content calculated from the high stretching mode, c_{HSM}, and R* versus Φ_{He}.

In the first experiment, Φ_{He} is varied between 0 and 600 sccm and t_{heat} is taken at 13 minutes. For this condition, the growth rate remains constant, independent of Φ_{He}. However, as shown in figure 3.2, the density of the a-Si:H thin film increases with higher He flows to saturate around Φ_{He} = 400 sccm. The hydrogen content, as determined from FTIR, decreases as a function of He flow and reaches saturation for Φ_{He} ~ 400 sccm. Moreover, the hydrogen content from the high stretching mode,

c_{HSM}, as well as the microstructure parameter R^*, follows the same decreasing trend (figure 3.3). c_{HSM} corresponds to SiH_2 bonding [4] or clustered hydrogen and hydrogen bonded at the surface of nano-sized voids [5]. The decrease of c_{HSM} is attributed to a densification of the material due to a lower nano-void concentration in the film. The drop of R^* is also interesting as a lower R^* value generally indicates that the material is less sensitive to the Staebler-Wronski effect during degradation [6-8]. In summary, we conclude that the temperature of the a-Si:H growth surface is better controlled when a high He back flow is used.

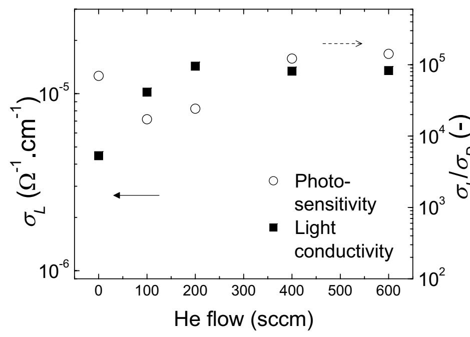

Figure 3.4: σ_L and photosensitivity of a-Si:H films versus He back flow, Φ_{He}.

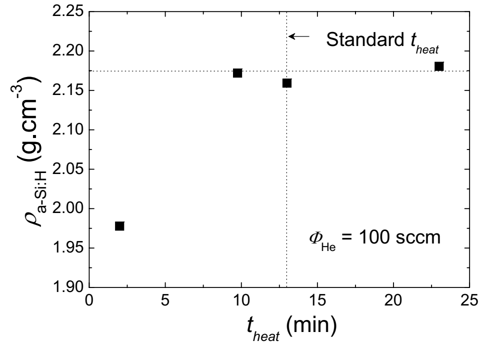

Figure 3.5: Mass density of a-Si:H films versus heating time t_{heat}.

For $\Phi_{He} \geq 400$ sccm, the low hydrogen content (~ 10 at.%) in the thin films indicates that the growing surface is sufficiently heated and that cross-linking and elimination of H_2 can take place. The optical band gap decreases from 1.80 eV at $\Phi_{He} = 0$ to 1.74 eV at 600 sccm. The light conductivity is also improved and as the dark conductivity decreases slightly, the photosensitivity of the thin films is enhanced for $\Phi_{He} \geq 400$ sccm (figure 3.4).

In a second experiment, the influence of t_{heat} is studied and Φ_{He} is kept constant at 100 sccm. The growth rate is not affected by t_{heat}. However, as shown in figure 3.5, a heating time of at least 10 min is necessary to obtain dense material. c_{HSM} also decreases when more time is allowed to heat up the substrate, but even after 23 min the low c_{HSM} obtained using Φ_{He}= 600 sccm is not reached (see figure 3.6).

The same trend is observed for the microstructure R^*. A lower R^* value, attributed to a lower nano-sized void density, is obtained when a large heating time is used, but still R^* is higher than for conditions with a high He flow (Fig. 3.6). This means that it is rather preferred to heat up the sample using a high Φ_{He} than to wait a long time for the substrate to reach the desired temperature with a low Φ_{He}. The light conductivity is, within the measurement accuracy, more or less independent of t_{heat}, with the best value at $1\times10^{-5}\ \Omega^{-1}.cm^{-1}$ for a 13 min heating time (figure 3.7).

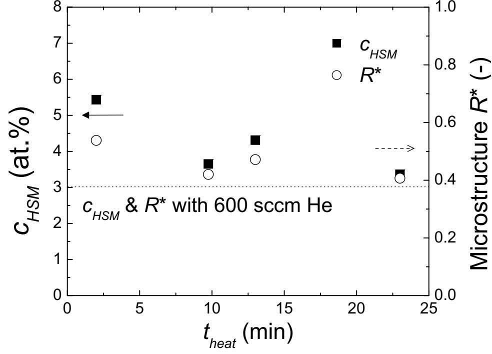

Figure 3.6: Hydrogen content from the high stretching mode and microstructure R^* versus t_{heat}. Φ_{He} = 100 sccm.

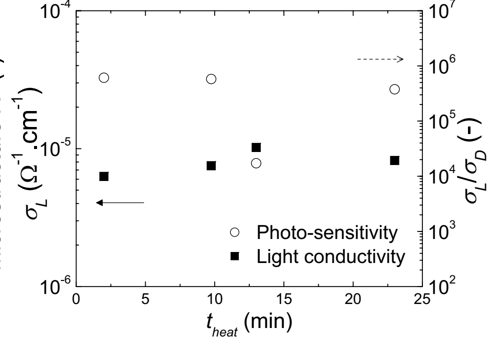

Figure 3.7: Light conductivity σ_L and photo-sensitivity of a-Si:H thin films versus t_{heat}.

In the third experiment, we varied the substrate temperature from 100°C to 400°C. Φ_{He} was set at 100 sccm and t_{heat} at 13 min. The density of the thin films increases with higher T_{sub} and the hydrogen content decreases below 10 at.% (Fig. 3.8 (a) & 3.8 (b)). Parallel to the decrease of c_{HSM}, the H content from the low stretching mode (c_{LSM}) increases. This suggests that more mono- or divacancies, with only Si-H bondings at their surface, are incorporated in the films instead of nano-sized voids. The R^* value drops below 0.2 at 400°C; this value could not be obtained either with a high Φ_{He} or a long t_{heat}. The a-Si:H network contains less defects, which is confirmed by the electronic properties of the material (figure 3.8 (c)), where the light conductivity goes from 1×10^{-7} to 2×10^{-5} Ω^{-1}.cm^{-1}.

In conclusion, the conditions used to prepare the sample before deposition so far (100 sccm He back flow for 10 min) were not sufficient to bring the substrate to a stabilized temperature. A He flow of 400 sccm has to be used for at least 13 min to ensure that the growing surface is at the good temperature and stays at this temperature during the whole deposition. Higher He flows are not necessary as the properties of the a-Si:H thin films do not change for flows above 400 sccm. It is also not necessary to prolong the heating time further than 13 min as very long t_{heat} would be needed to improve further the properties. To obtain denser material, a higher substrate temperature can be used.

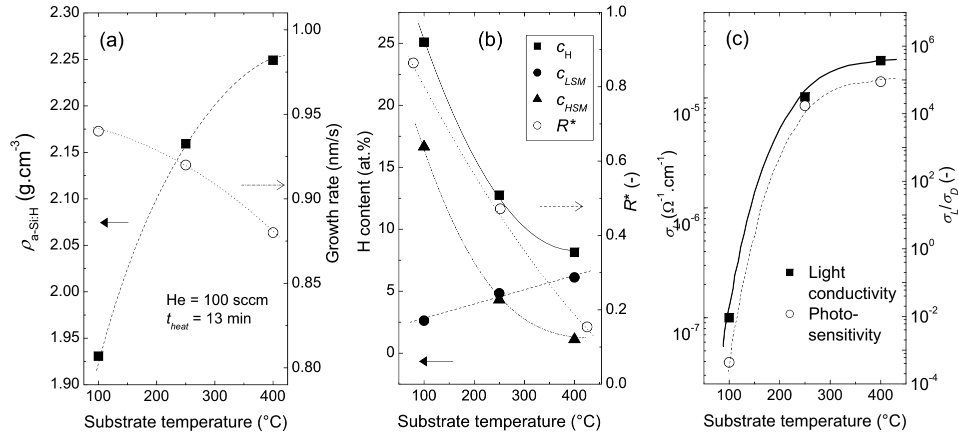

Figure 3.8: Mass density and growth rate (a), H content and microstructure R^* from FTIR (b) and light conductivity and photosensitivity (c) of ETP a-Si:H versus T_{sub}. Lines are guide to the eye.

3.3.3 Reproducibility study

In order to estimate the effect of the measures taken to improve the control of the a-Si:H deposition with ETP, a reproducibility study on single layers has been carried out. The conditions were as follows: Ar = 900 sccm, H_2 = 200 sccm, SiH_4 = 200 sccm and He back flow Φ_{He} = 400 sccm; $p_{reactor}$ = 0.24 mbar and T_{sub} = 400°C. The current through the arc was 40 A, the voltage 150 V and the pressure in the arc 0.52 bar.

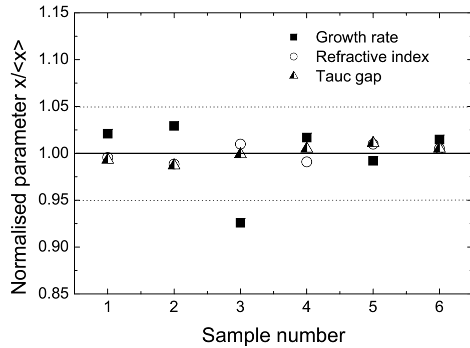

Figure 3.9: Normalized R_d, n_{2eV} and E_{Tauc} values determined from RT measurements.

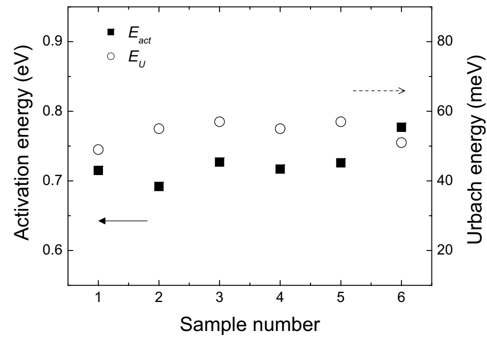

Figure 3.10: Activation energy and Urbach energy versus sample number.

The growth rate, R_d, the refractive index at 1.96 eV, n_{2eV}, and the Tauc optical band gap, E_{Tauc}, were determined. The normalised value to the average of these parameters can be found in figure 3.9. Their standard deviation is as follows: 3.8% for R_d, 1.0% for n_{2eV} and 0.9% for E_{Tauc}. These parameters reproduce within a standard deviation of 5%. The electric properties such as the activation energy of the dark conductivity, E_{act}, and the Urbach energy, E_U, are plotted in figure 3.10. Their standard deviation is slightly higher, with respectively 3.9% for E_{act} and 5.9% for E_U. The higher standard deviation obtained for the E_U originates from the inaccuracy of the DBP fitting.

The dark and light conductivities vary less than an order of magnitude (figure 3.11). Note that the dark conductivity depends exponentially on the Fermi level position and therefore a slight variation in the activation energy already implies a substantial change in σ_D. The light conductivity depends on the light generated carrier density in the material and their lifetime, thus on the defect density.

R_d (nm/s)	1.93 ± 0.07	$\rho_{a\text{-}Si:H}$ (g.cm^{-3})	2.25 ± 0.01
n_{2eV} (-)	4.23 ± 0.04	c_H (at.%)	5.9 ± 0.5
E_{Tauc} (eV)	1.67 ± 0.01	c_{LSM} (at.%)	4.6 ± 0.2
E_{act} (eV)	0.73 ± 0.03	R* (-)	0.05 ± 0.03
E_U (meV)	53.9 ± 3.2		

Table 3.1: Average of the main parameters of a-Si:H samples and their standard deviation.

From FTIR spectroscopy, c_H, c_{LSM} and $\rho_{a\text{-}Si:H}$ of the thin films have been determined (figure 3.12). $\rho_{a\text{-}Si:H}$ is reproduced very accurately with a standard deviation of 0.1%. c_H and c_{LSM} deviate somewhat more with a standard deviation of

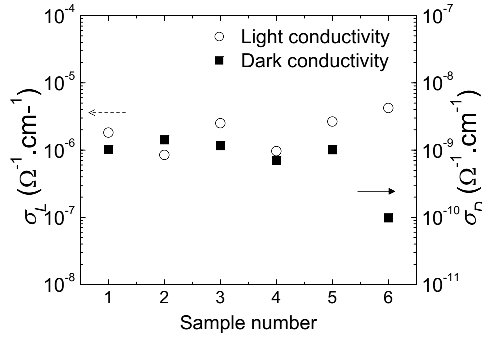

Figure 3.11: Light and dark conductivities versus sample number.

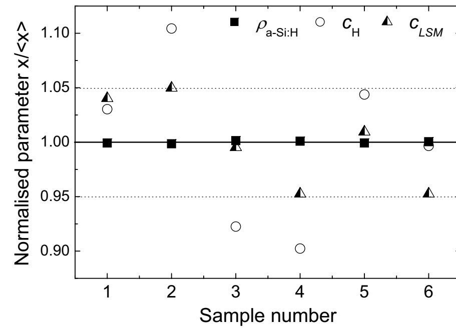

Figure 3.12: Normalised $\rho_{a\text{-}Si:H}$, c_H and c_{LSM} values determined from FTIR measurements.

respectively 7.7% and 4.2%. This higher standard deviation is due to the inaccuracy of the background subtraction while analyzing the FTIR data for samples with a low c_H

(6 at.%). The average values of the electric-optical properties of the a-Si:H are listed in table 3.1.

3.4 Conclusions

To ensure the reproducibility of layers grown with the ETP technique, the arc source of the plasma has to be checked and cleaned regularly. By monitoring the pressure in the arc, as well as the voltage across the arc, it is easily possible to get information about the status of the arc. An increase of these parameters is a sign of deterioration of the arc, which can be due to erosion of the tungsten cathode tips or to a diminution of the channel diameter if some sparks were observed from the arc.

Another important issue concerning the reproducibility of a-Si:H is the temperature control of the substrate and thus of the growing surface. Before deposition, a heating time of at least 13 min with a He back flow of 400 sccm should be allowed to bring the substrate at the desired temperature. During deposition, the same He flow should be used to maintain the temperature and avoid that the substrate heats up further because of the direct exposition to the plasma beam.

Finally, when these precautions are taken, the a-Si:H thin films deposited by ETP-CVD are reproducible. A variation of less than 5% is found for parameters such as growth rate and mass density, whereas the variation in the Urbach energy is lower than 6%. The electric properties of the material are more difficult to reproduce as they depend exponentially on the position of the Fermi level but they are also reproducible within one order of magnitude.

References

[1] J. Tauc, R. Grigorovici and A. Vancu, Phys. Stat. Sol. **15** (1966) 627

[2] J.C. van den Heuvel, M.J. Geerts and J.W. Metselaar, Sol. Energy Mater. **22** (1991) 185

[3] B.A. Korevaar, unpublished results

[4] G. Lucovsky, R.J. Nemanich and J.C. Knights, Phys. Rev. B **19** (1979) 2064

[5] A.H.M. Smets, W.M.M. Kessels and M.C.M. van de Sanden, Appl. Phys. Lett. **82** (2003) 1547

[6] B.G. Budaguan, A.A. Aivazov, M.N. Meytin and A.G. Radoselsky, Mater. Res. Soc. Proc. **485** (1998) 297

[7] U.K. Das and P. Chaudhuri, Indian J. Phys. Part A, **71**(3) (1997) 279

[8] J.A. Schmidt, R.R. Koropecki, R. Arce and R.H. Buitrago, J. Appl. Phys **78** (1995) 5959

A brief introduction to a-Si:H growth mechanism

Since the discovery in 1975 by Spear *et al.* of hydrogenated amorphous silicon (a-Si:H) [1], much effort has been spent on understanding the growth mechanism of this material. Gallagher [2], Perrin *et al.* [3] and Matsuda *et al.* [4] were the first to develop a model in which growth of a-Si:H from plasma enhanced chemical vapor deposition (PE-CVD) occurs by precursor-mediated chemisorption and recombination.

The deposition process of a-Si:H from a silane plasma consists of four stages: the creation of reactive species in the plasma, their transport to the film surface, their reaction with the growing-surface and finally the conversion of surface layers into bulk a-Si:H. In the following section we will shortly described these four stages.

1. Creation of reactive species in the plasma

In a silane plasma, in the absence of hydrogen atoms or ions flux and at low temperature, the top surface of a-Si:H film is essentially covered by hydrogen atoms. It is generally accepted that the main growth precursors of a-Si:H by rf PE-CVD are SiH_3 radicals [5-8], which are produced in the gas phase. Kessels *et al.* [9] showed that the contribution of SiH_3 to a-Si:H growth, calculated from cavity ring-down spectroscopy (CRDS) and threshold ionization mass spectrometry (TIMS) measurements, increases with increasing H_2 flow and saturates for flows larger than 8 sccs (see figure 1). Being a low reactive species, SiH_3 survives the collisions longest in

the plasma. It indeed does not react with SiH_4 because Si_2H_n structures are possible only with $n \leq 6$, and therefore SiH_3 radicals have the highest concentration. Hoefnagels *et al.* have demonstrated by time-resolved CRDS that SiH_3 was unreactive in gas phase [10].

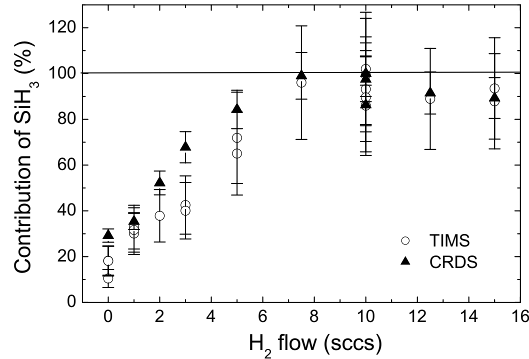

Figure 1: Contribution of SiH_3 to a-Si:H film growth, from CRDS and TIMS measurements [9].

2. Transport of reactive species to the film surface

It has been observed experimentally that a-Si:H has a smooth surface. For that, surface diffusion of radicals and hydrogen abstraction from kink or valley-sites are required. The SiH_3 radical has only one dangling bond and therefore cannot be added to fully hydrogenated sites of a-Si:H film surface. Instead, it may physisorb on the film surface, creating a dipole interaction with the surface, and then hop from site to site on the passivated surface [3]. Dewarrat and Robertson [11] proposed another mechanism: SiH_3 radicals are in a physisorbed state and for that, hydrogen from the passivated surface adjusts its configuration and moves to an antibonding site. Then SiH_3 radical can diffuse from one surface Si to the next, in agreement with minimization of surface energy. The hydrogen at the antibonding site comes back to a normal Si-H bond, while the next hydrogen is pushed into an antibonding site. Gupta *et al.* proposed that SiH_3 radicals diffuse through Si-Si bond breaking and reforming [12]. Hydrogen insertion into a weak stretched Si-Si bond facilitates the bond breaking and the Si-Si bond formation is accompanied by the formation and release of a H_2 molecule.

3. Reaction of reactive species with the growing-surface

The sticking of SiH_3 radicals on the a-Si:H surface requires first the creation of dangling bonds. When hydrogen and silyl radicals impinge on the a-Si:H surface, the atomic H are much more likely to abstract surface hydrogen, hence create dangling bond sites, compared to the SiH_3 radicals [12]. Growth sites are thus dominantly

created by hydrogen recombination (1). Hydrogen adsorption (2) and hydrogen recombination (1) are competing reactions. However, recent research [13,14] has shown that the main process for H-abstraction from the surface is by SiH_3 radicals through an Eley-Rideal reaction mechanism (3). SiH_4 molecules then return to the gas phase. At high temperature, associative desorption or thermal desorption of H_2 from neighboring -SiH occurs, leaving two dangling bonds (4). In a diluted silane plasma, hydrogen-induced etching of silicon can occur (5). Finally, dangling bonds can be created by ion-induced reactions combined with H_2 abstraction (6). No sputtering is considered, as high ion energies are required.

$$(SiH)_s + H \rightarrow (Si\text{—}DB)_s + H_2$$ Hydrogen recombination (1)

$$(Si\text{—}DB)_s + H \rightarrow (SiH)_s$$ Hydrogen adsorption (2)

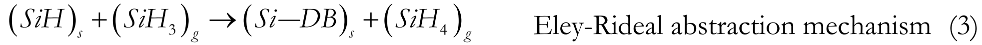
$$(SiH)_s + (SiH_3)_g \rightarrow (Si\text{—}DB)_s + (SiH_4)_g$$ Eley-Rideal abstraction mechanism (3)

$$(SiH)_s + (SiH)_s \rightarrow 2(Si\text{—}DB)_s + (H_2)_g$$ Associative desorption (4)

$$(SiH_3)_s + H \rightarrow (Si\text{—}DB)_s + (SiH_4)_g$$ Etching (5)

$$(SiH)_s + A^+ \rightarrow (Si\text{—}DB)_s + H_2 + B^+$$ Ion induced reaction (6)

with -DB standing for dangling bond, subscript *s* for solid and *g* for gas phase.

a-Si:H growth mainly takes place from SiH_3 radicals finding a dangling bond and chemisorbs. However, polysilane radicals and silicon cluster ions participate to the film growth, although to a smaller extend (< 10%). It is mentioned in literature that these large species lead to a higher density of Si-H_2 bonding configuration, which means that the microstructure of the material is increased [15].

4. Conversion of surface layers into bulk a-Si:H

The final step of a-Si:H growth consists of hydrogen elimination as the H-rich surface layer (50-60 at. H %) is converted into bulk Si-Si network containing typically 4 to 20% hydrogen atoms. At low temperature growth, Robertson [16] proposed an explanation based on thermodynamics: the neighboring SiH undergo a spinodal decomposition in which species diffuse up a concentration gradient, so the excess hydrogen from the bulk is expelled towards the hydrogen-rich surface. During that process, an intense bond rearrangement accompanies hydrogen elimination and leads to disorder and creation of weak Si-Si bonds. At deposition temperature above 400°C, it is reported that thermal associative desorption of hydrogen occurs spontaneously from bond reconstruction between neighboring chemisorbed SiH_3. At low deposition temperature, weak bonds facilitate hydrogen elimination, allowing local rearrangement of hydrogen in pair, hydrogen passing through a bond center to join another hydrogen, to form molecular H_2 [16].

In the next two chapters, we will focus on the electro-optical properties of a-Si:H deposited by ETP-CVD at high growth rates. In particular, we will investigate the material properties as function of plasma settings, such as additional hydrogen injection in the reactor through the nozzle (in Chapter 4) and external rf bias on the substrate (in Chapter 5). These two approaches have in common that they aim to reduce the influence of large silicon-related species, like cluster ions and polysilanes, that are present in the plasma and participate to the a-Si:H growth, as these large species are believed to lower the material properties.

References

[1] W.E. Spear and P.G. le Comber, Sol. State Com. **17** (1975) 1193
[2] A. Gallagher, Mater. Res. Soc. Symp. Proc. **70** (1986) 3
[3] J. Perrin, Y. Takeda, N. Hirano, Y. Takeuchi and A. Matsuda, Surf. Sci. **210** (1989) 114
[4] A. Matsuda, K. Nomoto, Y. Takeuchi, A. Suzuki, A. Yuuki and J. Perrin, Surf. Sci. **227** (1990) 50
[5] A. Gallagher, J. Appl. Phys. **63** (1988) 2406
[6] J. Perrin, M. Shiratani, P. Kae-Nune, H. Videlot, J. Jolly and J. Guillon, J. Vac. Sci. Technol. A **16**(1) (1998) 278
[7] A.J. Flewitt, J. Robertson and W.I. Milne, J. Appl. Phys. **85** (1999) 8032
[8] A. Matsuda, M. Takai, T. Nishimoto and M. Kondo, Sol. Energy Mat. & Sol. Cells **78** (2003) 3
[9] W.M.M. Kessels, M.G.H. Boogaarts, J.P.M. Hoefnagels, D.C. Schram and M.C.M. van de Sanden, J. Vac. Sci. Technol. A **19** (2001) 1027
[10] J.P.M. Hoefnagels, A.A.E. Stevens, M.G.H. Boogaarts, W.M.M. Kessels, M.C.M. van de Sanden, Chem. Phys. Lett. **360** (2002) 189
[11] R. Dewarrat, J. Robertson, Appl. Phys. Lett., **82** (2003) 883
[12] A. Gupta, H. Yang, G.N. Parsons, Surf. Sci. **496** (2002) 307
[13] W.M.M. Kessels, J.P.M. Hoefnagels, P.J. van den Oever, Y. Barrell, M.C.M. van de Sanden, Surf. Sci. **547** (2003) L865
[14] S. Ramalingam, D. Maroudas, E.S. Aydil, S.P. Walch, surf. Sci. **418** (1998) L8
[15] H.A. Weakliem, R.D. Estes and P.A. Longeway, J. Vac. Sci. Technol. A **5** (1987) 29
[16] J. Robertson, J. Non-Cryst. Sol. **266** (2000) 79

Chapter 4

Hydrogen injection in ETP plasma jet for fast-deposition of high-quality a-Si:H

4.1 Introduction

The deposition of hydrogenated amorphous silicon (a-Si:H) by plasma enhanced chemical vapor deposition (CVD) is inseparable from the plasma chemistry and the formation of silicon radicals from the precursor silane (SiH_4) in the gas phase. With the expanding thermal plasma (ETP) CVD technique, the dissociation of SiH_4 initially occurs from collision with argon ions (equation 1), which produces silicon-ions.

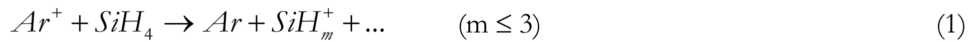

$$Ar^{+} + SiH_4 \rightarrow Ar + SiH_m^{+} + ... \qquad (m \leq 3) \qquad (1)$$

Subsequently, depending on the electron density, these silicon-ions are immediately further dissociated by either interaction with an electron (equations 2 followed by 3) or either by collision with another silane molecule (equations 4 and 5). Both of these routes lead to the formation of large silicon-containing radicals or ions.

At high electron density ($n_e > 10^{17}$ m^{-3}):

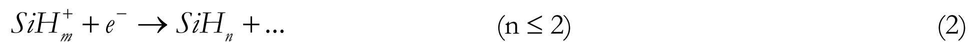

$$SiH_m^{+} + e^{-} \rightarrow SiH_n + ... \qquad (n \leq 2) \qquad (2)$$

$$SiH_n + SiH_4 \rightarrow Si_2H_p + ... \qquad \text{polysilane radical formation} \qquad (3)$$

And at lower electron density ($n_e = 10^{17}$ m^{-3}):

$$SiH_m^+ + SiH_4 \rightarrow Si_2H_r^+ + ... \quad (4)$$

$$Si_pH_r^+ + SiH_4 \rightarrow Si_{p+1}H_q^+ + ... \quad \text{silicon cluster ions formation} \quad (5)$$

However, these reactions are dominant only at zero or very low hydrogen flow. Kessels *et al.* [1] have shown that the ion density decreases significantly when the H_2 flow is increased due to charge transfer reactions (equation 6), immediately followed by dissociative recombination reactions (equation 7).

$$Ar^+ + H_2 \rightarrow ArH^+ + H \quad (6)$$

$$ArH^+ + e^- \rightarrow Ar + H \quad (7)$$

Injection of hydrogen in the arc effectively reduces the ion density emanating from the arc and a small channel diameter, like on the CASCADE set-up of Delft, results in a more effective quenching of the ion and electron densities [2]. To reduce the ion density further, we propose to inject also hydrogen directly into the reactor, through the nozzle. In presence of H_2 in the plasma, and consequently of atomic hydrogen, according to equations (6) and (7), the dominant dissociation of silane is H-induced and governed by equation (8).

$$SiH_4 + H \rightarrow SiH_3 + H_2 \quad (8)$$

Nevertheless, ions cannot be completely eliminated and the ion density does not diminish further than a factor 3 for larger H_2/Ar ratio than 5% [2]. Silicon-ion clusters can still be generated from charge transfer reaction (9) between H^+ and silane, followed by ion-molecule reaction (10).

$$SiH_4 + H^+ \rightarrow SiH_3^+ + H_2 \quad (9)$$

$$SiH_3^+ + SiH_4 \rightarrow Si_2H_q^+ + pH \quad (10)$$

A complete overview of the possible reactions occurring in the arc plasma and in the reaction chamber has been presented by van de Sanden *et al.* [3] and by Kessels *et al.* [4].

The plasma chemistry is of concern because of its impact on the material growth and properties. As a matter of fact, the properties of a-Si:H deposited by ETP-CVD are strongly influenced by the ions emanating from the arc, because polysilane radicals, $(SiH_2)_n$ $n \geq 2$, and silicon-cluster ions, $Si_pH_q^+$, are created when ion-induced dissociation of SiH_4 takes place (equations 3 and 5). These reactions are not desirable because polysilane radicals and silicon-cluster ions lead to material with higher microstructure [5], even if their contribution to the growth is limited (< 10%). The preferred dissociation route of SiH_4 is through collision with an atomic H (eq. 8) as SiH_3 has been identified as the precursor inducing improvement of a-Si:H properties when its contribution to the film growth is increased [6]. The favorable influence of SiH_3 radicals is attributed to its low surface reaction probability compared to other

silane radicals, implying a higher ability to diffuse over the growing surface. The probability to reach a step or valley is then increased and consequently the chance to incorporate voids or to get a columnar film growth is reduced. A smooth and dense material is consequently obtained.

In this chapter, we present the results of an investigation on the a-Si:H material properties when additional hydrogen is injected directly into the plasma jet at the exit of the arc. The addition of H_2 in the nozzle is expected to reduce the ion density further and the achievement of higher growth rates while keeping the pressure, voltage and gas mixture in the arc constant, leaving the plasma chemistry in the arc unchanged. After a comparison of materials deposited with and without hydrogen injected in the nozzle, H_{2Noz}, we will show the influence of several process parameters on material quality, such as deposition pressure, substrate temperature and gas mixture. Finally, we will present a comparative study with a-Si:H prepared in another ETP set-up and we will discuss the role of hydrogen bonding in the structural properties of a-Si:H. We will show that the vacancy- to void-dominated density transition is determined by the amount of polysilane radicals or clusters in the reactor versus the silicon growth flux.

4.2 Experiment

The channel diameter of the cascaded arc used in the Delft University set-up has been decreased compared to that of the Depo II set-up at the department of Applied Physics of the Eindhoven University of Technology (from 4 mm down to 2.5 mm). This was done in order to find a compromise between a smaller pump capacity of CASCADE compared to Depo II - leading to a smaller total possible gas flow during process - and the need of an arc pressure greater than 0.3 bar to create a stable thermal plasma in the cascaded arc. To ensure high growth rates, high argon, silane and hydrogen flows should be used. The addition of hydrogen in the arc can become a problem as the voltage over the cascade plates increases and there is a risk of voltage breakdown if the electric field between two copper plates is greater than 40 kV/m [2]. To avoid this problem and still be able to reach high growth rates, hydrogen has been injected directly in the plasma jet at the exit of the arc. The addition of H_2 in the nozzle permits to reach higher growth rates while keeping the pressure and voltage in the arc constant.

The a-Si:H depositions were carried out in the multi-chamber deposition system CASCADE. A description of the ETP set-up can be found in the experimental chapter of this thesis and more details are published elsewhere [7]. Layers of a-Si:H were deposited on Corning glass 1737 for optical and electric characterizations (reflection-transmission, dark and light conductivity, Urbach energy and defect density) and on crystalline silicon wafers for Fourier transform infrared (FTIR) absorption spectroscopy (hydrogen content, bonding configuration, microstructure).

Comparison with and without H_{2Noz}: two series were carried out, one with H_2 only in the arc (series I), the other one with 200 sccm extra H_2 injected in the nozzle (series II). The substrate temperature was varied from 200 to 400°C. The purpose was to assess the impact on growth conditions of H_2 admixture into the nozzle. The deposition conditions can be found in table 4.1.

Pressure series: (series III) the same gas settings were used as for series II. The reactor pressure was increased by partially closing the exhaust valve. The pressure was set at, respectively, 0.24, 0.26 and 0.28 mbar. The a-Si:H films were deposited with a substrate temperature of 400°C.

Temperature series: (series IV) three series were deposited with different silane flows. The substrate temperature was varied from 200 to 400°C. The flow ratio of H_2 in the arc and SiH_4 was kept constant as follows: 200/200 sccm, 270/260 sccm and 310/320 sccm. We will refer to these three series by the average growth rate of each series, 32 Å/s, 46 Å/s and 60 Å/s respectively.

H_2 flow series: (series V) the H_2 flow injected in the nozzle is varied from 0 to 250 sccm. The reactor pressure varies from 0.20 mbar for H_{2Noz} = 0 sccm to 0.24 mbar for H_{2Noz} = 250 sccm. The substrate temperature was chosen at 400°C, unless indicated otherwise.

(series VI) the total H_2 flow and the Ar flow are kept constant. (Ar = 850 sccm and total H_2 flows = 400 sccm). The ratio of H_2 in the nozzle to total H_2 in the reactor, $\Phi_{H2\ Noz}$ / $\Phi_{Tot\ H2}$, is varied from 0 to 1. The films are deposited at 400°C. The voltage in the arc varies from 183 V for $\Phi_{H2\ Noz}$ / $\Phi_{Tot\ H2}$ = 0 down to 81 V for $\Phi_{H2\ Noz}$ / $\Phi_{Tot\ H2}$ = 1.

Series	Ar (sccm)	$H_{2\ Nozzle}$ (sccm)	$H_{2\ Arc}$ (sccm)	SiH_4 (sccm)	Voltage (V)	Arc pressure (bar)	Temperature (°C)	Reactor pressure (mbar)
I	850	0	200	200	149	0.54	varied	0.21
II	850	200	200	200	147	0.55	varied	0.23
III	850	200	200	200	148	0.56	400	varied
IV	850	200	200	200	147	0.55	varied	0.23
	850	200	270	260	159	0.55	varied	0.24
	850	200	310	320	166	0.56	varied	0.25
V	850	varied	200	200	131	0.56	400	varied
VI	850	varied	varied	200	varied	0.55	400	0.23

Table 4.1: Overview of the deposition conditions used in this chapter to study the influence of H_2 injection in the nozzle on the a-Si:H film properties.

In addition, 400 sccm He was used as back flow for all the deposition conditions mentioned above in order to control the substrate temperature accurately. The arc current was set at 40 A and the pressure in the arc was p_{arc} = 0.55-0.56 bar. Except for

the pressure series (series III), the reactor pressure, p_{react}, was determined by the gas flows and the pumping capacity of the ETP set-up.

4.3 Results and discussion

4.3.1 Comparison between a-Si:H deposited with and without H_2 in the nozzle

The ETP technique is based on a remote plasma that is generated in the arc. This means that the arc is physically separated from the sample surface and that there is a large pressure difference between the arc and the reactor chamber. The physics and chemistry of the plasma depend on the pressure in the arc and on the voltage applied, as well as on the gas mixture injected in the arc. In order to alter the plasma chemistry in the reaction chamber and change the growth conditions without influencing the plasma processes in the arc, gas needs to be injected directly into the reactor. When H_2 is introduced through the nozzle (to which we will refer to from now on with H_{2Noz}), more SiH_4 can be dissociated whilst a stable plasma is obtained in the arc. By introducing H_{2Noz}, the growth rate is increased by 0.45 nm/s on average (see figure 4.1) without changing the SiH_4 flow, which was kept constant at 200 sccm. This increase in growth rate was not expected as the rate coefficient of silane dissociation by atomic H is much lower than by ionic H^+ ($k_H = 2 \times 10^{-16}$ m^3/s at 2000 K [8] and $k_{H+} = 5 \times 10^{-15}$ m^3/s [9]). However, SiH_4 dissociation by atomic H is temperature dependent and at high temperatures, hot atomic H has a higher reaction probability with SiH_4, which could explain the results.

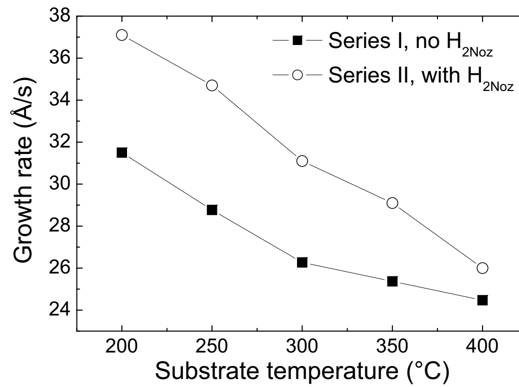

Figure 4.1: Growth rate versus substrate temperature for series I and II.

For each temperature, we observe that the Tauc band-gap of the sample with H_{2Noz} is slightly lower than that of the sample without H_{2Noz} (not shown here). This

correlates with a lower total H content ($E_{Tauc} = E_0 + B \times c_H$) [10,11]. However, the refractive index at 2 eV remains unchanged. The refractive index depends only on the substrate temperature and not on the total H_2 flow.

The increase in growth rate when injecting H_2 in the nozzle can be explained by even more quenching of the Ar^+ ion density by H_2 according to equations (6) and (7), generating more atomic hydrogen. The Ar^+ ions that come out of the arc have to go through a hydrogen 'curtain', which increases their probability to undergo charge-transfer reactions before interaction with SiH_4. The atomic hydrogen then reacts with SiH_4, leading to H abstraction reaction instead of charge transfer reaction [1] and forming SiH_3 radicals, as depicted in equation (10). It has been mentioned that the lowered Ar^+ density and the increased SiH_3 radical density are favorable for growing device-quality a-Si:H material and for reducing the formation probability of ions or large silicon clusters. Less clusters and polysilane radicals in the plasma lead to fewer defects in the material as the incorporation of these species is thought to result in void formation [12,13]. Moreover, as a result of the H_2 injection in the nozzle more atomic H is available in the reactor to dissociate SiH_4. Typically, the SiH_4 depletion is only 5 to 7% for a-Si:H growth conditions. We expect that this value is enhanced by the addition of H_2 in the nozzle, leading to a higher SiH_3 particle flux that contributes to the growth of a-Si:H. Hydrogen induced dissociation of SiH_4 is the advocated reaction to obtain better material quality.

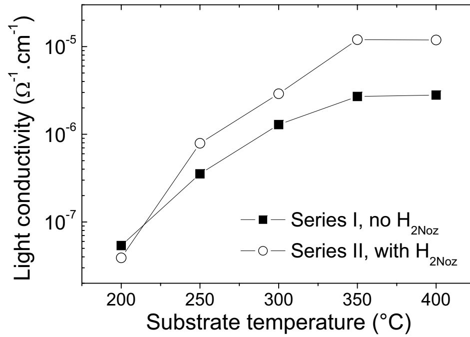

Figure 4.2: Light conductivity vresus temperature for series I and II.

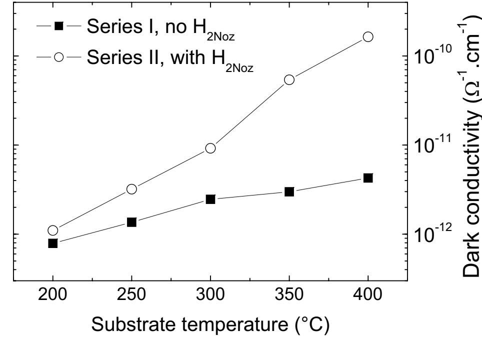

Figure 4.3: Dark conductivity versus temperature for series I and II.

Figure 4.2 shows the light conductivity as a function of the substrate temperature for the two series. It is clear that the injection of extra H_2 directly into the reactor enhances the light conductivity. As show in figure 4.3, the dark conductivity, σ_D, is also increased, which results in a lower photoresponse. However, the increase in σ_D is more pronounced in series II than in series I and this cannot be explained by the decrease in band gap only. We think that the carrier mobility increases with H_{2Noz}. This increase in dark conductivity is not linked to an increase of defect states in the band-gap, as we

observe that the defect density, obtained from DBP measurements, follows the same trend for the two series (see figure 4.4). The Urbach energy is actually reduced with H_{2Noz}, and so is the defect density, to a minor extent.

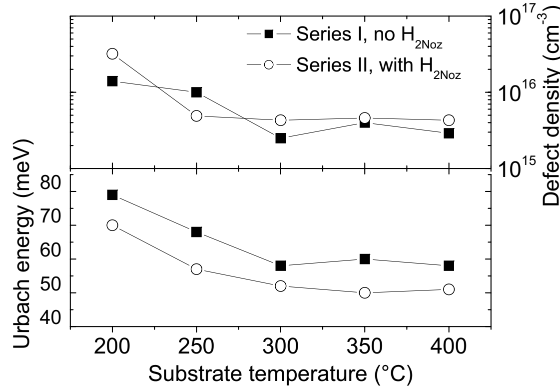

Figure 4.4: Defect density and Urbach energy versus substrate temperature for series without and with H_{2Noz} (series I and II).

From the comparison between series I and II, deposited without and with H_{2Noz}, we can conclude that the main advantage of H_2 in the nozzle is an increase in growth rate, while maintaining or even improving the material optical and electric properties. We note, however, that the pressure in the reactor increases slightly when H_2 is injected in the nozzle, reducing the plasma-beam diameter.

4.3.2 Pressure series

We investigated the influence of the reactor pressure on the material properties by carrying out a reactor pressure series. This was achieved by partially closing the exhaust valve, increasing the pressure for a given gas-flow setting to obtain a constant reactor pressure. The a-Si:H films were deposited at 400°C, the temperature at which we have grown the best film in terms of material properties.

During ETP-CVD, the growth rate does not depend only on precursor gas flow, but also on the reactor pressure. The increase in growth rate may arise from the reduction of the plasma beam diameter when higher reactor pressures are used. When the gas flux remains the same, more radicals arrive on a smaller surface area, which leads to a higher growth rate. However, the pressure increase in the reactor entails an increase of the growth rate of 2.3 Å/s on average per 0.02 mbar (0.02 mbar is the pressure increase observed when adding H_2 in the nozzle, see table 4.1). This was calculated from series III as well as from other deposition series where the pressure was varied. The reduction of the plasma beam explains only partially the increase in growth rate of 4.5 Å/s observed when H_2 is added in the nozzle. The remaining

growth-rate increase of 2.2 Å/s (on average) can be attributed to the effect of H_{2Noz} on either dissociation of SiH_4 or on further quenching of the remaining Ar^+ ion density coming from the arc.

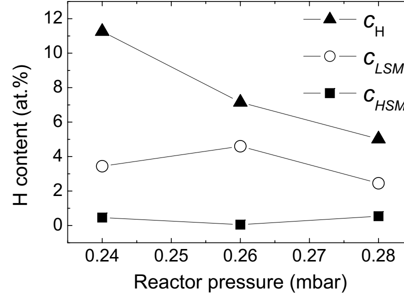

Figure 4.5: Total H content (c_H), low stretching mode (c_{LSM}) and high stretching mode (c_{HSM}) hydrogen content versus reactor pressure for series III.

The increase in growth rate due to higher pressures in the reaction chamber does not influence the optical properties of the material. However, the total hydrogen content, c_H, decreases at higher pressures, although c_{HSM} and c_{LSM} are more or less constant (see figure 4.5). Moreover, the electric properties are not influenced by a change in the reactor pressure. The Urbach energy, as well as the defect density in the band gap, does not show any trend with increasing reactor pressure.

In conclusion, we observe an increase of growth rate following an increase of the reactor pressure. This increase can be due to a reduction of the plasma-beam diameter and a concentration of the reactive species on a smaller surface area. Virtually no effect is observed on the optical and electric properties of the material. The reactor pressure seems to influence the structural properties of the material to a larger extent, as the hydrogen content decreases with an increase of pressure.

4.3.3 Temperature series

We deposited three temperature series varying the SiH_4 flow as described in section 4.2 (see table 4.1, series IV).

The deposition rate versus the substrate temperature is plotted in figure 4.6 for the three different gas settings used. The growth rate decreases as a function of increasing substrate temperature. This decrease of growth rate is due to a densification of the film (see figure 4.7). The mass density was obtained using the Clausius-Mossotti equation [14], with the refractive index, n_∞, and the hydrogen content, c_H, determined from FTIR measurements. The temperature at which the density saturates depends on the growth rate. It was shown by Mahan *et al.* [15] for hot-wire a-Si:H, as well as Kessels *et*

al. [16] and Smets *et al.* [17] for ETP a-Si:H, that for higher growth rates, higher substrates temperatures were necessary to densify the film.

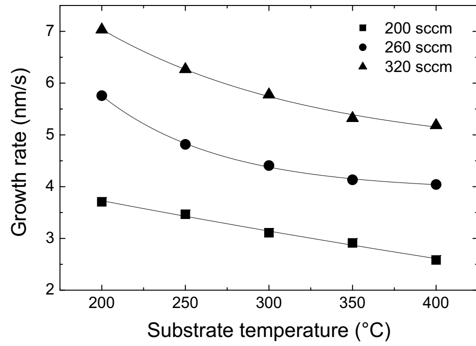

Figure 4.6: a-Si:H growth rate versus substrate temperature for three SiH_4 flows.

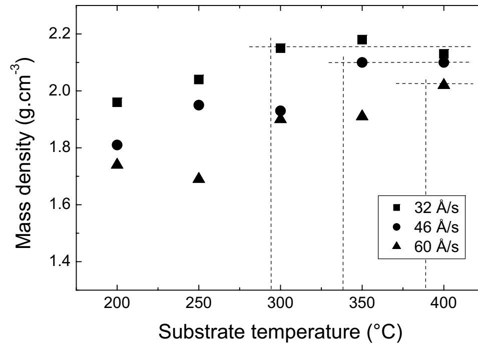

Figure 4.7: Film density from FTIR data versus substrate temperature for three series.

A possible reason for this densification is the thermally activation of Si radical diffusion, which gives rise at high temperatures to the diffusion of chemisorbed species to growth sites situated at steps or valleys. Another possibility for film densification is the faster desorption of intermediate species during growth, leading to a more ordered structure. As a result, the surface is smoother and the material denser and therefore the growth rate is reduced.

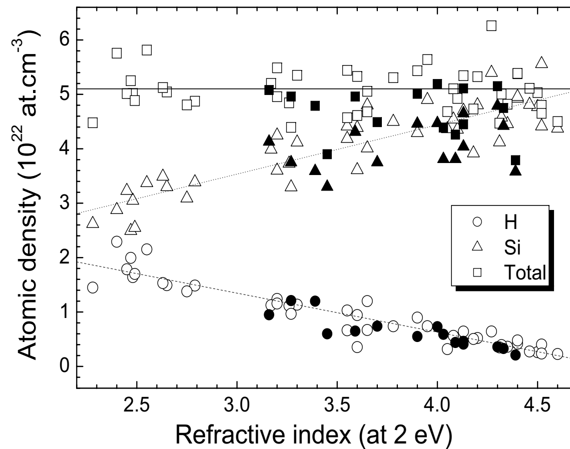

Figure 4.8: Atomic density of H, Si and sum of both from RBS measurements versus refractive index. Open symbols for Eindhoven samples, full symbols for Delft samples. Lines are guide to the eye.

The atomic densities of silicon and of hydrogen, as well as the total atomic density, were determined by Rutherford Backscattering Spectroscopy (RBS) and Elastic Recoil Detection Analysis (ERDA). In figure 4.8, we compare the hydrogen densities for ETP a-Si:H material obtained by Kessels *et al.* deposited with Depo II and ours deposited with CASCADE. We observe that the atomic hydrogen density as a function of the refractive index, n_{2eV}, for material deposited in CASCADE is in reasonable agreement with the data from Kessels *et al.* [18] for material deposited in Depo II. An increase in n_{2eV} leads to a decrease in hydrogen content and an increase in silicon density. This results in a total atomic density for the thin films of 5×10^{22} at.cm^{-3}, which is independent from n_{2eV}. Some samples have a significantly lower total density, which could come from a high void density.

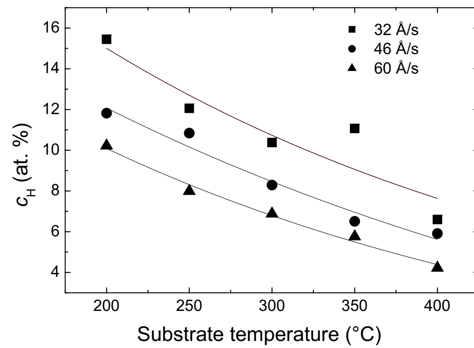

Figure 4.9: H content versus substrate temperature. Lines are guide to the eyes.

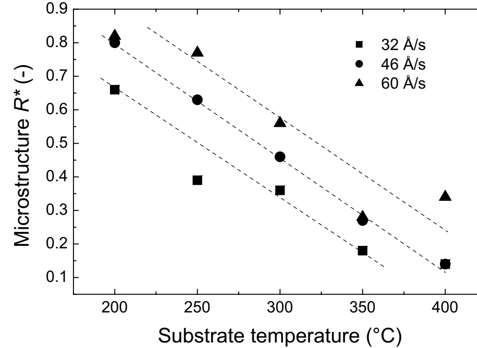

Figure 4.10: Microstructure parameter R^* versus substrate temperature. Lines are guide to the eyes.

The hydrogen content, c_H, and the microstructure parameter, R^*, are shown in figures 4.9 and 4.10, respectively. Obviously, both c_H and R^* drop as a function of temperature. At higher temperatures hydrogen is eliminated via a cross-linking mechanism [19, 20], creating a denser material that contains less hydrogen. The decrease in c_H is accompanied by a drop of the band gap (not shown here). It is interesting to note that the series grown at a faster deposition rate has a lower c_H (see figure 4.9). This is most likely a pressure effect, as seen earlier in this chapter. An increase in reactor pressure entails a reduction in hydrogen content in the deposited film. Although c_H is lower for the material grown at 60 Å/s, the R^* value indicates that a substantial fraction of the hydrogen is bonded in Si-H_2 configurations or in Si-H configurations on void surfaces. A high R^* value is generally accompanied by a larger void fraction in the material. This conclusion is in agreement with the data in figure 4.7, which show that material deposited at a high rate has a considerably lower mass density. We ascribe this lower mass density to a substantially higher void fraction.

Furthermore, from SAXS (Small Angle X-ray Scattering) and infrared measurements, Mahan *et al.* [21] deduced that the c_{HSM} is linked to microvoids and that the interior surfaces of these microvoids are largely unhydrogenated. This would explain why a higher void fraction leads to lower c_{H} for material deposited at high rates.

The Urbach energy (see figure 4.11) and the defect density decrease when the substrate temperature is increased, which again indicates that the film quality is improved at higher substrate temperature. A denser material, with a low microstructure, implies less defects and both the Urbach energy, as well as the absorption in the sub band gap, is lowered for substrate temperatures up to 300°C. No further decrease is observed for higher temperatures (Fig. 4.11).

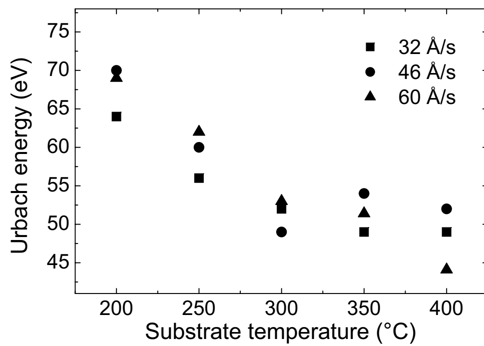

Figure 4.11: Urbach energy versus substrate temperature for three growth rate series.

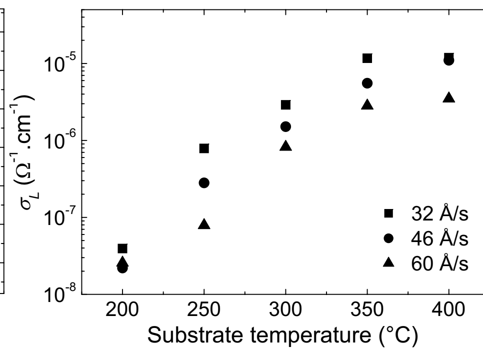

Figure 4.12: Light conductivity versus temperature for three growth rate series.

Figure 4.12 shows the increase in light conductivity as a function of substrate temperature. This increase can be explained by a reduction of the band gap and defect density. The light conductivity is higher for lower growth rates. As the band gap does not depend on the gas flows or the growth rate used but only on the substrate temperature, this growth-rate dependence of the light conductivity at a given temperature appears to be correlated to the R^* value. As noted above, this value gives an indication of the void fraction in the material. Indeed, we find a good correlation between light conductivity and R^*, as shown in figure 4.13. We think that, for material with a high R^* value, the defects on void surfaces act as recombination centers and lead to lower light conductivities. Obviously, a high R^* value leads to a lower light conductivity, which is generally ascribed to a higher defect density. Shiratani *et al.* found a correlation between Si clusters in the plasma and R^* [22]. The suppression of clusters by means of a filter grid situated above the sample led to cluster-free a-Si:H and the H concentration associated with SiH_2 bonds could be significantly reduced compared to the concentration found in conventional films.

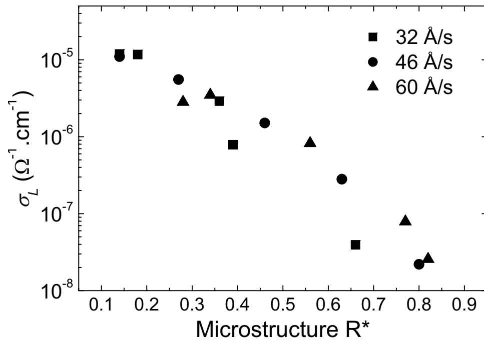

Figure 4.13: Light conductivity versus R^* microstructure for three growth rate series.

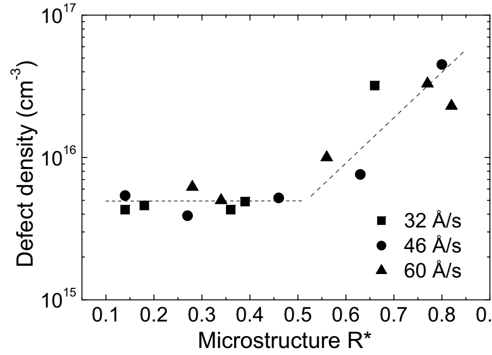

Figure 4.14: Defect density versus microstructure parameter R^* for three growth rate series.

In figure 4.14, the defect density, N_d, is plotted as a function of R^*. N_d is correlated to R^* and two regions can be distinguished. In the first region, $R^* < 0.5$, N_d is independent of R^* and has an average value of 5×10^{15} cm^{-3}. For these samples, a substrate temperature of at least 300°C was used. It is remarkable that N_d is not influenced by the R^* value (for $R^* <0.5$), whereas the light conductivity drops an order of magnitude in that region. However, we should note that DBP measurements tend to underestimate N_d [23]. In the second region, $R^* > 0.5$, N_d increases substantially. In that case, the substrate temperature was below 300°C. For $R^* > 0.5$, the void fraction becomes that large that defects on void surfaces dominate the density of defect states in the band gap.

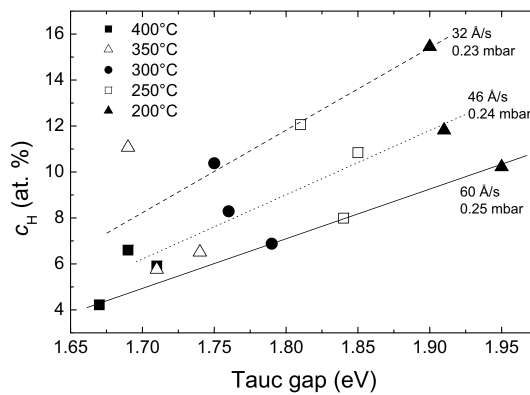

Figure 4.15: The H content, c_H, versus the Tauc band gap, E_{Tauc}. The linear relation between c_H and E_{Tauc} is strongly dependent on the reactor pressure and the substrate temperature. Lines are guide to the eye.

When the substrate temperature is increased, the variation of hydrogen content with reactor pressure (or growth rate) is smaller (see figure 4.15). A possibility is that at low substrate temperature, the precursors arriving on the surface have a low mobility and the probability that hydrogen abstraction from two adjacent Si-H bonds occurs is small. The formation of a highly strained Si-Si bonds at low temperature, in relation with the low precursor mobility, is more likely. Moreover, a higher pressure leads to a lower c_H for a given substrate temperature. This was already observed for the pressure series (see section 4.3.2). However, the thin films obtained at higher pressure are also less dense, which indicates that more voids are incorporated in the material, but also that these voids are not covered by hydrogen.

4.3.4 H_2 flow series

To find the optimum conditions for growing a-Si:H with a low defect density and a high photosensitivity, a series was deposited varying H_{2Noz} from 0 to 250 sccm (series V, see table 4.1 in section 4.2).

Apart from the growth rate that increases, due to the increase in reactor pressure with H_{2Noz}, no other changes are observed in the electro-optical properties of the material deposited at 400°C. The dark and light conductivities increase in the same proportion, leading to a constant photosensitivity. In figure 4.16, the Urbach energy, E_U, is plotted versus H_{2Noz} (full squares). After a slight decrease when some H_2 is injected into the nozzle, the Urbach energy starts to increase somewhat for flows in excess of or equal to 200 sccm, but it remains low (≤ 50 meV). Finally, no big changes in properties are observed for this material deposited at 400°C.

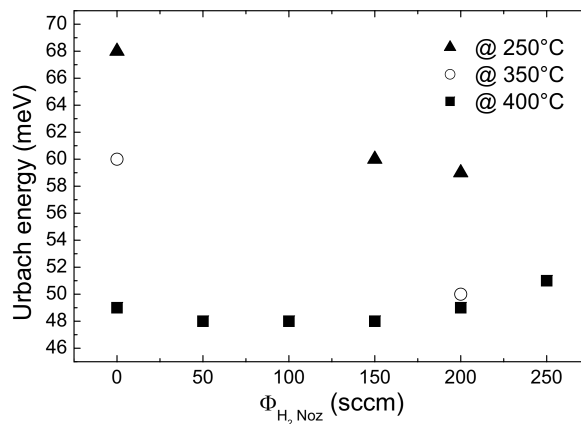

Figure 4.16: Urbach energy versus H_2 flow injected in the nozzle for three substrate temperatures.

The influence of H_2 in the nozzle becomes more appreciable when the deposition temperature is lower. As shown in figure 4.16, the Urbach energy drops with H_{2Noz} for deposition temperatures of 250°C and 350°C. This trend is more noticeable for low substrate temperatures. The defect density and the absorption coefficient at 1.2 eV, $\alpha_{1.2}$, are also minimized with H_{2Noz} but only if the substrate temperature is lower than 350°C (see table 4.2). However, we have to note that at lower substrate temperature, $\alpha_{1.2}$ is higher than at 400°C, even with H_{2Noz}. So the injection of H_2 in the nozzle cannot replace substrate temperature entirely.

T_{sub} (°C)	H_{2Noz} = 0 sccm	H_{2Noz} = 200 sccm
250	7.5	3.9
350	2.4	1.8
400	1.3	1.3

Table 4.2: Absorption coefficient $\alpha_{1.2}$ (cm^{-1}) taken at 1.2 eV.

In order to prevent the growth rate to increase due to the increase in reactor pressure, a second series was deposited (series VI) with the total H_2 flow kept constant. $\Phi_{H2\ Noz}/\Phi_{Tot\ H2}$, the ratio of hydrogen injected in the nozzle to the total hydrogen flow, was varied. The films were deposited at 400°C.

The fact that the reactor pressure and the total gas flow remain unchanged does not imply that the growth rate is not affected by the distribution of H_2 across the arc and/ or the nozzle. Actually, we observe a decrease in growth rate when $\Phi_{H2\ Noz}$ / $\Phi_{Tot\ H2}$ is increased. This decrease is accompanied by a drop in arc voltage, which means that the ionization of the species present in the arc is less effective. It appears that the atomic H formation is much more efficient in the arc than in the chamber. The opto-electronic properties are not affected by the $\Phi_{H2\ Noz}$ / $\Phi_{Tot\ H2}$ ratio, unless no H_2 is admitted in the arc at all. As seen in figure 4.17, the dark and light conductivities remain unchanged with varying $\Phi_{H2\ Noz}$ / $\Phi_{Tot\ H2}$, unless there is no H_2 in the arc. In that case, the light conductivity drops as well as the refractive index (not shown here). The growth rate is indeed boosted from 33 up to 134 Å/s and the defect density is multiplied by a factor 100 (see figure 4.18). This is thought to be due to the dominant process for SiH_4 dissociation. Instead of SiH_4 dissociation by atomic H abstraction, leading to SiH_3 formation [8], SiH_4 will be mainly decomposed by Ar^+ when no H_2 is injected in the arc, leading to dissociative recombination reactions with electrons and formation of clusters [1,9]. It is mentioned in literature [5] that these clusters are responsible for the growth of material of lower density, with higher defect densities and inferior electric properties.

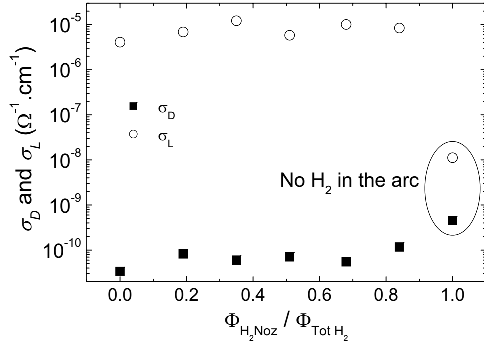

Figure 4.17: Dark and light conductivities versus the ratio of H_{2Noz} to total H_2 flow. T_{sub} = 400°C.

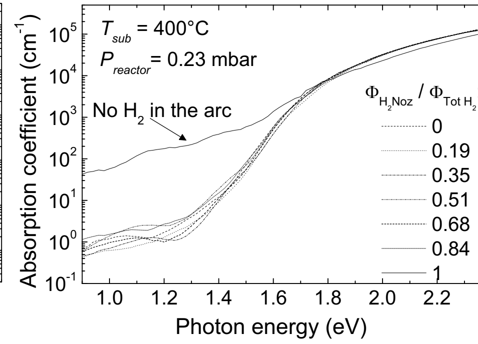

Figure 4.18: Absorption in the band-gap for several ratios of H_2 flow in the nozzle to that in the arc.

In conclusion, the process window for high deposition rate (> 2 nm/s) a-Si:H is quite large, and at a substrate temperature of 400°C it does not matter in which proportion H_2 is injected in the arc and the nozzle, as long as arc and nozzle are both used. At lower T_{sub}, the addition of H_{2Noz} improves parameters such as E_U and the sub band-gap absorption. We think that the excess of atomic H in the reactor, coming from dissociation of H_{2Noz}, helps the hydrogen abstraction from the surface, either directly by reaction of atomic H with surface-bonded hydrogen, either by the intermediate SiH_3, thereby creating less defects in the material.

Comparing the series with H_2 in the nozzle constant (series V) and the one with constant reactor pressure (series VI), we conclude that the optimum flow for a-Si:H deposited at high deposition rate is 200 sccm of H_2 both in the arc and in the nozzle, for 850 sccm of Ar.

4.3.5 Film density and hydrogen bonding type in the a-Si:H network

As shown by the large number of studies dedicated to it, hydrogen plays an important role in the formation of the a-Si:H network and thus in the properties of the grown material. Hydrogen atoms that bond to dangling bonds reduce the number of defects. It is known that pure a-Si, deposited for instance from sputtering, has a defect density of 10^{19} cm^{-3} and this density can be reduced down to 10^{15} cm^{-3} in a-Si:H. On one hand, hydrogen promotes a reconstruction of the network during growth, by breaking and removing weak Si-Si bonds and passivating dangling bonds. On the other hand, however, hydrogen is also held responsible for the material degradation under illumination. This phenomenon is known as the Staebler-Wronski effect [24]. The opto-electronic properties degrade under illumination and can be restored after annealing the a-Si:H films at temperature above 180°C. Another remarkable feature of

hydrogen is the fact that excess hydrogen in the plasma induces a transition to microcrystalline silicon. Before the transition to microcrystalline silicon occurs, the hydrogen content in a-Si:H films actually decreases when hydrogen is added to the plasma [25].

In the ETP technique, SiH_3 radicals are considered to be the main precursors for the a-Si:H growth [1]. Although the film surface is expected to be covered by hydrogen and the dangling bonds to be passivated, the bulk is hydrogen poor, with a hydrogen content of about 10 at.%. Furthermore, the solubility of hydrogen in a-Si is around 3 to 4 at.% [26]. A fundamental question is how the H-to-Si ratio drops from typically 2 to 4 in the gas phase down to 0.1-0.2 in the bulk. Several models have been proposed to explain how a hydrogen-rich surface, where the growth occurs, is 'transformed' in a low hydrogen content bulk. Robertson proposed a hydrogen elimination process based on rearrangement of H_2^* configurations in a region close to the surface [27]. This rearrangement, in combination with the chemisorption of SiH_3 radicals, brings enough energy for hydrogen elimination. However in his case, the growth rate is substantially lower than in our case and the hydrogen elimination process is thermo-dynamically limited instead of kinetically. Kessels *et al.* proposed the elimination of hydrogen based on a thermally activated hydrogen cross-linking step, right after the chemisorption of a silyl radical [19]. Smets found physical and chemical evidence in that direction [17]. However, these models do not take into consideration the hydrogen bonding type in the a-Si:H network and its influence on the a-Si:H properties.

Infrared absorption measurements provide much information about Si-H bonds, such as the total hydrogen content in the film and the configuration in which hydrogen is incorporated into the film (c_{HSM} and c_{LSM}). Smets *et al.* demonstrated that the film density of the ETP a-Si:H films was either vacancy- or void-dominated [28] depending on the hydrogen content. Silicon-hydrogen bonding configurations contributing to the low stretching mode (~2000 cm^{-1}) correspond to isolated (di-)vacancies, whereas configurations contributing to the high stretching mode (~2100 cm^{-1}) correspond to voids. He found that the film density is dependent on the total hydrogen content of the film, c_H, and he uses this dependence as a means to study the hydrogen bonding configuration in the material. The transition between the two regions is induced at c_H = 14 at.% and can be seen in figure 4.19 (open symbols). Samples containing less than 14 at.% H follow a linear relation between the film density, $\rho_{a\text{-}Si:H}$, and c_H, given by

$$\rho_{a\text{-}Si:H} = \rho_{a\text{-}Si}(1-\delta \cdot c_H) + \rho_H c_H \quad (15)$$

with δ the hydrogen incorporation parameter, $\rho_{a\text{-}Si}$ the pure a-Si volume density component and ρ_H the hydrogen volume density component. The samples with higher c_H obviously do not follow the same relationship and it was proved that these films are in the void density dominated region [28], which means that two hydrogen are bonded

to a silicon atom or that these hydrogen atoms are situated on void surfaces ($c_{HSM} > c_{LSM}$).

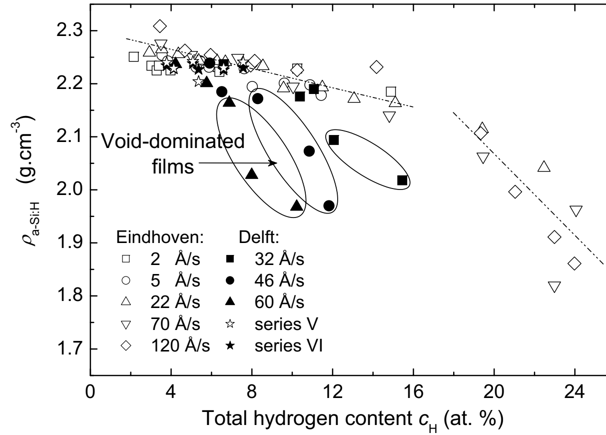

Figure 4.19: Film density versus hydrogen content obtained from the 640 cm^{-1} wagging mode for several growth rates; the a-Si:H films are either deposited in Eindhoven (open symbols) or in Delft (full symbols).

In figure 4.19, a-Si:H thin films grown in Delft at high growth rate and with H_2 injected in the nozzle are also plotted (full symbols). We can see that the Delft material does not match the trend previously observed for the Eindhoven material. Only samples deposited at substrate temperatures of 350°C or more are in agreement with the data from Eindhoven. It seems that c_H = 14 at.% is not the transition point in our case. When the hydrogen contents from the high and low stretching modes are plotted as a function of the total hydrogen content for each setting (figure 4.20), we observe that the transition from a vacancy- to a void-dominated region shifts as a function of the growth rate, so as a function of the reactor pressure. Table 4.3 summarizes the correspondence between growth rate, reactor pressure and critical hydrogen content delimiting the two structural regions.

Growth rate (Å/s)	Reactor pressure (mbar)	Critical hydrogen content (at.%)
32	0.23	~ 13
46	0.24	~ 9
60	0.25	~ 7

Table 4.3: Correspondence between growth rate, reactor pressure and critical c_H for a-Si:H films deposited in Delft.

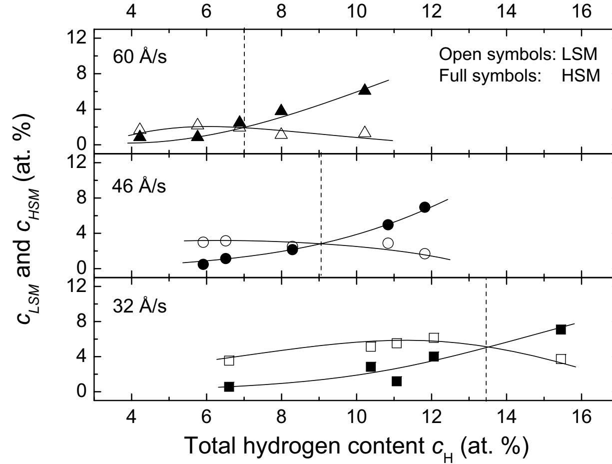

Figure 4.20: Stretching modes hydrogen content, c_{HSM} and c_{LSM}, plotted versus the wagging mode hydrogen content c_H for three growth rate series (from CASCADE set-up). Lines are guide to the eye.

It appears that there is a critical pressure at which this transition occurs. Andújar *et al.* [29] also observed a threshold pressure around 20 Pa for the transition between the α and γ regimes for rf PE-CVD. In the high-pressure region, the growth rate increases and the film density is reduced. Using rf PE-CVD, polymerization reactions that lead to poorer material quality can be suppressed by increasing the rf power. Higher powers lead to an increase in ion bombardment that enhances the surface mobility of adsorbed radicals and eliminates hydrogen bonded in SiH_2 configurations. In ETP-CVD, ion bombardment can be excluded, which means that the effect on the material properties of polymerization reactions occurring at higher pressures cannot be suppressed. For the Eindhoven material, the reactor pressure depends also on the deposition conditions and on the growth rate. However, we think that these reactor pressures are still low enough ($\leq$ 0.21 mbar) to not influence the structure of the deposited films. For the Delft material, the pressure in the reactor is higher (up to 0.25 mbar for the 60 Å/s series) and the structure of the material and the incorporation of hydrogen are then influenced. The critical hydrogen content, delimiting the vacancy-void regions, is then moved to lower c_H (figure 4.21). Consequently, some samples are grown in the void-dominated region although their hydrogen content is lower than 14 at.%, and this explains why they do not fit the vacancy-dominated samples from Eindhoven (see figure 4.19, full samples in a bubble).

In section 4.3.2, the influence of the reactor pressure on the material structural properties was established. At higher pressures, less hydrogen was incorporated in the

material. However, this study was carried out with samples deposited at 400°C. At this elevated substrate temperature, the density of the material follows the relationship with hydrogen content as described by equation (15). Only at lower temperatures, when less energy is supplied to the growing surface, the reactor pressure has an influence. This dependence of structural properties of the a-Si:H thin films on the reactor pressure and substrate temperature can be explained by the presence of polysilane radicals (e.g., Si_2H_p, $p \leq 6$) in the plasma chamber, which are hydrogen deficient radicals, or clusters (Si_nH_{2n+2}, $n \geq 2$). High pressures might give rise to gas phase polymerization reactions and thus powder formation [12]. The reactive polysilane radical contribution to the growth is then enhanced. As a consequence, the contribution of SiH_3 radicals to the growth is reduced. It has been reported that SiH_3 radicals are favorable for the growth of device-quality film because of their low surface reaction probability and their ability to diffuse on the surface. Polysilane radicals are known to lead to less compact material because they most likely stick to the surface on impact as their surface reaction probability is quite high (0.6 to 1) [13, 30]. Matsuda *et al.* postulated [31] that these higher silane-related reactive species form dihydride-rich subsurface structure, causing Si-H_2 rich bonding configuration in the resulting a-Si:H. Moreover, these polysilane radicals are known to stick preferentially on cold surfaces, which could explain why device-quality material can still be obtained at high substrate temperature and high reactor pressure. We think that with a high reactor pressure and a high deposition rate, more polysilane radicals contribute to the growth, therefore leading to poorer material properties.

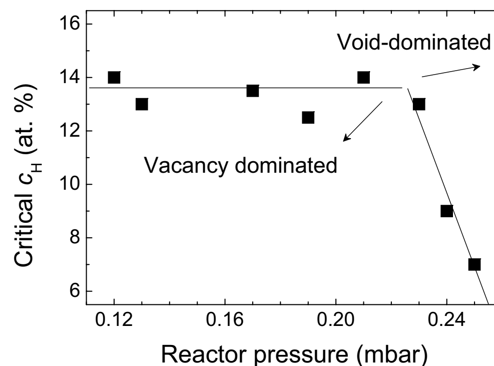

Figure 4.21: Dependence of the critical hydrogen content, for the transition between vacancy- and void- dominated regions, on the reactor pressure.

Figure 4.22 shows the light conductivity plotted versus the microstructure parameter R^* for samples deposited in Delft (full symbols) and in Eindhoven (open symbols). These samples are deposited under void-dominating conditions, as

determined earlier according to the hydrogen content and reactor pressure (see figures 4.19 and 4.20). We can see that the light conductivity decreases with increasing R^*. This suggests that the condition determined earlier for growing void- or vacancy-dominated material (transition for $c_{HSM} = c_{LSM}$), is valid. It indicates that the void surfaces act as recombination centers for the photocarriers. It was shown by photo deflection spectroscopy [32], as well as cavity ring down absorption spectroscopy [23], that the defect density of the a-Si:H surface is five orders of magnitude higher than for the bulk. This can give an indication of the defect density on the surface of the voids included in the bulk and explain the decrease of light conductivity with R^*.

The photosensitivity, σ_L / σ_D, of the Delft and Eindhoven a-Si:H samples is plotted versus R^* in figure 4.23. For the Delft samples (full symbols), the relationship found between σ_L and R^* can be seen for samples with a void-dominated structure. The dark conductivity is independent of the microstructure parameter. In general, the photosensitivity is higher for the Delft samples than for the Eindhoven ones, indicating that the Eindhoven samples have a higher dark conductivity. This implies a larger contamination in the Eindhoven samples than in the Delft ones by, e.g., oxygen from the background. The photosensitivity of device-quality a-Si:H varies typically from 10^4 up to 10^6.

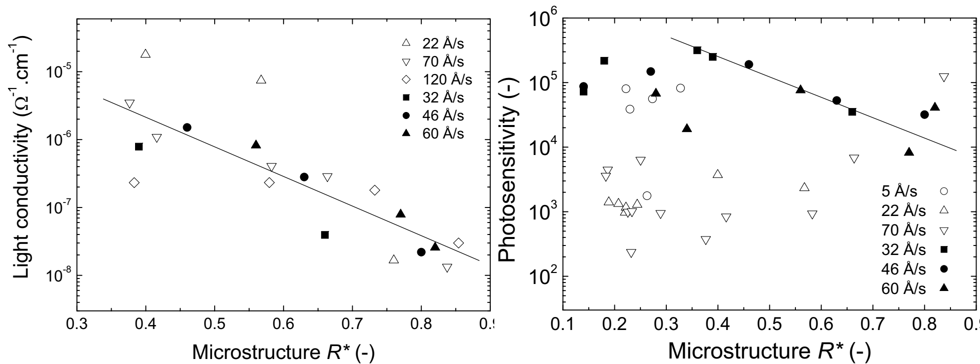

Figure 4.22: Light conductivity versus R^* for samples with a void-dominated density. Open symbols corresponds to Eindhoven samples, full symbols to Delft samples.

Figure 4.23: Photosensitivity σ_L/σ_D versus R^*, for all samples. Open symbols corresponds to Eindhoven samples, full symbols to Delft samples. The line is a guide to the eye.

In summary, the hydrogen bonding type in the a-Si:H network, determining if the material has a vacancy- or void-dominated structure, is very important to understand the structural and electric properties of the material [28]. It appears that not only the growth rate and the substrate temperature determine the structural properties of the growing material, but also the reactor pressure is very critical. The formation of polysilane or cluster ions in the plasma, which lead to the growth of less compact

material, is indeed attributed to higher reactor pressure. The incorporation of nano-voids results from a competition between the deposition rate (or the time to grow a monolayer) and the substrate temperature (or the time for radicals to diffuse on the surface, which is a thermally activated process). Smets *et al.* showed that for each growth rate there is a critical temperature above which compact material is obtained [17]. Here, we show that in addition to this critical temperature, also a critical reactor pressure, related to the growth flux, plays a role in the formation of the ETP-CVD a-Si:H structure. Above this critical pressure, the transition from one domain to the other (vacancy to void regions) is shifted to lower total hydrogen content and has as a consequence that although low c_H are obtained, the material is not compact. This is detrimental for the material properties, such as the photoconductivity (figure 4.22) and the defect density (figure 4.14). The latter increases for $R^* > 0.5$, i.e., for material in the void-dominated regime, whereas the N_d does not change for material grown in the vacancy-dominated region (i.e., $R^* < 0.5$).

4.4 Conclusions

We studied the properties of amorphous silicon deposited by ETP-CVD with extra H_2 injected directly in the reactor chamber via the nozzle, H_{2Noz}, in addition to H_2 flow in the arc. The aim was to reduce ion density emanating from the arc in order to minimize the growth contribution of polysilane radicals and silicon cluster ions, which are species with a low surface mobility and which deteriorate the quality of a-Si:H. We think that the Ar^+ ion density is decreased when passing through the H_{2Noz} 'curtain'. The growth rate is increased compared to material grown without H_2 in the nozzle, partly due to an increase in reactor pressure and reduction of the ETP beam diameter, partly due to the formation of extra radicals in the plasma.

As already observed for high growth rate deposition techniques, an increase of substrate temperature permits to improve the material properties, such as the light conductivity and defect density. The growth rate is slightly decreased when the substrate temperature is increased because of material densification. Remarkably, hydrogen content decreases with higher growth rate, but this is due to a higher pressure in the reactor. In addition, we observe that the microstructure of the material, R^*, decreases with increased substrate temperature and with lower growth rates and it appears that the light conductivity is strongly correlated to R^*. In fact, a-Si:H containing a high content of HSM configurations is less conductive due to defects on the surface of nano-voids incorporated in the material that operate as recombination centers. The defect density is also correlated to the material microstructure. A higher density of voids in the material entails more defect states in the band gap. However, for samples with R^* below 0.5, N_d is independent of R^*; the material is grown in the vacancy-dominated regime.

By studying the hydrogen bonding type in the a-Si:H network, it turns out that the transition between vacancy- and void-dominated density a-Si:H can be monitored with the hydrogen content for moderate reactor pressures (≤ 0.21 mbar) and that the critical c_H equals 14 at.%. However, this critical c_H shifts to lower values when higher reactor pressures are used. This is thought to be due to the presence of polysilane radicals and cluster ions in the plasma that contribute in a larger extent to the growth under high reactor pressure conditions and higher growth rates.

We conclude that device quality a-Si:H can be deposited at high growth rates with ETP-CVD (> 30 Å/s) when H_2 is added in the nozzle and when the substrate temperature is above 300°C.

References

[1] W.M.M. Kessels, C.M. Leewis, M.C.M. van de Sanden and D.C. Schram, J. Appl. Phys. **86** (1999) 4029

[2] B.A. Korevaar, Ph.D. thesis, Eindhoven University of Technology (2002)

[3] M.C.M. van de Sanden, R.J. Severens, W.M.M. Kessels, R.F.G. Meulenbroeks and D.C. Schram, J. Appl. Phys. **84** (1998) 2426

[4] W.M.M. Kessels, M.C.M. van de Sanden and D.C. Schram, J. Vac. Sci. Technol. A **18** (2000) 2153

[5] H.A. Weakliem, R.D. Estes and P.A. Longeway, J. Vac. Sci. Technol. A **5** (1987) 29

[6] W.M.M. Kessels, M.G.H. Boogaarts, J.P.M. Hoefnagels, D.C. Schram and M.C.M. van de Sanden, J. Vac. Sci. Technol. A **19** (2001) 1027

[7] M.C.M. van de Sanden, R.J. Severens, J. Bastiaanssen and D.C. Schram, Surf. Coat. Technol. **97** (1997) 719

[8] A. Goumri, W.J. Yuan, L. Ding, Y. Shi and P. Marshall, Chem. Phys. **177** (1993) 233

[9] J. Perrin, O. Leroy and M.C. Bordage, Contrib. Plasma Phys. **36** (1996) 3

[10] A. Matsuda, M. Matsumura, S. Yamasaki, H. Yamamoto, T. Imura, H. Okushi, S. Iizima and K. Tanaka, Jpn. J. Appl. Phys. **20** (1981) L183

[11] R.C. Ross and J. Jaklik Jr., J. Appl. Phys. **55** (1984) 3785

[12] M.H. Brodsky, Thin Solid Films **40** (1977) L23

[13] S. Ramalingam, E.S. Aydil and D. Maroudas, J. Vac. Sci. Technol. B **19** (2001) 634

[14] J.C. van den Heuvel, M.J. Geerts and J.W. Metselaar, Sol. Energy Mater. **22** (1991) 185

[15] A.H. Mahan, Y. Xu, D.L. Williamson, W. Beyer, J.D. Perkins, M. Vanecek, L.M. Gedvilas and B.P. Nelson, J. Appl. Phys. **90** (2001) 5038

[16] W.M.M. Kessels, R.J. Severens, A.H.M. Smets, B.A. Korevaar, G.J. Adriaenssens, D.C. Schram and M.C.M. van de Sanden, J. Appl. Phys. **89** (2001) 2404
[17] A.H.M. Smets, W.M.M. Kessels and M.C.M. van de Sanden, Appl. Phys. Lett. **86** (2005) 041909-1
[18] W.M.M. Kessels, M.C.M. van de Sanden, R.J. Severens, L.J. van IJzendoorn and D.C. Schram, Mater. Res. Soc. Symp. Proc. **507** (1998) 529
[19] W.M.M. Kessels, R.J. Severens, M.C.M. van de Sanden and D.C. Schram, J. Non-Cryst. Sol. **227** (1998) 133
[20] W.M.M. Kessels, A.H.M. Smets, D.C. Marra, E.S. Aydil, D.C. Schram and M.C.M. van de Sanden, Thin Solid Films **383** (2001) 154
[21] A.H. Mahan, D.L. Williamson, B.P. Nelson and R.S. Crandall, Phys. Rev. B **40** (1989) 12024
[22] K. Koga, N. Kaguchi, K. Bando, M. Shiratani and Y. Watanabe, Rev. Sci. Instr. **76** (2005) 113501
[23] A.H.M. Smets, J.H. van Helden and M.C.M. van de Sanden, J. Non-Cryst. Sol. **299** (2002) 610
[24] D.L. Staebler and C.R. Wronski, Appl. Phys. Lett. **31** (1977) 292
[25] N.M. Johnson, S.E. Ready, J.B. Boyce, C.D. Doland, S.H. Wolff, J. Walker, Appl. Phys. Lett. **53** (1988) 1626
[26] S. Acco, D.L. Williamson, P.A. Stolk, F.W. Saris, M.J. van den Boogaard, W.C. Sinke, W.F. van der Weg, S. Roorda and P.C. Zalm, Phys. Rev. B **53** (1996) 4415
[27] J. Robertson, J. Appl. Phys. **87** (2000) 2608
[28] A.H.M. Smets, W.M.M. Kessels and M.C.M. van de Sanden, Appl. Phys. Lett. **82** (2003) 1547
[29] J.L. Andújar, E. Bertran, A. Canillas, C. Roch and J.L. Morenza, J. Vac. Sci. Technol. A **9** (1991) 2216
[30] W.M.M. Kessels, M.C.M. van de Sanden, R.J. Severens and D.C. Schram, J. Appl. Phys. **87** (2000) 3313
[31] A. Matsuda, M. Takai, T. Nishimoto and M. Kondo, Sol. Energy Mat. & Sol. Cells **78** (2003) 3
[32] G. Amato, G. Benedetto, L. Boarino and R. Spagnolo, Appl. Phys. A **50** (1990) 503

Chapter 5

External rf substrate-biased ETP for deposition of high-quality a-Si:H

5.1 Introduction

The role of ions in the a-Si:H growth mechanism and the effects of surface-ion interactions on ETP-CVD a-Si:H are not yet entirely understood. Polysilane radicals and ion clusters might have a large impact on the a-Si:H properties, although their contribution to the growth is estimated to a maximum of 10% [1]. We saw in the previous chapter that the addition of H_2 in the nozzle permits to improve the material quality, which is believed to be linked to the reduction of the high-degree silane radical and cluster ion densities. In this chapter, we use the ionic species present in the plasma to bombard the surface during growth and we study the influence of this bombardment on the properties of a-Si:H deposited at low substrate temperature.

At high deposition rates (> 10 Å/s), relatively high substrate temperatures are required to supply additional energy to the growth precursors in order to enhance their surface diffusion with respect to their arrival rate, permitting to obtain dense material [2]. These high substrate temperatures can be a source of difficulties when the intrinsic a-Si:H film is incorporated in a p-i-n solar cell. The underlying a-Si(C):H p-layer is sensitive to high temperatures and the material properties may be significantly affected when exposed to temperatures above 250°C. For this reason it is desired that extra energy is supplied to the growing surface by an alternative method rather than by using

a high substrate temperature. This extra energy supply can be realized by bombarding the surface with energetic ions.

In the ETP technique, the plasma is at a remote location and ions emanating from the arc expand in the reactor, arriving on the deposition surface with little energy (< 2 eV). Therefore, in contrast to a-Si:H growth with rf PE-CVD, the growth of a-Si:H by ETP-CVD occurs without ion bombardment. It was shown by Takagi [3] that using an accelerated ion beam increases the migration of adatoms during deposition without actually heating the substrate. Ion energies as low as few eV are expected to have similar effect as temperature [4,5]. Therefore ion bombardment, by applying an external rf biasing during ETP-CVD a-Si:H deposition, can be a means to provide extra energy to the surface, hence permitting to grow thin films fast at lower substrate temperatures.

In this chapter, we first present the properties of a-Si:H deposited with rf-biased ETP-CVD as a function of the bias voltage generated on the substrate. Then we will present the differences and similarities of rf-bias and substrate temperature. Finally, in the last section, we will discuss the different processes occurring under ion bombardment and the consequences on a-Si:H growth in terms of ion energy.

5.2 Experimental details

The a-Si:H samples used in the present study were prepared with the ETP technique in the multichamber deposition system CASCADE. The plasma was operated with a gas mixture of Ar-H_2-SiH_4. The ion bombardment was generated by applying an rf power (13.56 MHz) to the substrate holder. A more detailed description can be found in Chapter 2 of this thesis.

The thin films were deposited on Corning glass 1737 for optical and electric characterization by reflection-transmission (RT) and dual-beam photoconductivity (DBP) techniques and on crystalline silicon for structural characterization by Fourier transform infrared (FTIR) absorption spectroscopy. The following series were deposited:

Power series: three series were deposited, one with 150 sccm H_2 injected in the nozzle (series I), one without extra H_{2Noz} (series II) and a last one at higher growth rate with H_{2Noz} (series III). The rf power applied on the substrate holder was varied from 0 to 50 W, which corresponds to a bias voltage $|V_{dc}|$ varying between ~ 0.5 and 53 V. The gas flow settings and other deposition conditions can be found in table 5.1.

Temperature series: two series were deposited, one without rf-bias (series IV) and one with 8-W rf-bias on the substrate (series V). In both cases, 150 sccm H_2 was injected in the nozzle. The substrate temperature, T_{sub}, was varied from 150°C to 400°C. The other deposition conditions can be found in table 5.1.

Series	Ar (sccm)	$H_{2\,Nozzle}$ (sccm)	$H_{2\,Arc}$ (sccm)	SiH_4 (sccm)	Tempera-ture (°C)	RF power (W)	$\|V_{dc}\|$ (V)	Growth rate (Å/s)
I	600	150	200	200	250	varied	varied	11.8
II	600	0	200	200	250	varied	varied	12.0
III	850	150	200	200	250	varied	varied	40.0
IV	600	150	200	200	varied	0	~0.5	11.3
V	600	150	200	200	varied	8	24	11.8

Table 5.1: Overview of the deposition conditions used in this chapter. Note that the growth rate is the average growth rate for each series.

In addition, for all the deposition conditions mentioned above, 400 sccm He was used as back flow in order to control the substrate temperature accurately. The arc current was set at 40 A and the pressure in the arc was p_{arc} = 0.41-0.43 bar, except for series III where p_{arc} = 0.54 bar. The pressure in the reactor chamber, $p_{reactor}$, was respectively 0.18 mbar for series II, 0.20 mbar for series I, IV and V and 0.23 mbar for series III when no bias was applied on the substrate. When rf biasing was applied, it was not possible to determine $p_{reactor}$ accurately, because of interferences from the rf-signal with the pressure gauge.

5.3 Results

5.3.1 RF power series

The dc bias voltage, V_{dc}, generated when applying an external rf power, P_{rf}, on the substrate holder was measured for three plasma conditions (see figure 5.1). For a pure Ar plasma, V_{dc} exhibits a linear dependence on P_{rf}. This means that all the rf power is used to accelerate the ions within the plasma sheath and the ion current is constant considering the relation $P_{rf} \sim I_{ion}V_{dc}$ [6]. When H_2 is added to Ar in the reactor, the dependency between V_{dc} and P_{rf} is no longer linear and part of the rf power is used to create an extra plasma above the substrate, generating a bright light. We think that this secondary plasma comes from the formation of excited species and their subsequent decay. These excited species were generated by collision of neutral species with heated electrons around the substrate holder. The generation of secondary electrons is twofold. First of all, the rf bias provides extra energy to the electrons crossing the sheath and efficiently heats the electron gas, leading to a higher ionization of species around the substrate. And secondly, the other possibility could be, although to a lower extend, that some secondary electrons are ejected from the substrate surface when energetic particles impinge on it and transfer their kinetic energy to this surface. These secondary electrons may ionize or excite neutral particles close to the surface and

contribute to the generation of the bright light observed around the substrate. Finally, when SiH_4 is added to the gas mixture, an extra plasma also appears, characterized by a higher $|V_{dc}|$ than in the pure Ar case and by an additional light emission above the substrate. The bias voltage obtained when SiH_4 is introduced into the reactor is lower than in the case of Ar with H_2, because SiH_4 is easier to ionize than H_2 and therefore the current is higher. As a consequence, the electron density is also higher, and this results in a lower bias for a given power.

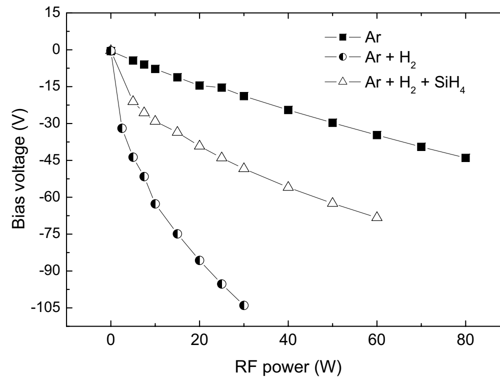

Figure 5.1: Bias voltage, V_{dc}, measured at the substrate holder versus the applied rf power for respectively an Ar, Ar-H_2 and Ar-H_2-SiH_4 plasma.

The extra plasma created when applying an rf power to the substrate enhances the a-Si:H growth as shown in figure 5.2. The growth rate increases as a function of the dc bias voltage for various deposition settings. This deposition-rate increase can be due to a larger SiH_3 radical density in front of the substrate [7], generated by the extra plasma, thereby increasing the Si growth flux. SiH_3 radicals are generally considered as the main precursors in a-Si:H growth. In addition, positive ions containing silicon atoms ($Si_mH_n^+$), which are impinging onto the growing surface, can contribute to film growth [8], although only in a moderate proportion (< 9%). Smets *et al.* observed a growth flux saturation for self-bias voltages in excess of 60 V [6]. In our case, the series deposited at high growth rate (series III, deposited at 250°C) does not show a clear indication of saturation, but the maximum investigated power voltage was 55 V.

Despite this increase in growth rate, the refractive index, n_{2eV}, remains constant for a wide range of $|V_{dc}|$ (Fig. 5.3). The refractive index is a measure of the mass density of the deposited films and thus an increase in n_{2eV} indicates an increase in material compactness. We can notice a slight increase in the refractive index for bias voltages around 21 V. This increase is in good agreement with the improvement in electric properties of a-Si:H thin films deposited by rf PE-CVD and the grid-bias method, reported by Kato and Ganguly [9] when ions have an energy between 23 and 24 eV.

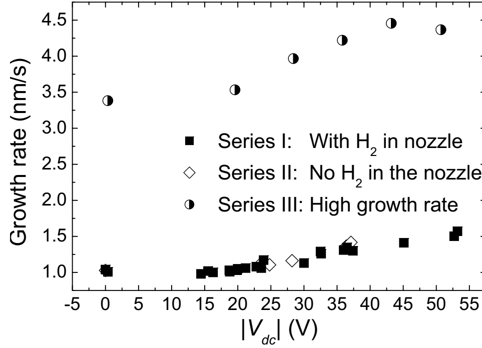

Figure 5.2: Growth rate of the thin films versus bias voltage.

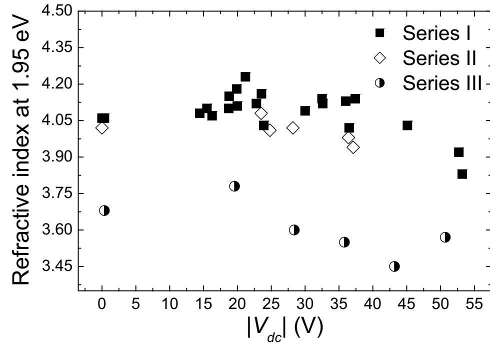

Figure 5.3: Refractive index, n_{2eV}, of the thin films versus bias voltage.

In figure 5.3, open diamonds represent samples deposited without H_2 in the nozzle (series II). These samples have a lower refractive index than those deposited with H_{2Noz}, irrespective of the rf power used. It confirms that the H_{2Noz} has a beneficial effect on the properties of a-Si:H. For high-energy ion bombardment ($|V_{dc}| > 45$ V), the refractive index decreases. For series III, this decrease in refractive index is found already for low V_{dc} values and $|V_{dc}| = 20$ V is the optimum condition. The improvement in refractive index as a function of V_{dc}, followed by a decrease, is a sign that two processes are competing when an external rf substrate biasing is applied: (i) energy transfer of the surface-impinging ions to the radicals increasing their surface mobility, which is dominant at low-energy ion bombardment, and (ii) sputtering or displacement of Si atoms from the sub-surface, decreasing the density of the thin film, which is prominent at high-energy ion bombardment [10]. The first process has a positive influence on the material properties, whereas the second process leads to poorer material quality.

As reported in table 5.2, the dark-conductivity activation energy of the thin films is rather high for intrinsic a-Si:H material. The activation energy increases substantially when substrate biasing is applied and exceeds half of the Tauc band gap value. This increase in activation energy does not correspond to an increase in band gap, which either remains constant or slightly decreases when varying $|V_{dc}| = 0.5$ to 36 V (or $P_{rf} = 0$ to 60 W), but is attributed to a shift of the Fermi level towards the valence band. We expect either a higher donor-like dangling bond states in the band-gap or a broadening of the conduction band tail. Therefore the material is slightly p-like doped. This behavior is rather surprising as usually the Fermi level of intrinsic a-Si:H is reported to be slightly above midgap, giving a n-type behavior to the material. This n-type behavior is due to either the higher mobility of electrons compared to holes [11], or to the incorporation of oxygen or nitrogen impurities [12]. The dark

conductivity is correspondingly low at $1 \times 10^{-12}\ \Omega^{-1}.\mathrm{cm}^{-1}$. The light conductivity remains constant within the measurement accuracy (Table 5.2). Akiyama *et al.* showed that for a-Si:H deposition by ECR (Electron Cyclotron Resonance) plasma CVD [13] the concentration of $(SiH_2)_n$ chains in the deposited film dominates the photo-conductivity. An increase in microwave power permits to reduce the cluster chains incorporation in the material and this is attributed to an increase of energy transfer of the incident ions to the film surface. A high photosensitivity is maintained in all cases.

$\lvert V_{dc} \rvert$ (V)	E_{act} (eV)	σ_{Dark} ($\Omega^{-1}.\mathrm{cm}^{-1}$)	σ_{Light} ($\Omega^{-1}.\mathrm{cm}^{-1}$)	*Photosensitivity* (-)
~ 0.5	0.879	9.5×10^{-13}	2.0×10^{-6}	2.1×10^{6}
18.8	0.966	1.0×10^{-12}	2.8×10^{-6}	2.8×10^{6}
22.8	0.946	5.2×10^{-13}	3.1×10^{-6}	6.0×10^{6}
32.6	0.960	8.7×10^{-13}	2.1×10^{-6}	2.4×10^{6}
52.7	0.910	1.9×10^{-12}	3.1×10^{-6}	1.6×10^{6}

Table 5.2: Electronic properties of a-Si:H for several values of $\lvert V_{dc} \rvert$, series I.

In figure 5.4, the Urbach energy, E_U, is shown as function of the bias voltage. We do not observe a strong trend for the series deposited with H_{2Noz} at ~ 1 nm/s, but what is remarkable is that as soon as an rf bias is applied, E_U is decreased, irrespective of the rf power applied to the substrate. For samples deposited without H_{2Noz}, the rf bias does not improve E_U. Finally, for the samples deposited at higher growth rate (> 3 nm/s), applying an external bias results in the increase of the Urbach energy, except for a low self-bias of 20 V. This corresponds to the best value found for the refractive index.

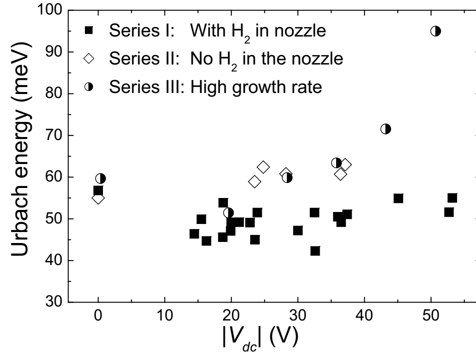

Figure 5.4: Urbach energy E_U versus bias voltage for various deposition conditions.

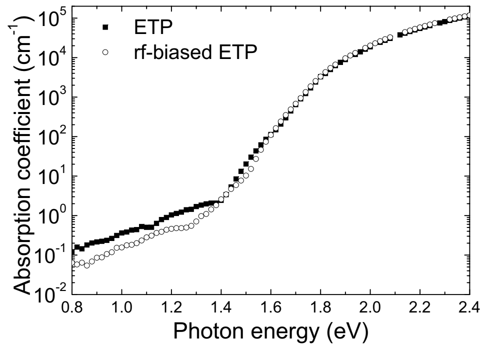

Figure 5.5: Absorption coefficient vs. photon energy for samples deposited at 250°C with and without external rf bias ($\lvert V_{dc} \rvert$ = 24 V).

The absorption coefficient obtained from RT and DBP measurements for a-Si:H films deposited at 250°C from series I is shown in figure 5.5. The sample deposited with an external rf bias ($|V_{dc}|$ = 24 V) shows a smaller sub gap absorption than the sample deposited without rf bias. This observation implies that with moderate ion bombardment fewer defects are incorporated into the material thanks to the extra energy brought by the ions.

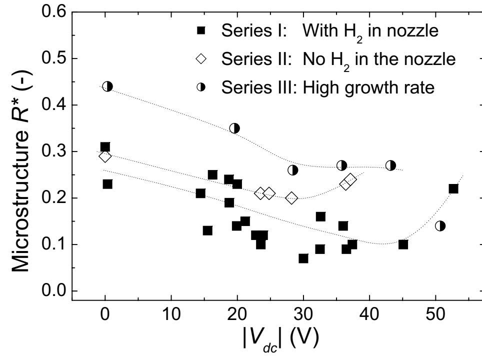

Figure 5.6: Microstructure R^* versus external dc bias for a-Si:H films deposited at various conditions. Lines are guide to the eye.

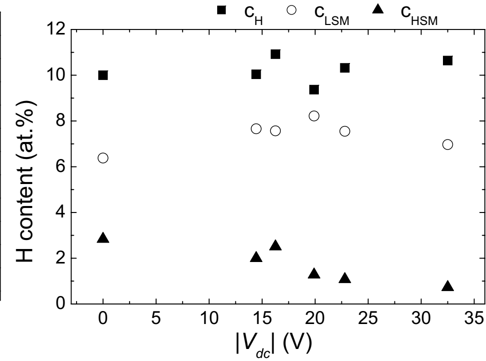

Figure 5.7: H content versus bias voltage for the standard deposition conditions (Series I, ~ 1 nm/s, 250°C, H_2 in nozzle).

The microstructure R^* of the a-Si:H films was calculated from fitting the FTIR spectra. Attention was paid to the integrated absorption of the low stretching mode (LSM, 1980-2010 cm^{-1}) and of the high stretching mode (HSM, at 2070-2100 cm^{-1}) and to the R^* value. From figure 5.6, it is clear that ion bombardment has an important influence on the microstructure of the material. One of the criteria for device-quality a-Si:H is that the R^* value is lower than 0.1 [14] and we can see that this condition is fulfilled for standard material (series I) when a $|V_{dc}|$ of about 20-30 V is applied to the substrate. For samples deposited at high growth rate or with no H_{2Noz}, R^* is still above 0.1 within the studied range, although an rf-bias improves the R^* value. We point out that these samples are deposited at a low substrate temperature of 250°C. We have to note that the R^* value of the point at 51 V of series III is probably erroneous as the other material properties of this particular sample (E_U, absorption coefficient at 1.2 eV) indicate that this material is inferior compared to the rest of the series.

The hydrogen content, c_H, determined from the 640 cm^{-1} peak of the IR absorption spectrum, scatters between 8 and 11 at.% and the hydrogen content in the low stretching mode, c_{LSM}, slightly increases in that range as is shown in figure 5.7 (for clarity, only one of the series deposited with H_{2Noz} is shown). Therefore, the decrease in R^* is representative of the decreasing hydrogen content in the high stretching mode, c_{HSM}. This means that the void incorporation in a-Si:H is reduced when the growing

surface is bombarded by energetic ions. A low external substrate bias is already sufficient to decrease the R^* value from 0.3 to 0.1 for the conditions where hydrogen is injected into the nozzle (series I). We think that ion bombardment, by enhancing the radical surface diffusion, promotes hydrogen desorption from the surface during growth. However, when a higher dc bias is applied (> 35 V), the R^* value increases again. The growth rate is increased and the a-Si:H network becomes less ordered. We conclude that a mild self-bias voltage is sufficient to make the growth surface reactive without damaging the structure.

5.3.2 Temperature series

The effect of rf biasing is sometimes compared to that of temperature [4], as extra energy is brought to the growing surface and the radical mobility is therefore increased. However, ion bombardment might have other effects on the species in the plasma and on the grown material. We can think that energetic ions can break big clusters close to the surface into smaller entities, thereby reducing the contribution of polysilane to the growth. Alternatively we can think that the energetic ions can leave the polysilanes intact but increase their mobility on the surface so they can hop and reach a more thermodynamically favorable sticking site. It is interesting to investigate to which extent temperature and ion bombardment are interchangeable in the ETP deposition technique.

To study this correlation, two series as function of substrate temperature have been deposited, one by standard ETP at 11 Å/s (series IV) and the second one with an rf bias of 8 W, corresponding to a bias voltage of 24 V (series V). The growth rate in this case is 12 Å/s on average. The substrate temperature was varied between 150°C and 400°C. See table 5.1 for the deposition conditions.

As shown in figure 5.8, n_{2eV} increases when the substrate temperature is increased from 150°C up to 400°C, which indicates that a more compact material is grown. For material grown with rf-biased ETP, the same trend is observed, but the refractive index is higher. Comparing the curves in figure 5.8, we can see that a material with the same refractive index can be obtained at lower substrate temperatures when rf-biasing is applied. The extra energy brought by the ions ($|V_{dc}|$ = 24 V in this case) permits to deposit a-Si:H thin films of same refractive index at substrate temperatures ~ 50°C lower than without rf bias.

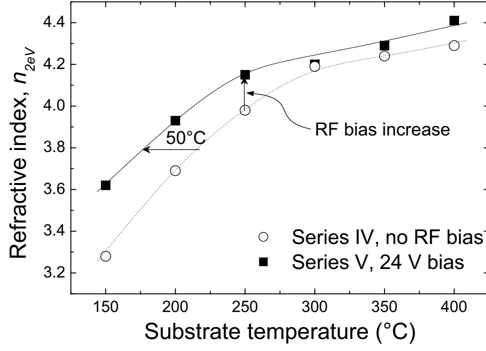

Figure 5.8: Refractive index taken at 2 eV versus T_{sub}. Layers deposited with ETP (open symbols) or rf-biased ETP (full symbols) with $|V_{dc}|$ = 24 V.

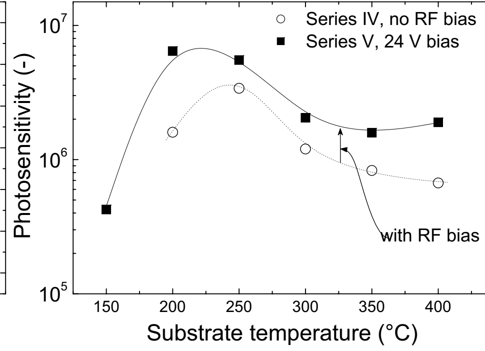

Figure 5.9: Photosensitivity (σ_L/σ_D) versus T_{sub} for layers deposited with ETP (open symbols) or rf-biased ETP (full symbols) with $|V_{dc}|$ = 24 V.

The light conductivity, σ_L, as well as the dark conductivity, σ_D, increases with substrate temperature. The increase in σ_D is directly linked to a narrower optical band gap (Tauc gap decreases from 1.90 eV at 150°C down to 1.72 eV at 400°C) [15]. The increase in σ_L is related to a lower density of states in the band gap. However, the addition of rf bias on the substrate enables σ_L to increase only for samples prepared at temperatures lower than 300°C. The defect density, however, is always lower with rf-bias (as shown in Fig. 5.11), independently of the substrate temperature. The best σ_L obtained is ~ 5×10^{-6} Ω^{-1}.cm^{-1}. As the defect density remains unchanged for T_{sub} > 250°C, we think that the electron mobility is reduced. The relative low σ_L obtained suggests the presence of either deep traps for electrons (deeper in the gap than 0.8 eV, as no increase in defect density is observed, see Fig. 5.11) or of a lot of shallow traps, that in both cases reduce the electron mobility. Time-of-flight measurements showed indeed an electron drift mobility at room temperature of 0.1 cm^2.V^{-1}.s^{-1}, which is one order of magnitude smaller than in standard rf PE-CVD a-Si:H [16], and this low electron mobility could be the limiting factor for the photoconductivity. The photosensitivity, which is defined as the ratio between the σ_L and σ_D, has a maximum for substrate temperatures around 200-250°C (Fig. 5.9). It is interesting to note that a mild rf bias of 24 V leads to an improvement in photosensitivity and that the optimum substrate temperature concerning the photosensitivity is then lowered from 250°C down to 200°C.

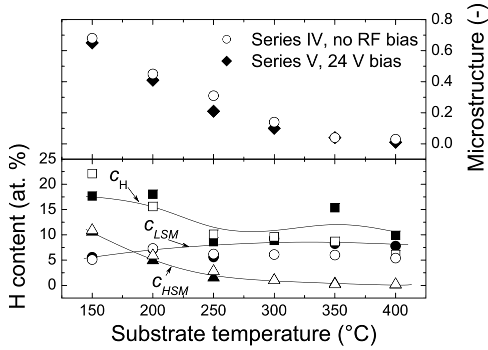

Figure 5.10: Hydrogen content (c_H, c_{LSM} and c_{HSM}) and microstructure R^* versus T_{sub}. Open symbols: standard ETP, full symbols: rf-biased ETP ($|V_{dc}|$ = 24 V).

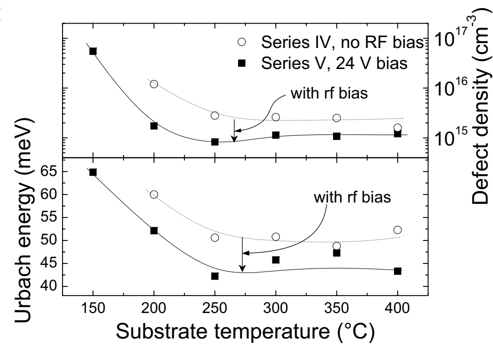

Figure 5.11: Urbach energy and defect density versus T_{sub} for samples deposited with and without rf bias ($|V_{dc}|$ = 24 V).

The total hydrogen content, c_H, is strongly dependent on T_{sub} (see Fig. 5.10) and the microstructure parameter R^* also decreases drastically with T_{sub}. Surprisingly, rf bias on the substrate does not reduce R^* further at temperatures above 300°C.

On average each ion is accelerated with an energy of 24 eV in the conditions chosen here. However, when considering the ion-energy distribution, some ions possess a higher energy. These ions may be responsible, for example, for weak-bond breaking.

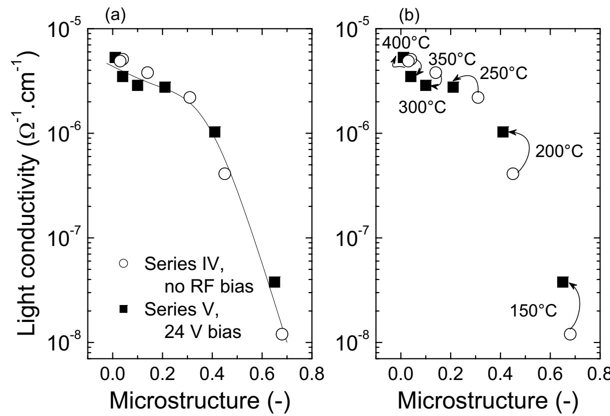

Figure 5.12: Light conductivity versus R^* for the temperature series IV and V. (a) Effect of rf bias on the general trend (line is a guide to the eye); (b) with substrate temperature taken into account.

In that case, ion bombardment not only leads to a higher surface mobility of radicals, which we think is equivalent to higher substrate temperature, but also to the removal of loosely bonded atoms, leading to a better structure of the material. This can be seen in figure 5.11 in which both the Urbach energy, E_U, and the defect density in the sub-band gap, N_d, are presented. E_U and N_d not only decrease with higher T_{sub}, but also when an rf bias is applied to the substrate at a given temperature. At 250°C, N_d decreases a factor 3 with a bias voltage of 24 V to values obtained only at 400°C without rf bias.

Figure 5.12 (a) presents the dependence of the light conductivity on the microstructure parameter. At a first glance, the addition of an external rf bias on the substrate seems not to influence their dependence and the lower *R**, the higher σ_L. However, when attention is paid to the specific substrate temperature for each point (Fig. 5.12 (b)), it appears that the addition of rf bias leads higher σ_L and lower *R** at a given temperature below 300°C. Above that temperature, *R** is still reduced, but then σ_L remains more or less constant compared to the case without rf bias. RF-biased ETP gives rise to the same material properties while lowering the substrate temperature, although this is obvious only at substrate temperatures below 300°C.

It is interesting to note that the bias voltage $|V_{dc}|$, measured on the substrate holder, increases when the substrate temperature is increased from 150°C to 400 °C, although the input rf power is kept constant (see Fig. 5.13). This increase might be due to the heating of the gas in the vicinity of the surface, making the ionization of the species easier and leading to an increased electron density. In that case, the ion bombardment is slightly more efficient at higher substrate temperatures, as the mean ion energy is increased.

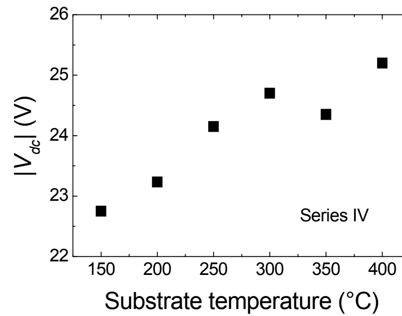

Figure 5.13: Substrate self-bias voltage $|V_{dc}|$ versus temperature. The applied rf bias was kept constant at 8 W.

In conclusion, with an external rf bias similar properties as those obtained with samples deposited without bias can be obtained, but at lower substrate temperatures (~ 50°C lower). However, temperature and rf bias are not completely interchangeable as ion bombardment can modify the plasma composition and reduce the incorporation

of polysilane in the film, as the energetic ions might break down polysilane clusters. Thereby the quality of the material is improved. Moreover, ion bombardment can lead to atom displacement (E_{ion} = 12.9 eV, [17]) or even silicon sputtering (E_{ion} = 80 eV, [18]), depending on the ion energy. These two features can potentially occur as a broad ion energy distribution function, around the mean energy eV_{dc}, is expected [19]. The ordering of the a-Si:H network is then improved and lower defect densities are achieved. Finally, at high substrate temperature (> 300°C), the beneficial effect of ion bombardment seems to be masked by the temperature effect and no further improvement is noticed concerning, e.g., the light conductivity, σ_L, that remains relatively low (< 10^{-5} Ω^{-1}.cm^{-1}).

5.4 Discussion

When an external rf bias is applied on the substrate during ETP-CVD deposition, the positive ions present in the plasma bulk will undergo an acceleration towards the substrate when crossing the sheath. As the ions have a larger mass than the electrons and a lower mobility, they react slower to the changes in electric field and to the rf signal. A negative dc bias is then generated on the substrate. Consequently, the positive ions will impinge on the growing surface, and this will result in ion bombardment. What is the nature of the ionic species involved in this process and what are the effects of such a bombardment on a-Si:H growth?

Nature of the ions bombarding the surface:

As mentioned earlier, under ETP condition without rf-biasing, no or negligible ion bombardment is taking place, although ions are present in the plasma. In particular hydrogen-poor cationic clusters, $Si_nH_m^+$, have been identified as growth precursors that contribute up to 5% of the a-Si:H growth [8]. Therefore, the contribution of large Si clusters to a-Si:H growth cannot be excluded.

With rf bias, the cationic clusters are thought to be either accelerated to the surface or broken up in smaller species before reaching the surface. It is very unlikely that these large ions can penetrate into the bulk. However, smaller ions can induce film modifications and material properties alteration. In other words, other ions than cationic clusters are expected to be mainly responsible for the energy transfer to the growth surface. The additional ions generated in front of the substrate are most likely SiH_n^+ or Ar^+ [20]. These ions are thought to dominate the surface bombardment. A domination of H^+ ions would lead to less efficient Si displacement due to their smaller mass. However the presence of H^+, $H_2^+$and H_3^+ ions has been observed in the plasma, which means that they can participate to the surface bombardment.

We know from previous studies that deposition of a-Si:H by ETP-CVD without rf bias is dominated, at more than 90%, by SiH_3 radicals [21]. The growth contribution

of these radicals during ETP-CVD with rf bias remains the same according to Hoefnagels *et al.* [7] and the growth contribution of $Si_nH_m^+$ ions is limited to ~ 6% [8].

Influence of ion bombardment on the growth rate:

When an external rf bias is applied, an additional plasma is observed close to the substrate surface. The extra plasma observed around the substrate holder is attributed to the electron temperature in the plasma that increases and, to some extent, to secondary electrons that are released from the surface following ion collision onto the surface. The higher electron density increases the dissociation degree of the H_2 and SiH_4 molecules present in the plasma [6], generating more radicals in the vicinity of the substrate surface. This higher radical density was confirmed by Hoefnagels *et al.* by time-resolved cavity ring down spectroscopy [7]. The increase in radical density close to the surface has as a consequence an increase in growth rate. Note that the increase in growth rate is not attributed to a decrease in compactness of the material as the density ρ remains more or less constant with increasing rf bias. The growth-rate increase, as a result of the radical-density increase, is substantiated by the fact that the growth flux, Γ, increases by 33% while the growth rate increases by 33.5%. Ando *et al.* [22] suggested that the increase in growth rate with larger bias voltage probably corresponds to an increase in incident ion flow, rather than the production of neutrals close to the substrate. However, the contribution of other radicals than SiH_3 seems to be limited in ETP-CVD, and this for two reasons. First of all, the silane molecules are dominantly dissociated by atomic hydrogen, which leads to SiH_3 production. Other radicals, such as SiH_x, with $x \leq 2$, are produced at a lower rate and their density in the plasma is lower [23]. Moreover, they can be lost in the gas phase by reaction with SiH_4, in contrast to SiH_3. Secondly, it was shown that negatively charged dust particles are confined in the plasma, thus their contribution to a-Si:H deposition is limited to a few percent or lower [23]. The dust particles present in the reactor usually deposit on the colder chamber walls, or are pumped away. Furthermore, we believe that most of the positive ions do not participate to the growth as they do not contain Si atoms (H^+, H_2^+, H_3^+). Concerning the cluster ions, such as $Si_nH_m^+$ ($n \geq 6$), generated by ion-silane chain reaction, Kessels *et al.* estimate their contribution to a-Si:H film growth from 4% to 9% [8]. This calculated contribution is considered as a maximum as no data on the sticking probability of the cationic clusters was available and thus it was taken as unity, following literature [24]. Moreover, we think that these large cationic silicon ions may be broken by collision with hot electrons in the plasma or on impact with the surface when an rf bias is applied.

Influence of ion bombardment on surface processes:

When an ion impinges on the growing surface, it can scatter back, be adsorbed on the surface or penetrate in the bulk of the material, depending on its potential and

kinetic energy. In any case, energy transfer to the surface takes place and the surface heats up locally. Therefore, ETP-CVD with external rf bias on the substrate seems to enhance surface processes, such as diffusion of radicals on the surface and hydrogen abstraction. Surface silicon atom displacement is also expected as a reduction in void incorporation is observed [20]. These processes are possible thanks to the energy transfer from the colliding particles to the radicals on the growing surface. Smets *et al.* observed a decrease in roughness with rf power [20] and this change in topography is a good indication of the increase in mobility of the precursors. The surface valleys are more efficiently filled. Moreover, the lower defect density, N_d, obtained with rf-biased ETP compared to solely ETP-CVD, suggests that hydrogen abstraction from the surface and sub-surface, from two neighboring hydrogen atoms, is facilitated, leading to lower polyhydride content (c_{HSM}, see Fig. 5.11). Hydrogen abstraction does not occur spontaneously at temperatures below 300°C [25] and thermal energy is insufficient to activate this process at low temperatures. The creation of growth sites (dangling bonds) and the desorption of precursor byproducts are most likely enhanced when an rf bias is applied. A lower defect density is also attributed to the prevention of strained or weak-bond incorporation thanks to ion bombardment.

Optimum ion energy:

High-energy ions can be detrimental to the deposited film as then bulk Si atom displacements or even sputtering may occur. Sasaki *et al.* suggested [26] that impinging ions break bonds and reconstruct the a-Si:H network, as the strength of Si-Si and Si-H bonds (respectively 2.4 eV and 3.4 eV) is much lower than the incoming ion energy. According to Hamers *et al.* [27], the optimum ion energy is defined by the energy per deposited Si atom, E_{perSi}, which should be between 5 eV and 15 eV. They observed an improvement in structural properties for material deposited in that range, promoting the formation of dense films. Unfortunately, this observation could not be confirmed by our results, as the error margin on the actual input power measurement is quite large in our case. However, we think that not only the total energy brought to the surface is important, but also the energy carried by each ion. The ions have indeed a local effect on the impact site and a small amount of high-energy ions might not have similar effects to that of a large amount of low-energy ions. In accordance with Smets *et al.* [20], the effects of ion bombardment can be distinguished into three phases depending on the energy of the impinging ions: (1) enhancement of radical surface diffusion at low-energy ion, similar to temperature effects; (2) bulk effect, such as atom displacement in the network for ions of medium-energy and (3) sputtering of atoms from the surface and sub-surface of the film for ions of high energy. In our case, a moderate ion energy of 20 eV, which correspond to phase (1) of the general phase diagram proposed by Smets *et al.* [20], is sufficient to improve the quality of the deposited layer.

Ion energy distribution function:

Another important aspect of ion bombardment is the ion energy distribution function (IEDF) of the ions arriving on the substrate. For collision-free rf-modulated sheaths, the ion IEDF has typically a saddle-shaped structure, as shown by Ero *et al.* [19], Coburn *et al.* [28] and later by Edelberg *et al.* [29]. Tsui *et al.* observed an IEDF that is non-symmetrical in amplitude about the mean ion energy eV_{dc} [30]. Thus in an Ar plasma with rf bias applied to the substrate, the IEDF is not a Gaussian around the average energy eV_{dc}, but a bimodal distribution. It is characterized by one peak at low energy and another at high energy. This characteristic is expected when the period of the rf signal ($2\pi/\omega$) is much longer than the transit time τ for an ion to traverse the sheath [28]. This is the reason why the average ion energy may not be representative of the actual energy of the ions bombarding the surface. In deposition conditions where the mean ion energy for example is 40 eV, ions carrying much higher energies can actually be present and be responsible for effects not expected on the basis of the average energy, such as atom sputtering. Moreover, in an Ar-H_2-SiH_4 plasma, ions with different masses are expected to be present and this may result in an energy distribution with multiple peaks. However, the subplantation or penetration of Ar ions in the subsurface is not considered to be likely, as the Ar^+ density in the plasma is low. H-related ions on the contrary could more easily penetrate in the subsurface layers of the deposited film [31]. This penetration could lead to either the passivation of dangling bonds or the creation of compressive stress in the material and thus affect the bulk properties of the deposited material. Strain leads to a decrease of the band gap [4], which Potts *et al.* observed with increasing rf bias at high deposition rate (> 30 Å/s). For the conditions presented in this study, the IEDF at the substrate has not yet been measured. Wang *et al.* showed that the ion energy distribution function at the substrate can be controlled during plasma processing by applying a periodic waveform to the substrate consisting of a short spike, to collect the electrons accumulated on the surface, in combination with a longer slow voltage ramp [32]. This method results in a narrow ion energy distribution compared to the IEDF obtained with the sinusoidal waveform we employed so far.

Substrate temperature versus ion bombardment:

During a-Si:H deposition, the surface mobility is determined to a large extent by the substrate temperature. At high substrate temperatures the surface mobility is large, leading to the relaxation of the growing network into a low-energy configuration, while promoting the emission of loosely adherent polyhydride species and hydrogen. The role of rf power is less clear. Ion bombardment supplies extra energy to the impact site on the substrate and from that point of view the effect is localized. However, it can be compared to the effect of substrate temperature and Marton *et al.* defined four quality regions for Si^+ ion beam epitaxy in the ion kinetic energy-temperature space [33]. They

showed that at low substrate temperatures, the optimal energy window for the ions is narrower than at higher temperatures, because at high temperatures damage inflicted by the bombardment is annealed out and thus higher ion energies are needed to really damage the surface. For rf PE-CVD film production, Turban has suggested [34] that at relatively low substrate temperatures, ion bombardment may provide the required activation energy for hydrogen elimination. Smets *et al.* [20] proposed that low-energy ion bombardment can lead to silicon surface displacement by reducing the activation barrier to bring the surface species into a diffusional state. The consequence would be a reduction in nano-size void incorporation. In our case, the surface temperature can be lowered by 50°C and dense material is still obtained when a mild ion bombardment accompanies the deposition. However, rf bias cannot substitute temperature as it has other implications. High-energy ion bombardment leads to sputtering of species weakly bonded to the film surface or even of Si from the bulk. On one hand, this can lead to an improvement of film quality that cannot be achieved with increasing substrate temperature (see N_d in Fig. 5.11). In that way, we believe that the defect-rich layer, supposedly deposited in the initial stage of the ETP growth, is reduced or even suppressed when an external rf bias is applied on the substrate. On the other hand, sputtering can lead to an increase in void density and thus to a decrease in mass density of the grown material. This latter effect is undesirable. The structure of the growing film is modified by the ion bombardment. This explains the improvement in the structural and electric parameters, irrespectively of the rf bias applied (expect for very high V_{dc}). In summary, only a mild ion bombardment is equivalent to substrate temperature.

5.5 Conclusions

In order to increase the deposition rate of a-Si:H at a moderate substrate temperature (250°C), while maintaining device-quality material properties, an external rf bias may be applied on the substrate holder during ETP-CVD. The combination of the ETP technique with ion bombardment opens up new possibilities for deposition of a-Si:H p-i-n solar cells. The addition of rf bias on the substrate leads to an increase in growth rate and the refractive index, a measure of the density of the film, reaches a maximum for a dc self bias of 20 V. The fact that there is a maximum indicates a competition between two effects: surface mobility enhancement, dominant at low power, and atom sputtering from the film surface, dominant at high power. For solar cell application, the former effect is considered as beneficial, whereas the latter has deleterious consequences. The reduction of mid-gap absorption for a mild bias of 24 V, as well as the reduction of Urbach energy, indicates that fewer defects are incorporated into the material.

Ion bombardment has some effects in common with substrate temperature and the application of a mild bias permits to reduce the substrate temperature by about 50°C

whilst keeping the same material properties. However, ion bombardment changes the structure of the a-Si:H network as lower defect densities can be achieved this way. It is interesting to note, however, that the light conductivity is not improved with rf bias at temperatures above 300°C, indicating that the temperature effect is stronger than that of ion bombardment. We think that the light conductivity is limited by the electron mobility. However, good material can be grown at 250°C, which is very important for p-i-n solar cells.

Ion-surface interactions play an important role in film formation. Depending on the potential energy of the bombarding ions, we can expect the following processes to occur:

1. Enhancement of surface diffusion,
2. Displacement of surface atoms (that in the ETP-deposition case may result in the reduction of an initial defect-rich layer) and displacement of bulk atoms,
3. Bond breaking or sputtering,
4. Implantation of positive ions, such as Ar^+ or H^+ (not considered at low ion energy used in our case),
5. Breaking up of $Si_pH_q^+$ clusters in the vicinity of the growing surface.

A mild ion bombardment of 20-25 V improves the film density, the bonding configuration of hydrogen to silicon atoms and reduces the incorporation of defects when a substrate temperature of 250°C is used. These effects are even more pronounced for ETP samples deposited without H_2 injected in the nozzle, which confirms the beneficial effect of H_{2Noz} in general on the a-Si:H properties. At higher bias voltages (> 40 V), the microstructure parameter, *R**, increases again, indicating an increase in void incorporation. The next step would be to study the ion energy distribution function and to control it in order to tailor the ion energy that leads to the growth of a-Si:H with optimized structural, optical and electric properties.

References

[1] W.M.M. Kessels, M.C.M. van de Sanden and D.C. Schram, J. Vac. Sci. Technol. A **18** (2000) 5

[2] S. Guha, X. Xu, J. Yang and A. Banerjee, Appl. Phys. Lett. **66** (1995) 595

[3] T. Takagi, J. Vac. Sci. Technol. A, **2** (1984) 382

[4] J.E. Potts, E.M. Peterson and J.A. McMillan, J. Appl. Phys. **52** (1981) 6665

[5] L. Martinu, J.E. Klemberg-Sapieha, O.M. Küttel, A. Raveh and M.R. Wertheimer, J. Vac. Sci. Technol. A **12** (1994) 1360

[6] A.H.M. Smets, W.M.M. Kessels and M.C.M. van de Sanden, Mat. Res. Soc. Symp. Proc. **808** (2004) 383

[7] J.P.M. Hoefnagels, Y. Barrell, W.M.M. Kessels and M.C.M. van de Sanden, J. Appl. Phys. **96** (2004) 4094

[8] W.M.M. Kessels, C.M. Leewis, M.C.M. van de Sanden and D.C. Schram, J. Appl. Phys. **86** (1999) 4029
[9] K. Kato, S. Iizuka, G. Ganguly, T. Ikeda, A. Matsuda and N. Sato, Jpn. J. Appl. Phys. **36** Part 1 (1997) 4547
[10] J.W. Rabalais, A.H. Al-Bayati, K.J. Boyd, D. Marton, J. Kulik, Z. Zhang and W.K. Chu, Phys. Rev. B **53** (1996) 10781
[11] R.E.I. Schropp and M. Zeman, *Amorphous and microcrystalline silicon solar cells*, Kluwer Academic Publishers, Dordrecht (1998) p. 44
[12] M. Isomura, T. Kinoshita and S. Tsuda, Appl. Phys. Lett. **68** (1996) 1201
[13] K. Akiyama, E. Tanaka, A. Takimoto and M. Watanabe, Jap. J. Appl. Phys. **27** (1988) 2192
[14] R.E.I. Schropp and M. Zeman, *Amorphous and microcrystalline silicon solar cells*, Kluwer Academic Publishers, Dordrecht (1998) p. 47
[15] G. Lavareda, C. Nunes de Carvalho, A. Amaral, J.P. Conde, M. Vieira and V. Chu, Vacuum **64** (2002) 245
[16] M. Brinza, Ph.D. thesis, Leuven University, 2004
[17] J.J. Loferski and P. Rappaport, Phys. Rev. **111** (1958) 432
[18] N. Laegreid and G.K. Wehner, J. Appl. Phys. **32** (1961) 365
[19] J. Ero, Nucl. Instrum. **3** (1958) 303
[20] A.H.M. Smets, J.P.M. Hoefnagels, W.M.M. Kessels and M.C.M. van de Sanden, to be published
[21] W.M.M. Kessels, M.G.H. Boogaarts, J.P.M. Hoefnagels, D.C. Schram and M.C.M. van de Sanden, J. Vac. Sci. Technol. A **19** (2001) 1027
[22] K. Ando, M. Aozasa and R.G. Pyon, Appl. Phys. Lett. **44** (1984) 413
[23] M. Isomura, T. Kinoshita and S. Tsuda, Appl. Phys. Lett. **68** (1996) 1201
[24] J.M. Jasinski, J. Vac. Sci. Technol. A **13** (1995) 1935
[25] A. Matsuda, K. Nomoto, Y. Takeuchi, A. Suzuki, A. Yuuki and J. Perrin, Surf. Sc. **227** (1990) 50
[26] T. Sasaki and Y. Ichikawa, J. Non-Cryst. Sol. **198** (1996) 1007
[27] E.A.G. Hamers, W.G.J.H.M. van Sark, J. Bezemer, H. Meiling and W.F. van der Weg, J. Non-Cryst. Sol. **226** (1998) 205
[28] J.W. Coburn and E. Kay, J. Appl. Phys. **43** (1972) 4965
[29] E.A. Edelberg, A. Perry, N. Benjamin and E.S. Aydil, J. Vac. Sci. Technol. A **17** (1999) 506
[30] R.T.C. Tsui, Phys. Rev. **168** (1968) 107
[31] S. Veprek, F.A. Sarrott, S. Rambert and E. Taglauer, J. Vac. Sci. Tech. **4** (1989) 2614
[32] S.B. Wang and A.E. Wendt, J. Appl. Phys. **88** (2000) 643
[33] D. Marton, K.J. Boyd and J.W. Rabalais, J. Vac. Sci. Technol. A **16** (1998) 1321
[34] G. Turban, Pure Appl. Chem. **56** (1984) 215

Chapter 6

Microcrystalline p-type doped layer as window layer of solar cells

6.1 Introduction

Microcrystalline p-type silicon (p-μc-Si:H) thin films have received much attention due to their potential application as window layers of amorphous silicon based solar cells [1] and tunnel-junction layers of tandem or multi-junction solar cells [2-4]. Solar cells fabricated with a p-μc-Si:H layer are expected to yield higher performances compared to solar cells with an amorphous SiC:H layer, because p-μc-Si:H layers show a larger doping efficiency, thus a higher conductivity, and good optical properties, namely smaller optical absorption.

In addition to these properties, we are interested in p-μc-Si:H layer for their thermal resistance, as it was shown that high growth rate expanding thermal plasma (ETP) a-Si:H material has a lower sub bandgap defect density and a higher mass density when it is deposited at high temperature (≥ 2 nm/s and 400°C). This high temperature treatment can be a problem for the underlying p-doped layer, so a thermal resistant p-layer is needed.

In this chapter, we give in section 6.2 a brief description of the experimental details, as well as the method used to determine the crystalline fraction of a microcrystalline silicon layer. In section 6.3, we present the optimization of the p-μc-Si:H layer and the influence of film thickness on crystallinity. Then p-μc-Si:H layers are annealed at various temperatures and the behavior of the properties following high-temperature

exposure is shown. Finally, in Section 6.4, we demonstrate the performance of this material in solar cells: first within a cell deposited with standard rf PE-CVD at low growth rate and low substrate temperature and then the preliminary results within cells deposited with the ETP technique at growth rate above 3 nm/s and at 400°C.

6.2 Experimental details

We deposited p-μc-Si:H thin films by radio-frequency plasma-enhanced chemical vapour deposition (rf PE-CVD) in the rf-chamber of the Cascade set-up, on Corning glass type 1737 for determination of the opto-electronic properties of the layers and for Raman spectroscopy and on [100] oriented low-resistance n-type c-Si for Fourier transform infra-red (FTIR) spectroscopy. The rf power was set at 40 W and the substrate temperature was fixed at 200°C. The electrode distance was 25.5 mm and the pressure in the reactor 0.15 mbar. Unless indicated otherwise, the gas flows were as follows: $H_2/SiH_4/B_2H_6$ = 100/1/0.2 sccm.

The Raman spectra were measured using a Raman microscope (Renishaw Ramascope system 2000), with a grating of 1800 lines/mm, in a backscattering geometry, with a 2 mW Ar laser at a wavelength of 514.5 nm focused on a spot of about 1 μm.

We determined the crystalline mass fraction, x_{cryst}, from the Raman spectra using the method developed by Smit *et al.* [5]. In Raman spectroscopy, incoming photons interact with the lattice, thus generating phonons (vibration of the lattice). The energy difference between the incoming and scattered photons is known as the Raman shift. For mono-crystalline silicon, a sharp peak is found at 520 cm^{-1} and for a-Si:H, a broad peak is centered at 480 cm^{-1}. This broad peak is mainly due to the transverse optical (TO) phonon mode. For microcrystalline silicon, the Raman spectrum consists of a combination of amorphous and crystalline contributions. In order to determine the crystalline contribution, we subtract an amorphous silicon Raman spectrum from the Raman spectrum of microcrystalline silicon. Here, we assume that the amorphous silicon Raman signal is not very sensitive to deposition conditions, which has been shown to be a valid assumption [5]. To obtain a flat background of the signal and a scaling factor, f, which takes into account the thickness of the sample and the alignment of the equipment, a least mean square routine is carried out in the spectrum regions where no peaks are expected for crystalline silicon. x_{cryst} is then calculated from the crystalline and amorphous peak areas, A_{cryst} and A_{am}, respectively, as described in equation (1). A_{am} corresponds to the amorphous TO peak obtained from Gaussian fitting of a typical amorphous spectrum, multiplied by the scaling factor f. A_{cryst} is the integration of the microcrystalline contribution spectrum between 440 and 560 cm^{-1}. Finally the ratio of the two peak areas is corrected for the difference in cross sections

for phonon excitation of crystalline silicon compared to that of a-Si:H and is taken at 0.8, as reported in literature [6,7].

$$x_{cryst}^{m} = \frac{A_{cryst}}{A_{cryst} + 0.8 * A_{am}} \quad (1)$$

Solar cells were prepared on Asahi TCO. The intrinsic layer has a thickness of 450 nm and the n-layer 20 nm. The back contacts consist of a succession of evaporated silver (100 nm) and aluminium (200 nm). The characterization of the cells is carried out using an Oriel solar simulator (Model 81150), under AM 1.5 global conditions (100 mW.cm^{-2} and 25°C).

6.3 p-doped microcrystalline silicon thin films

6.3.1 Crystallinity as function of layer thickness

In a first deposition series, we varied the B_2H_6 flow in order to get microcrystalline p-doped layers. We found an activation energy of the dark conductivity below 0.1 eV when using 0.2 sccm B_2H_6, diluted in 100 sccm H_2 and 1 sccm SiH_4, which indicates that the films are microcrystalline. The second experiment was carried out in order to estimate the amorphous incubation phase thickness for microcrystalline growth. It is known that the presence of boron hinders crystalline growth and that it is difficult to grow thin microcrystalline p-doped films [8]. First an amorphous layer is grown and only after few nanometers crystals start to form. This incubation layer depends on the substrate used, for instance using a crystalline substrate, the reactive species follow the underlying lattice and a thin incubation layer is obtained. For samples grown on glass, the incubation phase is usually thicker, but it can be reduced by tuning the gas dilution and pressure in the reactor chamber (low pressure), as well as the electrode distance (large electrode distance to get stable plasma). On thin transparent conductive oxide (TCO) layers, such as SnO_2:F used as front contact in p-i-n solar cells, p-μc-Si:H films as thin as 20 nm could be grown with a significant crystalline fraction [4]. The morphology and crystallinity of p-μc-Si:H depends on the thickness of the layer [9,10].

Raman spectroscopy was carried out on the second series to determine the crystalline mass fraction, x_{cryst} (Fig. 6.1). From this figure it is clear that the thin films contain a microcrystalline phase. However, we can notice that for a thickness lower than 10 nm, x_{cryst} drops from 55% down to 15%. We deduce from these data that the amorphous incubation layer is thinner than 10 nm. Note that there is a good correlation between the dark conductivity, σ_D, and the crystal fraction, x_{cryst}, as function of the layer thickness, as can be seen in figure 6.1. In the crystalline region, we may assume that most boron atoms are four-fold coordinated, which means that these boron atoms are active dopants. In the amorphous region, however, a large

fraction of these atoms are three-fold coordinated. As a consequence, the dark conductivity is enhanced when the crystal fraction is increased.

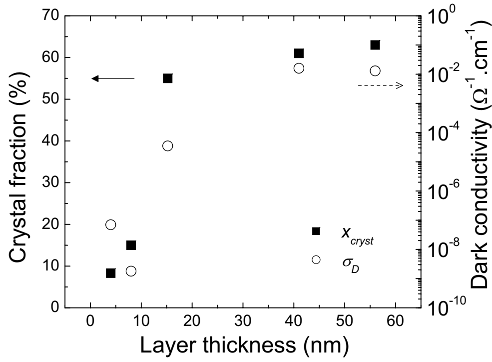

Figure 6.1: Crystalline fraction x_{cryst} from Raman spectroscopy and dark conductivity σ_D of p-μc-Si:H films versus sample thickness.

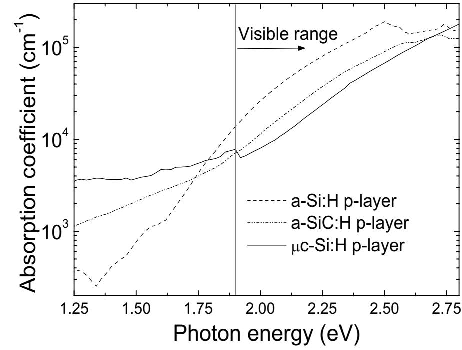

Figure 6.2: Absorption coefficient of amorphous Si, amorphous SiC and microcrystalline Si p-type materials.

The crystalline region of the p-μc-Si:H film has a mobility gap of 1.1 eV, but at the same time, crystalline silicon has an indirect band gap, which means that the absorption in the crystalline region is less efficient than in the amorphous region. The Tauc optical band gap is above 2.0 eV. The absorption profile of the p-μc-Si:H thin film as function of photon energy is compared to that of an amorphous sample in figure 6.2. The light absorption of the p-μc-Si:H layer is lower at high photon energy (in the visible range of the solar spectrum), although it is higher in the infra-red part of the spectrum. However, the solar spectrum has a low intensity at these low energies. We can expect that a cell with a p-μc-Si:H window layer will have a higher current density. For comparison, we show the absorption coefficient curve of an amorphous p-layer without carbon. It is obvious that this material has an increased absorption in the visible range compared to a-SiC:H.

6.3.2 Annealing of p-μc-Si:H thin films

In order to simulate the heating step that occurs before the deposition of a high-rate ETP deposition at high temperature and thus to assess the temperature resistance of the p-μc-Si:H layers, the samples were annealed at temperatures ranging from 250 to 400°C, for 0.5 h under 100 sccm He back flow to control substrate temperature. For this experiment, a thin film has been deposited on five pieces in one run and each piece was subsequently annealed at one given temperature, except for the 'as deposited' condition sample, which did not receive any annealing treatment.

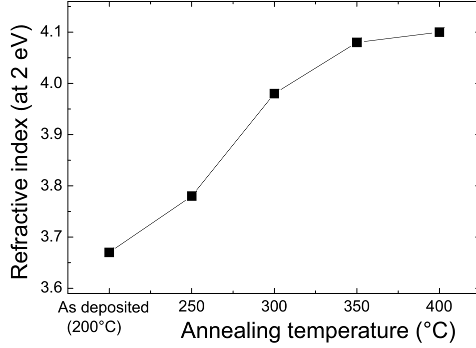

Figure 6.3: p-μc-Si:H films refractive index from RT versus annealing temperature.

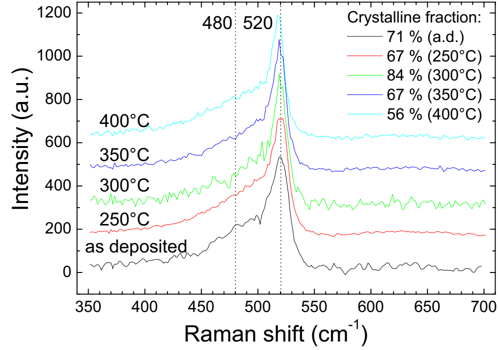

Figure 6.4: Raman spectra and x_{cryst} of the as-deposited and annealed p-μc-Si:H films.

After annealing, the refractive index of the p-μc-Si:H film has been measured. Compared to values prior to annealing, an increase of n_{2eV} was observed depending on the annealing temperature (Fig. 6.3). This increase indicates a densification of the material. The thermal energy supplied to the sample enhances a reorganization of the silicon network and we can expect that the doping is further activated. We speculate that the change in refractive index is mainly due to a densification of the amorphous part of the samples under the temperature treatment and we do not expect the crystalline mass fraction to vary. The variations in x_{cryst} with annealing temperature shown in figure 6.4 are due to the difficulty to fit the Raman spectra when the signal-to-noise ratio is low. The accuracy in x_{cryst} determination is then within 20%, like in the case of the sample annealed at 300°C.

With increasing annealing temperature, the dark conductivity increases (Fig. 6.5). This is due to a better activation of the doping as seen with the decrease of the activation energy, E_{act}, to values below 0.01 eV. The total hydrogen content, c_H, is quite low, below 3 at.%, as expected in microcrystalline material [11]. Hydrogen concentrates in the amorphous part and grain boundaries, where it passivates the dangling bonds and the crystalline part does not contain hydrogen. Within the measurement accuracy, c_H is independent of the annealing temperature, which means that hydrogen does not migrate out of the p-μc-Si:H layer during annealing.

In summary, we carried out thermal annealing treatments of p-μc-Si:H thin films at temperatures as high as 400°C to simulate the heating time before ETP i-layer deposition. After this step, the properties of the material have changed: the material densified thanks to the thermal energy supplied during annealing, the activation energy decreased considerably, indicating that the boron doping is further activated during the treatment and the dark conductivity increased by a factor of 10. The hydrogen content is independent of the temperature and the optical band gap remains around 2 eV.

Finally, these properties are still within the specifications for window layer in solar cells [12].

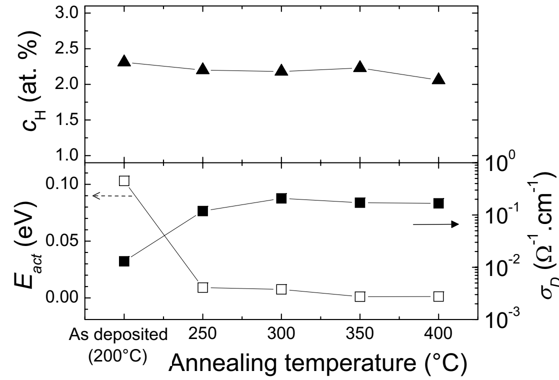

Figure 6.5: Activation energy, E_{act}, dark conductivity, σ_D, and total hydrogen content, c_H, of p-μc-Si:H layers before and after 0.5 h annealing at different temperatures.

6.4 Integration of the p-μc-Si:H layer in a solar cell

6.4.1 rf PE-CVD solar cells

In order to verify the influence of the p-μc-Si:H layer on solar-cell external parameters, two solar cells were deposited with rf PE-CVD in the Cascade set-up, with the intrinsic layer grown at 0.2 nm/s and 200°C. The first cell had a standard a-SiC:H p-doped window layer, while the second had a p-μc-Si:H layer as described in section 6.2. The a-SiC:H p-type layer had a thickness of 12 nm and the p-μc-Si:H layer had a thickness of 20 nm. A dummy deposition was carried out in the rf chamber between the p- and i-layer depositions to bury the B atoms, thereby avoiding contamination of the consecutive i-layer. The cell's external parameters can be found in table 6.1.

p-type layer	V_{oc} (V)	J_{sc} (mA/cm^2)	FF (-)	η (%)
Amorphous SiC	0.84	14.4	0.56	6.8
Microcrystalline Si	0.75	13.4	0.60	6.1

Table 6.1: External parameters of rf PE-CVD solar cells with either an a-SiC:H or a μc-Si:H p-layer.

The implementation of a p-μc-Si:H layer in the cell permits to increase the fill factor, *FF*, by 7%. This increase can be attributed to an increase of the internal electric field as the activation energy of p-μc-Si:H is much lower than that of a-SiC:H. However, although microcrystalline p-type silicon provides a good contact with the

transparent conductive oxide electrode [12] compared to an a-SiC:H p-layer, the open-circuit voltage, V_{oc}, decreases and the short-circuit current density, J_{sc}, is reduced compared to the amorphous case.

The ratio of the external quantum efficiency (QE) at 0 V bias to that at an applied negative bias (−1 V) is a measure for the carrier recombination in the cell at each wavelength [13]. This QE ratio is shown in figure 6.6. The 400-450 nm wavelength region is absorbed in the first nanometers of the i-layer. We can see that the cell with a p-μc-Si:H layer shows in that region a strong voltage-dependent charge collection behavior. This voltage-dependence behavior is not observed for a cell with an a-SiC:H p-layer. A reverse bias of −1 V is necessary to retrieve all the charge carriers generated at the micro-p-i interface. This seems to be a contradiction: although the p-μc-Si:H cell has more recombination at or near the p-i interface, yet this cell has a higher *FF*. However, this same cell performs better for longer wavelengths, which can explain the higher *FF*. Thanks to a higher internal electric field, less carriers are lost deeper in the cell with a p-μc-Si:H layer.

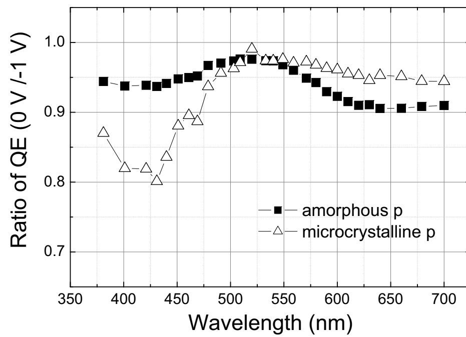

Figure 6.6: Spectra of external quantum efficiency ratios (0 V / −1 V reverse bias) for two cells with either an amorphous or a microcrystalline p-layer.

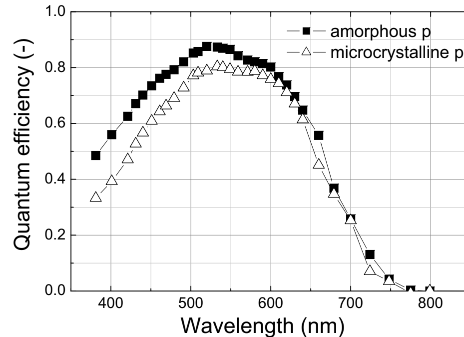

Figure 6.7: QE spectra of rf PECVD cells at −1 V external bias voltage with either an amorphous or a microcrystalline p-layer. The 450 nm thick i-layer is deposited at 200°C and 0.2 nm/s.

The spectral response of these two cells at −1 V indicates that less light enters the i-layer of the cell with a microcrystalline p-layer, compared to a totally amorphous cell (Fig. 6.7). Therefore some light is absorbed either in the p-μc-Si:H or in the TCO.

As a consequence, the overall efficiency of the cell is more or less the same when a p-μc-Si:H is implemented. This p-layer has shown good properties to high-temperatures exposure, which means that this structure can be used for cells with intrinsic layers deposited at high growth rate and high temperature.

6.4.2 Influence of p-μc-Si:H thickness in solar cells

The thickness of the p-type layer plays an important role in the operation of a solar cell. The structure of a p-i-n solar cell is indeed such that an internal electric field is generated in the cell, allowing the charge carriers that are generated after absorption of the photons in the intrinsic layer, to be separated and collected at the electrodes. The light absorption in the p-layer should be minimized. So the p-layer should have a high band gap and it also needs to be as thin as possible. However, the p-layer thickness cannot be reduced too much, because band bending at the TCO-p interface will affect the internal electric field distribution. The difficulty of growing microcrystalline silicon from the beginning without an amorphous incubation phase is also limiting the thickness of the p-μc-Si:H layer to a minimum value. A compromise between the two conflicting requirements (low absorption and high conductivity) has to be made to obtain a maximal performance.

To study the influence of the p-layer thickness, three solar cells were deposited with a p-μc-Si:H of respectively 8, 18 and 56 nm thick. As the p-layer thickness is increased, the V_{oc} also increases, due to the improvement of the built-in potential difference over the i-layer (see figure 6.8). However, the J_{sc}, as well as the *FF*, decreases. The decrease in J_{sc} indicates a higher absorption in the p-doped layer, which is observed in the spectral response of the cells taken at −1 V reverse bias (Fig. 6.9). It can be seen that for a p-μc-Si:H thickness of 18 nm and more, the quantum efficiency drastically decreases in the blue and green parts of the spectrum, compared to that of the cell with the thinnest p-layer. On the other hand, more charge carriers are lost at 0 V bias relatively to QE at −1 V for a p-μc-Si:H layer of 8 nm thick.

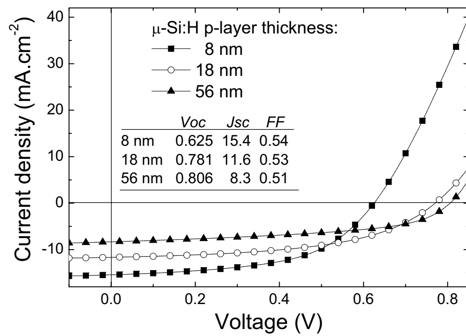

Figure 6.8: *J-V* curves of rf PE-CVD cells with different p-μc-Si:H layer thickness.

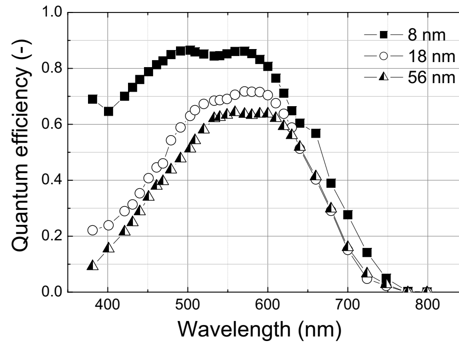

Figure 6.9: Spectral response of p-μc-Si:H thickness series solar cells under −1 V bias.

To conclude, to ensure high conductivity and high transparency, the microcrystalline p-layer is chosen to be 18 nm thick. We know indeed that for thin p-μc-Si:H layers, the crystalline fraction is much lower and thus also the conductivity

(crystalline fraction above 50% only for a thickness larger than 15 nm, see Fig. 6.1). We also observed that for a thicker p-layer, more light is absorbed in that layer and the cell performance decreases.

6.4.3 Integration of the p-μc-Si:H layer in an ETP solar cell

A relatively high substrate temperature of 350- 400°C is needed to obtain optimum properties of ETP a-Si:H grown at high rate (≥ 2 nm/s) [14]. At lower substrate temperature, a lower Si atomic density is obtained. This lower density is directly related to a relatively high hydrogen content, mainly bonded in the Si-H_2 configuration or clusters, and leads to a high microstructure value, R^*. An R^* value lower than 0.1 is usually reported for high-quality rf PE-CVD a-Si:H [15]. Increasing the substrate temperature permits to decrease the relative concentration of Si-H_2 bonds compared to the concentration of Si-H bonds, thereby reducing the R^* value. The light conductivity is also higher at these conditions, although still slightly lower than that reported for rf PE-CVD films [15].

In a solar cell deposited in a superstrate configuration, the p-type and i-layers are deposited consecutively. When the i-layer is grown at high temperature, like required for fast deposited ETP a-Si:H, the underlying p-layer has to sustain this high-temperature treatment and keep its properties. So far, the p-i-n solar cells deposited with these conditions have quite a low performance, mainly due to the extremely low current density. We think that the amorphous p-layer is damaged during deposition of the i-layer. Therefore we introduce a p-μc-Si:H, which showed good resistance to high-temperature exposure, instead of a standard a-SiC:H layer in the ETP solar cells.

Two solar cells were deposited with the intrinsic layer grown by means of the ETP technique at high growth rate (3.3 nm/s) and high temperature (400°C). The first cell had a standard a-SiC:H p-doped window layer, while the second had a p-μc-Si:H layer as described earlier. The thickness of the p-layer was 12 nm for the amorphous layer and 18 nm for the microcrystalline one. The *J-V* curves of these cells can be found in figure 6.10.

The implementation of a p-μc-Si:H layer in the cell gives rise to an increase of V_{oc} and of *FF* of about 10% (Fig. 6.10). Microcrystalline p-type silicon provides indeed a good contact with the transparent conductive oxide electrode, leading to higher V_{oc}. The series resistance, R_s, is decreased, which we ascribe to a better contact between the TCO and the p-layer. The increase in *FF* can be interpreted as an increase of the built-in potential, leading to a decrease of carrier recombination, as seen earlier in the rf PE-CVD cells. However, J_{sc} is lower than in the amorphous case. This decrease in current density is not thought to be due to extra absorption losses in the p-layer, as it was shown that the p-μc-Si:H absorbs less light than p-type a-SiC:H, but due to the reduction of the transparent conductive oxide after exposure to a H_2-rich plasma, needed for the deposition of p-μc-Si:H. During deposition of a-SiC:H, the TCO layer is indeed not exposed to H_2 plasma, but only to a SiH_4 plasma. Therefore, even if some

atomic hydrogen are produced, their density should be too small to affect the TCO significantly, in comparison with deposition of p-μc-Si:H. Moreover, deposition of a-SiC:H is 10 times faster than of p-μc-Si:H, so the TCO is quickly covered by a silicon layer, which can prevent further reduction of the SnO_2:F.

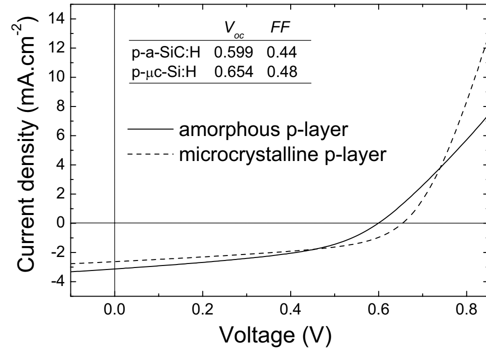

Figure 6.10: *J-V* characteristics of ETP cells, with either a-SiC:H p-layer or μc-Si:H. The 450 nm thick i-layer is deposited at 400°C and at a growth rate of 3.3 nm/s.

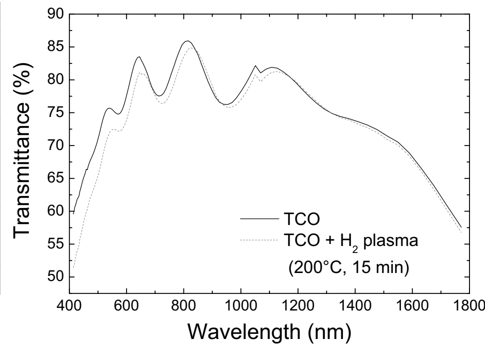

Figure 6.11: Transmittance spectra of TCO layers before and after H_2 plasma treatment of 15 min at 200°C, 40 W and 0.15 mbar.

In order to verify that assumption, we exposed a substrate glass + Asahi U-type TCO to identical H_2 plasma conditions as for p-μc-Si:H growth, except that no process gas was introduced in the rf chamber (H_2 = 100 sccm). The transmittance of the TCO layer is decreased after exposure to the H_2 plasma (Fig. 6.11), especially for wavelengths between 400 and 800 nm, which means that less light enters the i-layer. We observed also a blackening of the TCO. It is interesting to remark that Das *et al.* observed a much more severe reduction of TCO after exposure to H_2-plasma [16]. However, they carried out the experiments at higher pressure (0.67 mbar); we used a reactor pressure of only 0.15 mbar, which means that the residence time of the atomic hydrogen is much lower in our case, so the damage caused by the atomic hydrogen is expected to be of lower magnitude. Schade *et al.* found that the exposure of SnO_2:F to a H_2 plasma leads to chemical reduction to SnO and metallic Sn at a temperature as low as 150°C [17,18]. The oxygen depleted surface layer acts then as a source for Sn diffusion into subsequently deposited layers. This reduction of TCO leads to a decrease in light transmission, but can also lead to an increase in sheet resistance [19]. The darkening of the TCO can be avoided by protecting the layer with a ZnO layer [20], but we did not have the possibility to get ZnO coating at the time we carried out these experiments.

In addition to the darkening of the TCO, some elements, such as B or H, may diffuse out of the p-layer during deposition of the intrinsic layer at 400°C. Effusion of hydrogen out of the p-layer is not considered as we observed that the hydrogen

content of p-μc-Si:H remained unchanged following a heat treatment up to 400°C (Fig. 6.5). However, we do not know if some diffusion processes can take place when a layer is deposited on the p-μc-Si:H compared to a high-temperature exposure in vacuum. Boron diffusion out of the a-Si:H p-layer into the i-layer was already observed when the latter is deposited at 250°C [21,22]. However, this is not the case with a p-μc-Si:H layer as shown by Rath *et al.* [4], although they used a buffer layer as electron back-diffusion barrier. This buffer layer was necessary to compensate for the valence band offset between the p-μc-Si:H and the intrinsic a-Si:H layers and to reduce the recombination in the p-layer. The diffusion coefficient of boron in crystalline silicon is estimated to be about 10 orders of magnitude lower than that in an amorphous silicon [23], so we can estimate that the boron diffusion coefficient is lower in microcrystalline silicon than in a-Si:H. However, the possibility that boron diffuses into the intrinsic a-Si:H cannot be ruled out. This boron diffusion might lead to the creation of a defective region at the p-i interface in our case. This effect of i-layer growth conditions on the p-i interface properties are expected to be much less crucial in n-i-p structures.

In overall, the same efficiency is achieved for solar cells deposited at high growth rate and high temperature with an a-SiC:H p-layer or with a p-μc-Si:H layer. These are preliminary results on the potential of microcrystalline p-layers in ETP cells and further investigations should be carried out, with for instance a protective ZnO layer on the SnO_2:F and a buffer layer at the p-i interface, to exploit all the potential of this cell structure.

6.5 Conclusions

Microcrystalline silicon p-doped (p-μc-Si:H) thin films were developed in the rf-chamber of the CASCADE set-up for their high conductivity and low absorption, making them a suitable candidate as window layer in high-rate ETP solar cells. A low activation energy (< 0.1 eV) and a crystalline fraction above 50% were obtained. Annealing these layers for 0.5 h at 400°C enhances the doping efficiency. In the visible range of the solar spectrum, p-μc-Si:H layers absorb less light than p-type a-SiC:H.

Solar cells prepared with conventional rf PE-CVD i-layer (low growth rate and deposition temperature) show equivalent performance when a p-μc-Si:H window layer is used as when an a-SiC:H p-layer is incorporated in the cell; although a lower current density is obtained, the fill factor increases.

We incorporated this p-μc-Si:H layer in a solar cell with the intrinsic layer deposited with the ETP technique at 3.3 nm/s and 400°C. Compared to a solar cell with conventional p-type a-SiC:H layer, the V_{oc} and FF increase, but the J_{sc} decreases. It is shown that SnO_2:F is reduced during the p-μc-Si:H layer deposition by exposure to H_2 plasma, which overcomes the beneficial effect of low absorption of the microcrystalline layer. Metallic Sn from the oxygen depleted region at the TCO-p

interface can diffuse in the p-layer. Moreover, during the deposition of the high-rate ETP i-layer, boron can diffuse in the i-layer, deteriorating the p-i interface. No improvement in the performance of the solar cell is observed with a microcrystalline Si layer compared to an amorphous one. Here we have to point out that this does not mean that p-μc-Si:H does not resist to a high temperature treatment, but that other processes, such as TCO reduction, overcome the beneficial effect of the incorporation of p-μc-Si:H in an ETP cell. It is suggested that a thin ZnO layer should be applied onto the SnO_2:F to prevent the reduction of the TCO. It is also advised to use a buffer layer at the p-i interface to avoid electron-back diffusion and boron diffusion into the i-layer.

References

[1] S. Guha, J. Yang, P.Nath, M. Hack, Appl. Phys. Lett. **49** (1986) 218

[2] T. Yoshida, K. Maruyama, O. Nabeta, Y. Ichikawa, H. Sakai and Y. Uchida, Proc. IEEE Photovoltaic Specialists Conference, New Orleans (1987) 1095

[3] M. Trijssenaar, G.E.N. Landweer, L.L.A. Vosteen, J.W. Metselaar, Proc. of the 11th E.C. Photovoltaic Solar Energy Conference, Montreux (1992) 564

[4] J.K. Rath, R.E.I. Schropp, Sol. Energy Mat. Sol. Cells, **53** (1998) 189

[5] C. Smit, R.A.C.M.M. van Swaaij, H. Donker, A.M.H.N. Petit, W.M.M. Kessels and M.C.M. van de Sanden, J. Appl. Phys. **94** (2003) 3582

[6] R. Tsu, J. Gonzalez-Hernandez, S.S. Chao, S.C. Lee and K. Tanaka, Appl. Phys Lett. **40** (1982) 534

[7] A.T. Voutsas, M.K. Hatalis, J. Boyce and A. Chiang, J. Appl. Phys. **78** (1995) 6999

[8] K. Prasad, U. Kroll, F. Finger, A. Shah, J.-L. Dorier, A. Howling, J. Baumann and M. Schubert, Mater. Res. Soc. Proc. **219** (1991) 383

[9] R.W. Collins, B.Y. Yang, J. Vac. Sci. Technol. B **7** (1989) 1155

[10] M. Fang, B. Drévillon, J. Appl. Phys. **70** (1991) 4894

[11] D. Das, M. Jana, Sol. Energy Mat. & Sol. Cells **81** (2004) 169

[12] R.E.I. Schropp and M. Zeman, *Amorphous and microcrystalline silicon solar cells*, Kluwer Academic Publishers, Dordrecht (1998) pp 59-60

[13] R.R. Arya, A. Catalano, R.S. Oswald, Appl. Phys. Lett. **49** (1986) 1089

[14] B.A. Korevaar, G.J. Adriaenssens, A.H.M. Smets, W.M.M. Kessels, H.Z. Song, M.C.M. van de Sanden and D.C. Schram, J. Non-Cryst. Sol. **266-269** (2000) 380

[15] W. Luft and Y.S. Tsuo, *Hydrogenated amorphous silicon alloy deposition processes*, Marcel Dekker, New York (1993)

[16] R. Das, T. Jana and S. Ray, Sol. Energy Mat. & Sol. Cells, in press (Sept. 2004)

[17] H. Schade, Z.E. Smith, J.H. Thomas III, A. Catalano, Thin Solid Films **117** (1984) 149

[18] Y.H. Yang, G.F. Feng, M. Katiyar, N. Maley and J.R. Abelson, J. Vac. Sci. Technol. A **11** (1993) 1414
[19] S. Major, S. Kumar, M. Bhatnagar, K.L. Chopra, Appl. Phys. Lett. **49** (1986) 394
[20] A. Masuda, K. Imamori, H. Matsumura, Thin Solid Films **411** (2002) 166
[21] H. Matsumura, K. Sakai, M. Maeda, S. Furukawa, K. Horiuchi, J. Appl. Phys. **54** (1983) 3106
[22] D. Caputo, G. de Cesare, A. Nascetti, F. Palma, Thin Sol. Films **348** (1999) 79
[23] Y. Nasuno, M. Kondo, A. Matsuda, H. Fukuhori, Y. Kanemitsu, Appl. Phys. Lett. **81** (2002) 3155

Chapter 7

ETP solar cells deposited at high growth rates

7.1 Introduction

Over the past two decades much effort has been concentrated on increasing the deposition rate of hydrogenated amorphous silicon (a-Si:H) for p-i-n thin film solar cells from 2 Å/s up to 10 Å/s and more. Several techniques have been developed to reach this goal. In 1988, Bhat *et al.* manufactured a-Si:H with radio-frequency plasma enhanced chemical vapor deposition (rf PE-CVD) at ~ 10 and ~ 20 Å/s, giving p-i-n solar cell efficiencies of respectively 9 and 8% [1]. However, the cost related to disilane, the gas utilized as precursor in that case, reduced the potential for industrial production. In 1998, hot-wire (HW) CVD proved to be a suitable technique to grow intrinsic material up to 8.5 Å/s, leading to 8% cell efficiency [2]. Recently Franken *et al.* obtained efficiencies of HW-CVD a-Si:H solar cells ranging from 7.5% to 8.5% at growth rates from 32 Å/s to 16 Å/s, using a 5-nm thick ZnO:Al protection layer on Asahi TCO [3]. High efficiencies at high growth rates were obtained also for very high frequency (VHF) CVD, with which single-junction a-Si:H solar cells were grown on large area with an initial efficiency of 7.1% at a deposition rate of 6 to 7 Å/s [4] and recently 8% efficiency for a deposition rate of 10 Å/s [5]. We note that in most of these solar cells a highly reflective back contact is employed.

With the expanding thermal plasma (ETP) CVD technique, high growth rates (up to 100 Å/s, [6]) have also been achieved for a-Si:H deposition. ETP-CVD is a relatively

new technique with great potential and few problems are foreseen in the up-scaling of the method, as it is already used industrially for silicon nitride deposition [7]. As for most techniques, when using ETP-CVD, high temperatures (> 300°C) are required in order to obtain material with sufficiently low defect density for solar cell application at rates in excess of 10 Å/s. For the production of p-i-n a-Si:H solar cells, these high temperatures can lead to the deterioration of the underlying p-layer, thereby reducing the solar-cell performance. In addition, there are indications that during the initial growth stage of high-rate ETP a-Si:H, the defect density is relatively high, resulting in a defect-rich layer (DRL) in the first nanometers of the thin film.

Two routes are considered to overcome these difficulties. The first one consists in growing a dense buffer layer between the p- and the ETP i-layer to protect the TCO/ p-layer. This technique is commonly used in the solar cell fabrication. The second route consists in reducing the substrate temperature for i-layer deposition, while maintaining the electro-optical properties of this layer. This can be achieved by employing an external rf bias on the substrate, as an additional ion bombardment can be induced and under these conditions device-quality material can be obtained at moderate temperatures of 200-250°C.

In this chapter, we will explain the two routes in more detail and the results obtained so far. In the first section, after discussing the DRL assumption, we will present the results of simulations, carried out with the ASA modeling program, describing the dependence of the position and the thickness of the DRL on solar cell's performance. The choice of the buffer layer and of its thickness are then studied in superstrate solar cells of which the intrinsic layer is grown using ETP-CVD. In the second section, we will focus on the performance of single junction solar cells prepared with the ETP-layer grown with an external rf bias on the substrate. The analysis deals with the input power applied, in other words with the ion bombardment inflicted to the growing surface, but also on the influence of an annealing treatment on the cell's performance.

7.2 Buffer layer

It is well known that p-i interface properties largely dominate solar cell performance because most photocarriers are generated in this p-i interface region. In the p-i-n deposition sequence, where the intrinsic layer is directly grown on the p-layer, the effects of the i-layer growth conditions on the p-i interface properties are therefore expected to be crucial, because during the initial stages of the growth of the intrinsic layer the defect density can be high. We will refer to this region as the defect-rich layer (DRL). In order to improve the p-i interface properties a dense buffer layer with a low defect density is deposited at low rate and low substrate temperature prior to the high

rate, high substrate temperature intrinsic layer. As we will show, the implementation of such a buffer layer enhances the performance of the solar cell.

7.2.1 Indications of a defect-rich layer (DRL)

The properties of ETP-CVD material were found to be comparable to those of a-Si:H deposited by rf PE-CVD [8]. However, single junction solar cells fabricated with an ETP intrinsic layer systematically have a lower fill factor, *FF*, whereas the short-circuit current density, J_{sc}, and the open-circuit voltage, V_{oc}, can be as good as those of cells with an rf PE-CVD i-layer. This lower performance is not attributed to a higher defect density, N_d, of the ETP a-Si:H bulk because DBP measurements on ETP a-Si:H layers show that N_d is lower than 10^{16} cm^{-3}, comparable to N_d of rf PE-CVD a-Si:H. In order to explain the lower ETP solar-cell performance, Korevaar suggested that during the first stages of the growth with the ETP technique more defects are incorporated in the material than later in the bulk [8]. He showed by computer simulation that the defect density near the p-i interface, where most charge carriers are generated, can influence the fill factor: a higher N_d in that region of the cell leads to more recombination in this region and subsequently to a lower *FF*. Korevaar related this ETP characteristic to a high roughness of the microscopic surface (~ 4 nm) [9] compared to that of rf PE-CVD material (~ 1 nm) [10]]. The work of Smets *et al.*, using cavity ring down spectroscopy measurements, indicates also the possibility of the creation of such a layer [11], as well as the work of Shimizu *et al.* who used electron spin resonance measurements [12]. Smets found that the DRL could have a defect density as high as 10^{18} to 10^{19} cm^{-3}.

In order to confirm or refute the assumption of a DRL, the opto-electric properties of an ETP a-Si:H reference layer were plotted as function of the film thickness. The light conductivity, σ_L, the optical band-gap, E_{Tauc}, and the refractive index, n_{2eV}, were investigated for layers of thickness ranging from 20 nm to 850 nm. The thinner the sample, the larger the effect of the surface region compared to the bulk, and thus the larger the effect of the supposed DRL. However, despite the wide range in the thickness of the investigated layers, no strong indication of a DRL was found. The values of the considered parameters vary within the measurement accuracy. Moreover, other characterization methods, such as dual-beam photoconductivity or Fourier transform infrared spectroscopy, which permit to assess directly the defect density of the layers, can be performed only on thick samples (> 400 nm) to give reliable results.

It appears that the assumption of the existence of a defect-rich layer as initial growth of the ETP a-Si:H cannot be confirmed or refuted with the characterization methods used so far. However, simulations carried out by Korevaar with the ASA modeling (Amorphous Semiconductor Analysis) showed that the differences in performance of an ETP and an rf PE-CVD cell can be explained by a larger defect density near the p-i interface for the ETP cell [8]. And recently, Aarts *et al.* [13] carried out real-time measurements by thin film cavity ring down spectroscopy to detect

defect-related absorptions associated with dangling bonds. They claim the existence of a defect-rich layer with a defect density of 10^{12} cm^{-2}.

7.2.2 Simulations of a DRL and buffer layer in a-Si:H solar cells

It has been demonstrated experimentally [14] that implementation of a buffer layer in between the p- and high-rate ETP i-layer improves the performance of the solar cells, in particular due to an enhancement of the open-circuit voltage, V_{oc}, and the fill factor, *FF*. We think that this buffer layer protects the p-layer from thermal damage by reducing the diffusion of hydrogen out of the p-layer. However, a performance improvement was observed also for solar cells with a low temperature (250°C), high-rate (0.9 nm/s) intrinsic layer in which a buffer layer was implemented [14]. We think that in this case implementing the buffer layer in the cell moves the thin defect-rich layer, presumably formed during the first stages of deposition, away from the critical p-i interface, reducing the recombination and improving the *FF*. The quality of the remainder of the intrinsic layer is good.

In this section we present simulations, carried out with the Advanced Semiconductor Analysis (ASA) program [15], that aim to investigate the position dependence of the DRL on the solar-cell performance. By increasing the thickness of the buffer layer, the DRL is shifted through the intrinsic layer. We also investigate the influence of the DRL thickness on the cell performance. These simulations may shed light on the properties of the material deposited during the initial stages of the growth with ETP-CVD. Other workers (e.g., see [16]) have simulated the effect of a buffer layer in the p-i region, with for example different band gap profiles, but in contrast to the work presented here, the aim was to optimize the cell performance.

The ASA program is an one dimensional (1-D) simulation program that calculates the internal electrical properties and external characteristics of multi-layer, heterojunctions a-Si:H solar cells by solving the system of semiconductor equations (Poisson's, continuity and transport equations) for the steady state. The main features of the ASA program include calculation of light generation profile, models describing a complete density of states distribution as function of energy and calculation of the defect-state distribution in a layer according to the defect-pool model [17]. The continuous change of all input parameters as a function of position in the device can be defined.

Solar cell structure

The structure of the cells simulated with the ASA program is presented in figure 7.1: a glass substrate covered with a transparent conductive oxide, an a-Si:H based p-, i- and n-layer and finally the Al back contact. The intrinsic layer is divided in three parts: the buffer layer with thickness varying between 0 and 390 nm, the initial grown DRL, which has a thickness of 30 nm, and finally the bulk of the ETP i-layer with a

thickness varying between 410 and 20 nm. The total thickness of the intrinsic layer is kept constant at 440 nm.

Input parameters

In table 7.1, the input parameters for the ASA program are listed. Table 7.1 includes the band gap, E_g, the electron and hole extended-state mobility, μ_e and μ_h, the density of states at the mobility conduction band edge, N_C^{mob} and at the mobility valence band edge, N_V^{mob}, and the characteristic energy E_{C0} and E_{V0} of the conduction and valence band tail, respectively. The effective densities of extended states for the conduction band, N_C, and for the valence band, N_V, were kept constant at 4×10^{26} m^{-3} and the electron affinity, χ_e, was taken to be 4 eV. We assume that the Urbach energy of the DRL is higher than in the bulk of the intrinsic layer in order to account for the higher defect density.

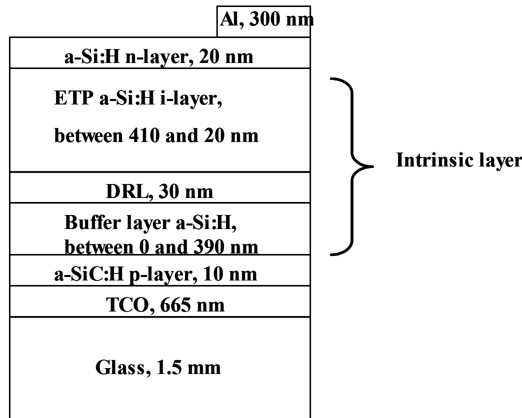

Figure 7.1: Schematic diagram of an a-Si:H solar cell as depicted in the ASA modeling.

The density-of-states distribution is calculated using the defect-pool model (DPM) from Powell and Deane [17]. The following DPM parameters have been used: the position of the peak of the defect pool, E_P, is taken at 1.25 eV, except for the p-layer in which case it is at 1.27 eV, the width of the defect pool, σ, can be found in table 7.4. The correlation energy between the transition energy levels representing the dangling bonds is E_{corr} = 0.2 eV.

Effect of a buffer layer

Two kinds of simulations were carried out. In the first series, the buffer-layer thickness was increased, moving the DRL away from the p-i interface. The DRL thickness was fixed at 30 nm.

Layers	E_g (eV)	μ_e / μ_h ($m^2V^{-1}s^{-1}$)	N_V^{mob} ($m^{-3}.eV^{-1}$)	N_C^{mob} ($m^{-3}.eV^{-1}$)	E_{V0} (meV)	E_{C0} (meV)	σ (eV)
p-type	1.97	1×10^{-3} / 1×10^{-4}	1×10^{28}	1×10^{28}	80	70	0.179
buffer	1.75	2×10^{-3} / 5×10^{-4}	5×10^{27}	7×10^{27}	50	32	0.160
DRL	1.75	1×10^{-3} / 1×10^{-4}	5×10^{27}	7×10^{27}	80	53	0.165
bulk ETP	1.75	2×10^{-3} / 5×10^{-4}	5×10^{27}	7×10^{27}	45	30	0.160
n-type	1.75	1×10^{-3} / 1×10^{-4}	7×10^{27}	7×10^{27}	90	80	0.175

Table 7.1: Parameters used in the ASA modeling.

The external parameters of the simulated solar cells can be found in table 7.2. When a buffer layer is incorporated in the cell, the V_{oc} first increases slightly, but then remains constant for a buffer-layer thickness in excess of 10 nm. The short-circuit current density, J_{sc}, decreases somewhat, though the *FF* increases significantly. The efficiency, η, also increases. The same trends have been observed experimentally on ETP solar cells [14].

Buffer layer (nm)	V_{oc} (V)	J_{sc} (mA/cm²)	*FF* (-)	η (%)
0	0.795	11.9	0.627	5.94
10	0.801	11.7	0.658	6.18
50	0.801	11.4	0.688	6.27
75	0.802	11.4	0.693	6.32

Table 7.2: External parameters of the simulated solar cells with varying buffer layer thickness.

The band diagram of the two simulated cells, one with and one without buffer layer, is shown in figure 7.2. We can see that near the p-i interface, in the region denoted as A, the bending of the conduction and valence bands is less strong for the cell without buffer layer compared to the one with a 50-nm thick buffer layer. This strong band bending implies that the internal electric field is stronger in that region when a buffer layer is applied (see figure 7.3) and therefore the charge carriers are swept out of this region faster than when there is no buffer layer. The recombination probability is then less and the *FF* increases. Moreover, when no buffer layer is incorporated in the cell, the defect density drastically increases at the p-i interface because of the DRL, thereby increasing the recombination which results in less charge carrier collection. Incorporation of a buffer layer moves the DRL away from the sensitive p-i area, thereby diminishing the recombination at the interface and improving the *FF*.

Deeper in the cell, in the region denoted as B, we can see that the band bending is stronger for the cell without a buffer layer, resulting in a stronger electric field. This means that for the cell without buffer layer more charge carriers are collected from deeper in the cell than for the cell with buffer layer at the expense of charge-carrier collection near the p-i interface. However, deeper in the cell fewer carriers are generated, but as these carriers experience a higher electric field, it is more likely that these carriers are collected, which implies that J_{sc} is higher for the cell without buffer layer.

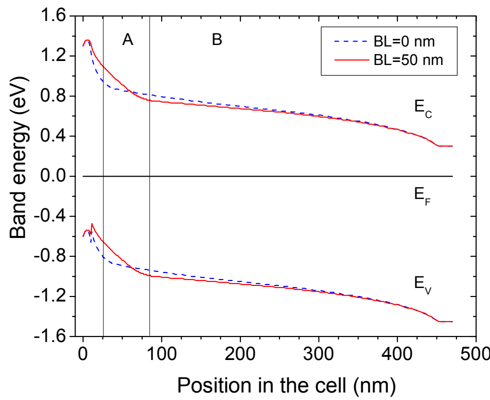

Figure 7.2: Band diagram of the simulated cells at thermal equilibrium with and without buffer layer. The DRL is 30 nm thick.

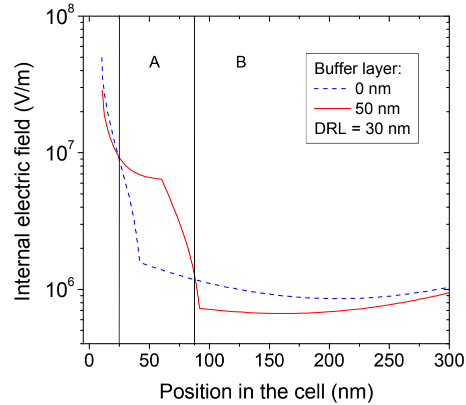

Figure 7.3: Internal electric field distribution for cells with and without buffer layer. The DRL is 30 nm thick.

There are several competing effects that determine the performance of a cell: the strength of the electric field and the defect density, the generation and recombination profiles. When the electric field is high, the carriers have more chance to be separated and collected, but if the defect density is also high, the carriers have more chance to recombine. The collection probability depends on where the DRL is situated and how thick it is. In our case, it seems that a buffer layer of 75 nm thick permits to increase the *FF*, but the J_{sc} is slightly decreased, so an even thicker buffer layer would not increase the performance anymore.

Effect of the defect-rich layer

In the second series of simulations, we studied the effect of the variation of the thickness of the DRL, grown during the initial stages of the deposition with ETP. It appears that the thicker this defective layer, the lower the solar cell performance in terms of V_{oc}, *FF* and J_{sc} (see figure 7.4). A 10-nm thick buffer layer is sufficient to improve the V_{oc}. For thicker buffer layers, the V_{oc} increases only slightly. The J_{sc} decreases to reach a minimum value for the 30-nm thick DRL. For the 5-nm and

15-nm thick DRL J_{sc} keeps on decreasing with the buffer layer thickness. The *FF* is largely affected by the DRL thickness and the same trend is observed for the three thicknesses. The *FF* becomes maximal for a buffer layer of about 75 nm. With a buffer layer at the p-i interface, the DRL is situated further in the cell, so more carriers recombine in the middle of the cell, where the defect density is highest, which means that fewer carriers are collected and the current density decreases. Moreover, the *FF* is first increased as a function of buffer layer thickness because more carriers are separated at the p-i interface. Above a certain buffer layer thickness (~75 nm), the DRL is too far from the p-i interface to have an influence on the recombination there but it starts to influence the i-n interface and the *FF* diminishes.

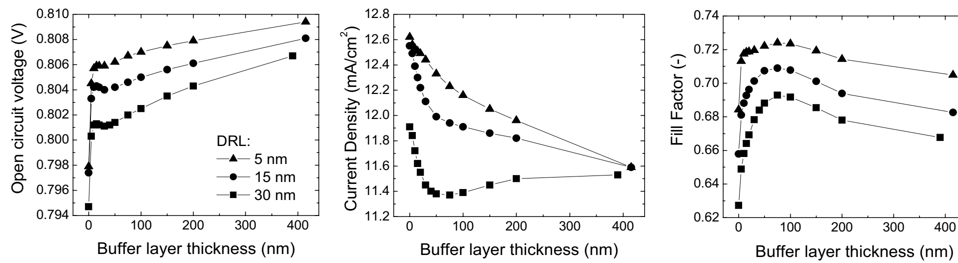

Figure 7.4: Simulations of the external parameters of a p-i-n cell as a function of the buffer layer thickness, this for three different thicknesses of DRL. The total thickness of the intrinsic layer is 440 nm.

If the DRL cannot be avoided, it is better to situate it within the first quarter of the intrinsic layer. The *FF* is indeed optimal around 75 nm buffer layer thickness, V_{oc} is more or less constant and J_{sc} is decreasing.

To understand the effect of the DRL thickness on the cell performance, we compare two cells that have a buffer layer of 10 nm; the thickness of the DRL is respectively 5 nm and 30 nm. The band diagram of these cells at thermal equilibrium is presented in figure 7.5. The DRL thickness has little influence on the band diagram in the buffer layer, but in the ETP layer we can see that for a thinner DRL the slope of the band is less steep. The DRL thickness does not influence the band diagram after 200 nm in the cell. Close to the p-i interface, the internal electric field is stronger for the cell with a thick DRL (see figure 7.6). This means that the carriers are swept away from this region faster than in the cell with a thin DRL. However, the J_{sc} and the *FF* are lower. We believe that this is due to the fact that more carriers are trapped or recombine in the DRL.

The presence of the DRL influences the current collection not only in this layer, but also in the rest of the cell. Deeper in the cell (before ~200 nm), the electric field is higher for cell with a thin DRL, which allows more carrier collection and thus a higher J_{sc}.

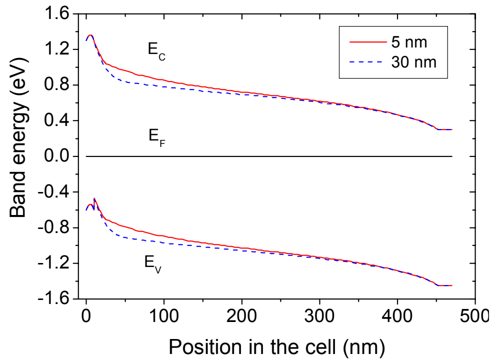

Figure 7.5: Band diagram of the simulated cells at thermal equilibrium with resp. a 5- and 30-nm thick DRL. The buffer layer is 10-nm thick.

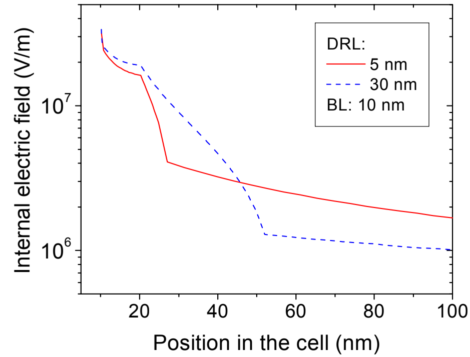

Figure 7.6: Internal electric field distribution for cells with resp. a 5- and 30-nm thick DRL. The buffer layer is 10-nm thick.

In conclusion, we have carried out two series of simulations. The first series shows that the incorporation of a buffer layer at the p-i interface increases the performance of the cell by augmenting the internal electric field at the interface and shifting the defect-rich layer further in the bulk of the cell away from the sensitive p-i interface.

The second set of simulations shows that a thicker DRL suppresses the performance of the cell. Further the simulations show that also at the i-n interface the DRL thickness has a strong influence on the *FF*, which is clearly lower for a thicker DRL. This means that a larger defective layer enhances the recombination at the i-n interface.

7.2.3 Choice of a buffer layer

The intermediate layer that will be used as a buffer layer between the p- and i-layers should have a low structural disorder and a low defect density. For that purpose, the buffer layer is grown by rf PE-CVD at low substrate temperature and low growth rate. A lower defect density at the interface results in less recombination in this region and thus we can expect a solar cell with a higher *FF*. Moreover, other research groups used buffer layers as a seed layer for better start of the high-rate i-layer or to protect the p-layer from thermal damage as the buffer layer is deposited at similar temperature as the p-layer, which is usually much lower than for the high-rate i-layer. Wang *et al.* [18] used a buffer layer to engineer the band gap, which means that the buffer layer serves to decrease the band gap smoothly from ~ 2 eV (p-layer) to ~ 1.75 eV (i-layer). When the band discontinuity between the a-SiC:H p-layer and the a-Si:H i-layer is large, the surface recombination at the p-i interface is also large and the recombination current

in the interface region is much larger than that in the bulk region of the i-layer. A buffer layer permits to reduce the recombination rate at the interface because the carrier density in that region is actually reduced. A buffer layer has also been used in order to prevent electron back diffusion to the p-layer, and thus increasing the open-circuit voltage [19]. Finally, a buffer layer can act as a barrier for the diffusion of hydrogen out of the p-layer to the less hydrogen concentrated region formed by the high-rate i-layer, and especially the DRL. Hundhausen *et al.* explained that the hydrogen outdiffusion during the deposition process increases if a material of lower density (such as the DRL) is grown on top of a dense material [20].

Two buffer layers were studied as potential buffer layer between the p- and the i-layers. The deposition conditions, as well as some optical properties, are presented in table 7.3. These layers are deposited with the rf PE-CVD technique in the rf chamber of the CASCADE set-up. First a standard a-Si:H layer was deposited. Although it has a low band gap of 1.75 eV, which is comparable to that of the ETP material, this layer is a good candidate as buffer because of its quite high refractive index at 2 eV, representative of a dense material. And secondly, an amorphous silicon layer deposited from an H_2-diluted plasma was studied. This layer is also considered as a good buffer layer candidate as it is known to be a more ordered material than standard a-Si:H (considering the short-range order). We also tried a silicon carbide layer, as this layer has the advantage of a very high band gap (~ 2 eV), so it can be used to prevent electron back diffusion to the p-layer. The same conditions as for the p-layer deposition were used, except that no diborane flow was introduced in the reactor chamber. It is reported in literature [21-23] that a higher V_{oc} can be obtained when using an a-SiC:H layer at the p-i interface. However this effect was not observed here and the origin of this behavior is still not clear.

	SiH_4 (sccm)	H_2 (sccm)	Temp. (°C)	Pv / Pwr (mbar/W)	Rd (Å/s)	n_{2eV}	E_{Tauc} (eV)
a-Si:H	40	--	250	0.58 / 2.2	1.46	4.41	1.75
Diluted a-Si:H	10	100	200	0.78 / 2.2	0.71	4.25	1.75

Table 7.3: Deposition settings and optical properties of potential buffer layers.

In order to assess the influence of the selected buffer layers on the cell performance, four solar cells were prepared. The cells have a structure of glass/TCO/ p-(BL)-i-n/Ag/Al. The p-layer is deposited at 250°C and the n-layer at 200°C. The deposition conditions of the buffer layers can be found in table 7.3. The ETP layer is deposited without H_2-injection in the nozzle and is grown at a rate of 18.9 Å/s and a substrate temperature of 400°C. The performance of the cells can be found in table 7.4.

Cell A, entirely made with rf PE-CVD at a substrate temperature of 250°C, has a relatively high efficiency of 7.4%, mainly due to a high V_{oc} of 0.82 V. Cell A shows the potential of this cell structure with the best i-layer that can be produced in the rf-

chamber of the CASCADE set-up so far (note that in this rf-chamber the doped layers are deposited as well). When the rf i-layer is replaced by an ETP layer (18.9 Å/s and 400°C, Cell B), the efficiency drops drastically to 2.3%. We observe that all parameters are reduced, which indicates that the p-i-n cell structure is not adapted to the deposition of high growth-rate, high substrate-temperature intrinsic layers. Cells C and D are then prepared with a buffer layer deposited on top of the p-layer. The thickness of the buffer layer is chosen to be 10 nm. We can see that an a-Si:H buffer layer permits to recover some fill factor (7.7% improvement) and V_{oc} (Cell C, table 7.4), leading to an improved efficiency. A hydrogen-diluted buffer layer leads to an increase in all parameters (cell D versus cell B) and in particular to a nearly 20% improvement of the *FF*.

Cell n°	Buffer layer	i-layer	i-Temp (°C)	V_{oc} (V)	J_{sc} (mA.cm^{-2})	*FF* (-)	η (%)
A	none	rf PE-CVD	250°C	0.820	16.9	0.546	7.40
B	none	ETP-CVD	400°C	0.561	12.6	0.326	2.30
C	a-SiH	ETP-CVD	400°C	0.626	13.4	0.351	2.95
D	diluted a-SiH	ETP-CVD	400°C	0.612	15.1	0.389	3.57

Table 7.4: Superstrate solar cells deposited with and without a buffer layer at the p-i interface. The total i-layer thickness is kept constant at 440 nm and the buffer layer is 10 nm thick. The average of the best 10 cells is presented for each condition.

We think that the cell, deposited at 400°C in the p-i-n configuration, has improved characteristics when an a-Si:H buffer layer is employed because of several factors. First of all, the p-layer is to some extent protected from the high deposition temperature by the presence of the dense buffer layer. We believe that hydrogen diffusion out of the p-layer is reduced as the incorporation of the buffer layer diminishes the difference in hydrogen concentration at the p-i interface. This permits to get higher V_{oc}. However, the hydrogen of the buffer layer can diffuse in the ETP layer during its deposition at 400°C and this can explain why the V_{oc} of cell A is not reproduced in the cells containing an ETP i-layer. Secondly, the short wavelength response is enhanced, leading to an increase in J_{sc}. The quantum efficiency at short wavelengths is lower when no buffer layer is applied, as shown in figure 7.7. We think that the buffer layer enhances the carrier lifetime at the p-i interface by reducing the amount of excess carrier recombination in that region. The buffer layer displaces the defect-rich layer grown with ETP (region with a high defect density, thus a high recombination rate) from the p-i interface where the excess carrier concentration is very large and therefore the recombination in this region of the solar cell is diminished.

The H-diluted buffer layer seems to be more efficient in preserving the p-layer than the standard a-Si:H buffer layer. We believe that this is partially due to the fact that the

p-layer is then exposed to an H_2-rich plasma during the deposition of the buffer layer. Therefore H is re-introduced in the p-layer. Fujiwara *et al.* demonstrated by real time spectroscopic ellipsometry that the band gap of the p-layer was reduced by the loss of hydrogen into the vacuum when the plasma was extinguished [24]. They think that a chemical equilibrium of H exists between the plasma and the subsurface of the growing p-layer and when the plasma is turned off, the equilibrium is no longer sustained and H is emitted from the p-layer from a depth equal to the H mean free path, which is 200 to 400 Å. Then a new equilibrium is reached and a restructuring of the Si-Si bonds takes place. A H_2-plasma treatment of the p-layer prior to the i-layer deposition may permit to reverse this effect. In any case we obtain a higher cell performance with an H-diluted buffer layer (Cell D) than with a standard a-Si:H buffer layer (Cell C). This improvement can be seen in the ratio of quantum efficiencies taken at 0 V and −1 V (Fig. 7.8). The ratio increases for short wavelengths (blue part of the spectrum) when a buffer layer is used and is best when an H-diluted buffer is introduced at the p-i interface.

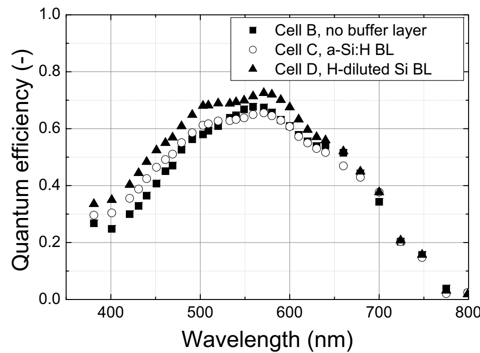

Figure 7.7: Quantum efficiency of cells B, C and D; no bias voltage is applied to the cells.

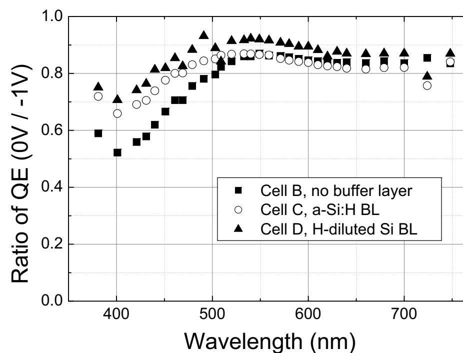

Figure 7.8: Ratio of quantum efficiencies taken at 0 V and -1 V of cells B, C and D.

In conclusion, a buffer layer at the p-i interface, prepared in a hydrogen-diluted plasma, yields higher cell performances compared to cells with either a standard rf PE-CVD a-Si:H buffer, an a-SiC:H buffer or no buffer at all. However, we notice that the efficiency of the ETP-CVD cells is still low compared to an rf PECVD cell. It seems that not any of the buffer layers entirely protects the p-layer from high-temperature exposure (here 400°C). Therefore the deposition temperature of the i-layer should be limited to 300ºC.

7.2.4 Buffer layer thickness series

We investigated the effect of varying the buffer layer thickness on the solar cell performance. In these experiments, the p-layer was grown at 250°C, the H-diluted a-Si:H buffer layer at 200°C and the ETP i-layer at high growth rate (31 Å/s) at 300°C, with hydrogen injected into the nozzle, the total thickness of the intrinsic layer (buffer + ETP) being kept constant at 445 nm. Finally the n-layer was deposited at 200°C. The thickness of the buffer layer, estimated from the growth rate of thicker samples, was varied from 0 nm to 21 nm.

The dependence of the solar cell performance on the buffer layer thickness at the p-i interface is shown in figure 7.9. We observe an increase in V_{oc} with increasing buffer layer thickness up to 10 nm. Then, for thicker buffer layers, the V_{oc} increase is negligible. The *FF* reaches a maximum for a cell with a 10 nm thick buffer layer. The variation of the buffer layer thickness has no influence on the current density that stays constant at 11 mA.cm^{-2} (not shown). Similar effects on V_{oc} and J_{sc} were observed by Munyeme *et al.* [22] when carrying out simulations with abrupt and graded band gap buffer layers. However, they found that the *FF* was maximal for a 2-nm thick buffer layer. Sakai *et al.* [21] found an optimum of the cell performance with a buffer layer of 14 nm thick.

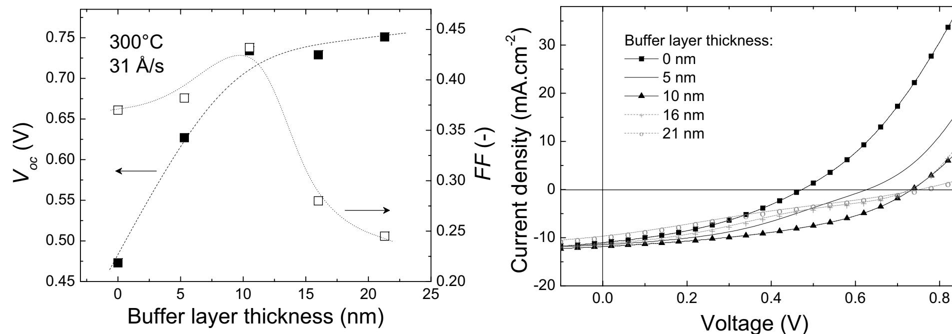

Figure 7.9: Dependence of buffer layer thickness on solar cell performance (full squares for V_{oc} and open squares for *FF*). Average of the 10 best cells.

Figure 7.10: *JV* curves for a-Si:H cells with buffer layer ranging from 0 nm to 21 nm thick. The characteristic of the best 0.1 cm^2 cell is shown.

In figure 7.10, the *JV* curves of the solar cells of the buffer layer thickness series are presented. The thickness of the buffer layer has a significant effect on the shape of the *JV* curve. In first place, the hydrogen-diluted buffer layer gives rise to a V_{oc} increase up to 0.75 V, J_{sc} remains constant and *FF* increases. A higher electric field, due to the presence of the buffer layer at the p-i interface (as seen with simulations, see Fig. 7.3), reduces the carrier recombination in that region and therefore increases the *FF*. Then, for the solar cells with a buffer layer thicker than 10 nm, a bump in the *JV*

curve appears, reducing the *FF*. This S-shape curve is associated with very high parallel and series resistances as seen in Fig. 7.10. Other workers [25] have observed this 'roll-over' behavior, but its origin remains unclear.

In conclusion we have carried out simulations and experiments to study the effect of a buffer layer at the p-i interface of a single junction a-Si:H solar cell. The intrinsic layer of the solar cells is prepared by ETP-CVD at high growth rate (31 Å/s) and high substrate temperature (300°C). The simulations show that the presence of a buffer layer increases the performance of the cell by augmenting the internal electric field at the interface and shifting the defect-rich layer further in the bulk of the cell away from the sensitive p-i interface. The experiments confirm the beneficial effect of a buffer layer at the p-i interface and a 10-nm thick hydrogen-diluted a-Si:H buffer layer seems enough to reduce interface recombination significantly and maximize the cell's performance. For thicker buffer layers, the solar cell performance is reduced. Nevertheless, cell efficiency does not exceed 4% and current density 12 mA/cm^2, which indicates that the combination of absorbing layer quality requirement (implying a high substrate temperature), together with the protection of the p-i interface from thermal damage (low T_{sub} needed), forms the limiting factor in obtaining highly efficient p-i-n solar cells. This concern had led to the development of ETP a-Si:H grown with an external rf bias applied on the substrate, in order to keep material properties at the moderate deposition temperature of 250°C.

7.3 Solar cells prepared with rf-biased ETP-CVD

Applying an rf bias to the substrate during amorphous silicon growth with the ETP technique permits to reduce the substrate temperature while keeping the properties of the thin layer, as seen in chapter 5. As a result of ion bombardment and energy transfer, surface diffusion of precursors, among other processes, is enhanced. This feature is a real advantage for the fabrication of p-i-n solar cells because the p-layer and/or the TCO layer are sensitive to heat and their properties may be altered during the deposition of the intrinsic layer at high substrate temperature. Therefore we will use in this section ETP i-layers deposited at 250°C with an external rf bias on the substrate.

7.3.1 Power series

For the integration of rf-biased ETP-CVD a-Si:H in solar cells, Asahi U-type SnO_2:F coated glass is used as front contact. The following cell structure was used:

- Using rf PE-CVD, a 12-nm thick a-SiC:H p-layer is deposited at 180°C in the AMOR deposition system. On top of this layer, a hydrogen diluted a-Si:H buffer layer (5 nm) and a standard a-Si:H layer (20 nm) are deposited, also with rf PE-CVD. The aim of this second 'buffer layer' is to protect the p-i interface.

- After deposition of the buffer layers, the cell is exposed to air when transferred from the rf PE-CVD set-up to the CASCADE set-up for the deposition of the ETP layer. The gas flows used for the deposition of the ETP layer are as follows: Φ_{Ar} = 600 sccm, Φ_{SiH4} = 200 sccm, Φ_{H2} = 200 sccm and Φ_{H2Noz} = 150 sccm. In order to control the substrate temperature, which is kept here at 250°C, 400 sccm of helium is used as back flow. The pressure in the arc is 0.42 bar and in the reactor 0.20 mbar. The rf bias applied to the substrate holder is varied and the growth rate related to each bias is given in table 7.5. The maximum rf bias that is applied is 50 W because the plasma cannot be sustained for higher power. The intrinsic layer has a thickness of 280 nm.

- The n-layer is grown at 200°C in the rf PECVD chamber of CASCADE. Finally, silver and aluminum layers are deposited as reflective back contacts. The area of the solar cells is defined by the metal contact and is here 4 mm × 4 mm.

The CASCADE setup has only one rf chamber. It was decided to use this chamber for n-type depositions only in order to avoid cross-contamination.

Cell name	P_{rf} (W)	$\lvert V_{dc}\rvert$ (V)	Growth rate (nm/s)
E	0	0.5	1.04
F	8	19.6	1.06
G	15	29.8	1.21
H	20	34.9	1.29
I	30	36.0	1.31
J	40	38.4	1.35
K	50	40.2	1.39

Table 7.5: Applied rf power to the substrate, measured self-bias and growth rate of the rf biased ETP-CVD a-Si:H layer applied in single junction p-i-n solar cells, and the corresponding cell.

The self-bias voltage, V_{dc}, that develops on the substrate holder when an external rf power is applied during the deposition of the ETP-layer, determines the average energy of the bombarding ions on the growing surface. We saw in chapter 5 that a mild ion bombardment of 20 eV was sufficient to improve the properties of the a-Si:H thin layer, such as the Urbach energy or the defect density. Figure 7.11 shows the external parameters (open-circuit voltage, fill factor, short-circuit current density and efficiency) of the solar cells with an rf-biased ETP i-layer versus $\lvert V_{dc}\rvert$. For each condition the average of the best 10 cells, in terms of efficiency, is presented. First of all, the solar cell deposited with standard ETP-CVD, without additional rf bias, performs better than the cells obtained so far of which the ETP i-layer was grown at 350 or 400°C. Cell E, grown at 250°C, has an efficiency above 5% against an efficiency below 4% for cell D (see table 7.4), grown at 400°C. This improved performance indicates that, as expected, the combination p-layer + buffer layer can sustain a

temperature of 250°C better than of 400°C. However, as the substrate temperature is lowered, the growth rate has to be lowered as well from ~19 Å/s to 10 Å/s.

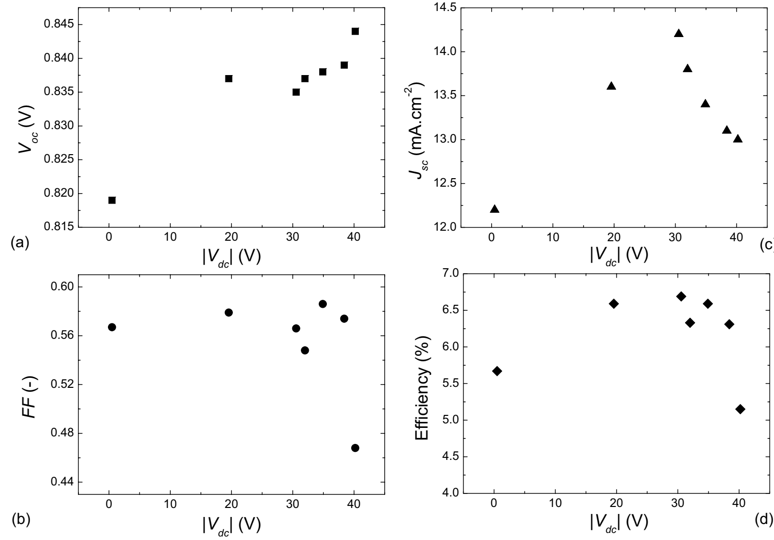

Figure 7.11: Open-circuit voltage (a), fill factor (b), short-circuit current density (c) and efficiency (d) of solar cells with the intrinsic layer deposited with rf-biased ETP-CVD at high growth rate (~1 nm/s) and low substrate temperature (250°C) versus bias voltage, $|V_{dc}|$. The average values of the 10 best cells, in terms of efficiency, are presented.

Secondly, it can be seen that the rf power applied on the substrate holder has a significant influence on all the solar cell parameters. The V_{oc} increases with $|V_{dc}|$, whereas the *FF*, although it first also increases with $|V_{dc}|$, drops for higher values (≥ 40 V). A higher V_{oc} indicates a better p-i interface and we believe that the initial layer grown with ETP-CVD, the so-called defect-rich layer, is either reduced in thickness or its defect density is reduced, leading to a higher V_{oc}. The J_{sc} is maximal for $|V_{dc}|$ around 30 V. Finally the efficiency of the single junction solar cells is enhanced for $|V_{dc}|$ in the range 20 V to 35 V. We observe that the solar cells fabricated with an rf-biased ETP i-layer have a better performance than the cells fabricated with standard ETP layer grown at 250°C. The opto-electronic properties of the a-Si:H films can be improved considerably when a moderate rf substrate bias voltage (~20-35 V) is applied, as reported elsewhere [26]. However, when the power applied on the substrate becomes relatively high, which is in our case around 40 V, the cell's efficiency drops. We have to keep in mind that although the average energy of the impinging ions is 40 eV, the ion energy is in fact distributed around that value and consequently some ions can have a much higher energy [27]. These ions might be responsible for atom displacement, or even atom sputtering from the growing surface,

leading to the creation of nano-voids and a drop in the cell's performance. The best condition is found to be for 30 V bias voltage (condition I), with an average efficiency of 6.7%. However, the best cell was obtained for a 20-V bias (condition F) with an efficiency of 6.97% and a *FF* of 0.607.

A low microstructure parameter R^* of the absorbing a-Si:H layer, preferably below 0.1 is often mentioned as a prerequisite for an efficient a-Si:H solar cell [28]. Figures 7.12 and 7.13 show that the cell's short-circuit current density has a direct correlation with some properties of the solar cell intrinsic layer, such as the R^* value and the light conductivity, σ_L. J_{sc} decreases with increasing R^* value. Moreover J_{sc} presents the same trend as σ_L (see Fig. 7.13). The R^* parameter is a figure of merit for the nano-void density in a layer because the lower the R^*, the lower the density of hydrogen bonded in the SiH_2 configuration compared to that of H bonded in the SiH configuration and because the SiH_2 configuration can be found mainly on the surface of nano-voids [26]. We think that a high R^* value entails a lower light conductivity as more nano-voids are present in the material and the probability that carriers do cross the material and reach the collecting electrode before recombination is lower. Therefore, when such a layer is incorporated into a solar cell, J_{sc} is limited.

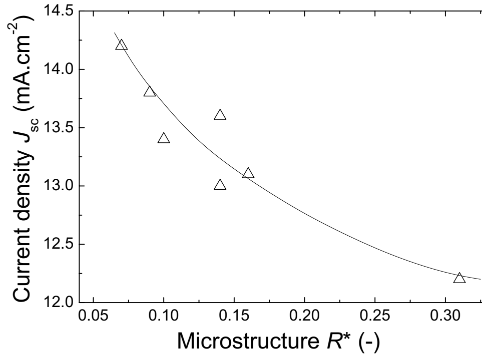

Figure 7.12: Current density J_{sc} of solar cells E to K versus R^* of corresponding single layers. The line is a guide to the eye.

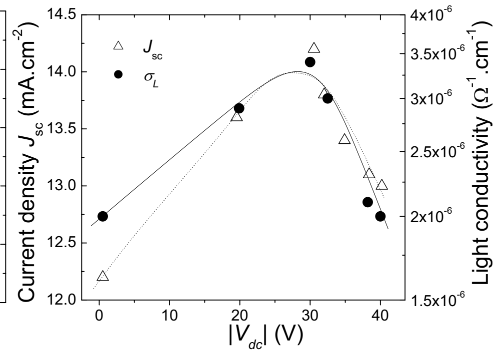

Figure 7.13: Correlation between solar cell's current density, J_{sc}, and single layer's light conductivity, σ_L, versus bias voltage $|V_{dc}|$. Lines are guide to the eye.

During rf-biased ETP-CVD, ions in the vicinity of the growing surface acquire extra energy and when they impinge on the surface, they either transfer their extra energy to the surrounding species, so also to the growth precursors, thereby increasing their mobility and the chance they reach a favorable growth site, or they transfer their energy to the atoms on the (sub-)surface, thereby allowing these atoms to rearrange in a more relaxed position (lower potential energy). Moreover, large silicon cluster ions from the plasma are believed to be broken by impact on the surface, leading to an a-Si:H layer of higher properties. This phenomenon is more likely to happen when the

bombarding ions have a mild energy; in our case it seems that 20 to 30 eV is the optimum. For higher energies, other phenomena occur, such as atom displacement that can be detrimental to the cell's performance as the lattice is then damaged.

Figure 7.14 shows the current-voltage characteristics of the best p-i-n solar cells. For clarity, only the *JV* curves of cells E, F, G and K, of which the i-layer was prepared respectively with 0, 20, 30 and 40 V rf-bias voltage, is shown. Cells H, I and J have a similar behavior as cell G. It is clear that moderate ion bombardment during the growth of the i-layer increases the J_{sc} and *FF*, although these parameters decrease for $|V_{dc}|$ above 30 V (see cell K). The best characteristics are obtained for a bias voltage of 20 V (cell F), the fill factor increasing from 0.58 up to 0.61 and the efficiency increasing from 5.9 up to 7.0%.

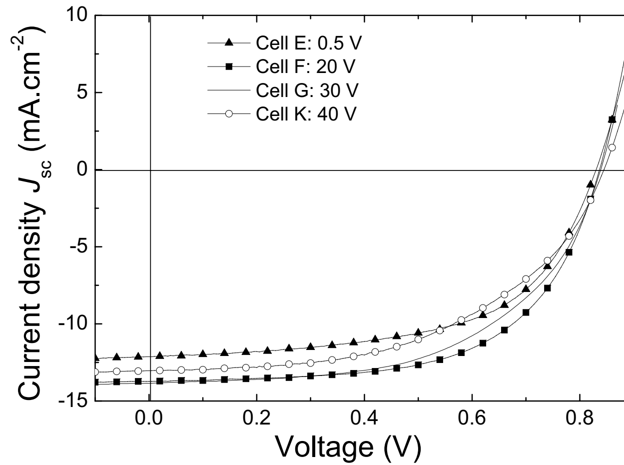

Figure 7.14: *JV* characteristics of solar cells with the absorbing layer grown by rf-biased ETP-CVD at 250°C and 10 Å/s.

Spectral response measurements were carried out on the solar cells and the quantum efficiency obtained with no bias voltage applied to the cell during the measurement is presented in Figure 7.15. Again, only the QE results of cells E, F, G and K is shown, as cells H, I and J have a similar behavior as cell G. It is obvious that rf-biased ETP-CVD leads to an improved solar response of the cell, particularly in the short wavelength region of the spectrum. Moreover, we observe that, although a 40-V bias leads to a cell with the highest response in the blue part of the spectrum (cell K), the best cell is cell F, with a 20 V bias, as it has a high response in the blue and the highest response in the red part of the spectrum (longer wavelengths). The higher performance of cell F above the other cells is demonstrated with the ratio of quantum efficiencies at 0 bias to −1 V bias presented in figure 7.16. This QE ratio gives an indication of the recombination of carriers in the i-layer [29]. This graph shows that rf-biased ETP cells have a better behavior than the cell with a standard ETP-CVD i-layer,

as then the QE ratio is closer to unity for a larger range of wavelength. Apparently, in these rf-biased ETP cells the internal electric field distribution is such that most generated charge carriers are collected without applying a reverse bias. On the contrary, cell E has a low QE ratio in the 400-500 nm region of the QE plot, which corresponds to the absorption in the first nanometers of the i-layer. This observation indicates that recombination occurs at or near the p-i interface and this latter limits the charge collection. We think that the addition of rf bias on the substrate avoids or at least reduces the growth of a defect-rich layer (DRL) at the beginning of the ETP-CVD layer, which is suspected to be usually present when no bias is used [30], thereby improving the p-i interface.

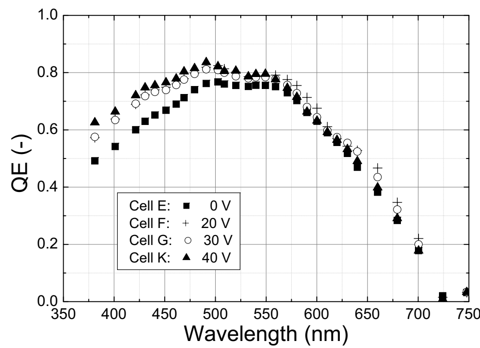

Figure 7.15: Quantum efficiency for cells with an rf-biased ETP-CVD i-layer. No bias was applied during the QE measurement.

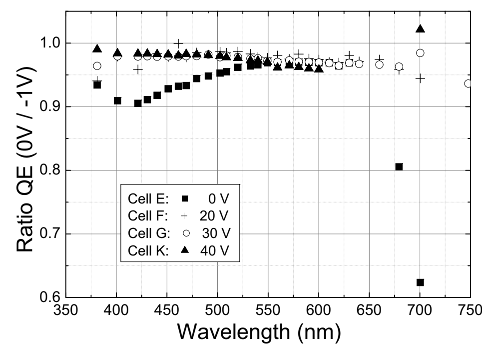

Figure 7.16: Ratio of quantum efficiencies taken at −1 V and 0 V of cells with an i-layer deposited by rf-biased ETP-CVD.

We conclude that applying an rf bias on the substrate during the deposition of a-Si:H ETP i-layer of a cell leads to the improvement of the cell performance for two reasons. First of all because the open-circuit voltage is enhanced. We believe that the DRL is reduced, resulting in a p-i interface of better quality. The spectral response of the cell in the blue part of the spectrum is improved. And secondly, the current density is enhanced, because of better properties of the intrinsic layer, such as a lower R^* value or a reduced defect density.

Applying an rf bias improves the cell's performance, but the bias does not seem to have a strong influence on the performance for the range considered here, up to a $|V_{dc}|$ of around 40 V. For higher voltages, the cell's performance drops considerably. We think that a high bias leads to a strong ion bombardment, which is detrimental for the deposited layer. The R^* value, representative of the nano-void density, increases. A mild $|V_{dc}|$ is sufficient to improve the layer properties and thus the cell's performance, and this with a low substrate temperature of 250°C and a relatively high growth rate of 10 Å/s. The best solar cell efficiency achieved with these conditions is 7%.

7.3.2 Annealing series

From the microelectronic industry, anneal steps or heat treatments of a wafer, are known to be beneficial to either activate the dopants or to relieve internal stresses. Depending on the time and temperature of the anneal, the properties of the material are modified and better contact between semiconductor and metal layers can be obtained. A double annealing treatment has been chosen to optimize the relaxation of the ETP a-Si:H network in a solar cell for two reasons. First of all, low-temperature annealing of a solar cell when it is complete has nearly no effect on its final performance [31]. Furthermore, annealing at higher temperature can deteriorate the metal contacts and thus the cell performance. It appears that to carry out the annealing step in two stages permits to adapt the treatment to a specific purpose: at moderate temperature before metallization to redistribute the density of states in the i-layer and at low temperature after metallization to improve the contact between the n-layer and the Ag layer.

The solar cells used for the annealing series have the same structure and the same deposition conditions as the cells forming the power series (see paragraph 3.1). A short H_2-plasma treatment of the p-layer is carried out, which has proved to improve the interface between p- and buffer-layers, as found by Myong *et al.* [32] for similar conditions. The a-Si:H intrinsic layer is deposited by ETP-CVD with 8-W rf bias on the substrate at 250°C ($|V_{dc}|$ = 20 V, growth rate of ~11 Å/s). The i-layer has a thickness of 280 nm. The annealing treatment of the cells is carried out in the rf chamber of the CASCADE set-up straight away after deposition of the n-layer under 50 sccm He back flow to control the substrate temperature. There is no vacuum break or cooling down of the cells prior to the annealing step.

The annealing conditions (time and temperature) and the external parameters of the corresponding annealed solar cells are given in table 7.6. The average of the 10 best cells, in terms of efficiency, is presented, with the efficiency of the best performing cell of that condition. The annealing step was carried out before metallization. For the low annealing temperature of 160°C (Cell M), a longer annealing time of 30 min instead of 10 min was chosen. Cell P was exposed to a graded temperature from 200°C down to 160°C in 12 min.

Considering the conditions L, M, N and O, in which the annealing temperature was increased, we observe that the annealing treatment has a beneficial effect on the solar cell performance for annealing temperatures below 225°C. Annealing at 225°C (Cell O) results in a lower solar cell efficiency than the 'as deposited' one. We can see that on average V_{oc} is improved after the annealing step. However J_{sc} seems to decrease with increasing annealing temperature, whereas the *FF* is improved only for an anneal at 200°C. When a graded temperature treatment is used (Cell P), from 200°C down to 160°C, the best effect is obtained and all external parameters are improved, in particular J_{sc}. An average efficiency of 7.3% is achieved for the single junction p-i-n solar cell deposited at high growth rate. Furthermore, an efficiency of 7.44% is

obtained for the best cell with an annealing from 200°C down to 160°C, which represents more than 5% improvement compared to the solar cell that did not undergo an annealing step (best cell of condition L, efficiency: 6.97 %).

Cell name	Annealing temperature (°C)	Annealing time (min)	V_{oc} (V)	J_{sc} (mA.cm^{-2})	FF (-)	η (%)	η best cell (%)
L	As deposited	_	0.837	13.6	0.579	6.59	6.97
M	160	30	0.847	13.9	0.573	6.76	6.95
N	200	10	0.847	13.5	0.622	7.03	7.12
O	225	10	0.838	13.1	0.565	6.19	6.79
P	200 ↓ to 160	12	0.847	14.4	0.598	7.31	7.44

Table 7.6: Annealing conditions and performance of the corresponding solar cells deposited with rf-biased ETP-CVD and a bias voltage of 20 V, before metallization. The average of the 10 best cells (based on the efficiency) is presented, as well as the efficiency of the best cell for each condition.

After metallization, an anneal step at 150°C for 10 min was carried out. In order to avoid silver and aluminium alloy formation and reflectivity loss of Ag, it is important that the first annealing step is carried out before the metallization to be able to perform it at relatively high temperatures (160°-200°C). However, a second anneal step after metallization and at lower temperature is beneficial for the cell performance, as a better contact is achieved between the n- and silver layers.

The solar cell performances after the second annealing step are presented in table 7.7. We can see that for the three annealing conditions presented previously, the annealing step after evaporation of the metal contacts improves the performance of the solar cells further. In particular V_{oc} and FF increase. Furthermore, this procedure of double annealing resulted in a best-cell efficiency of 8.0%. This is a record efficiency for a-Si:H p-i-n solar cell deposited with the ETP technique.

Cell name	Annealing temperature (°C)	V_{oc} (V)	J_{sc} (mA.cm^{-2})	FF (-)	η (%)	η best cell (%)
M'	160	0.860	13.7	0.622	7.32	7.38
N'	200	0.852	14.1	0.622	7.46	7.73
P'	200 ↓ to 160	0.861	14.3	0.630	7.75	7.95

Table 7.7: Performance of solar cells deposited with rf-biased ETP-CVD after 10 min anneal after metallization. The average of the 10 best cells (in terms of efficiency) is presented, as well as the efficiency of the best cell for each condition.

The influence of the annealing treatments on the solar-cell performance can be explained as follows. As the deposition of the ETP layer is very fast (less than 5 min

for the 280 nm thick i-layer), we think that the Fermi level in the i-layer, grown on top of the p-layer, is pinned in the lower part of the band gap throughout the entire layer. This effect results in a higher defect density in the band gap close to the conduction band, according to the defect-pool model [33].

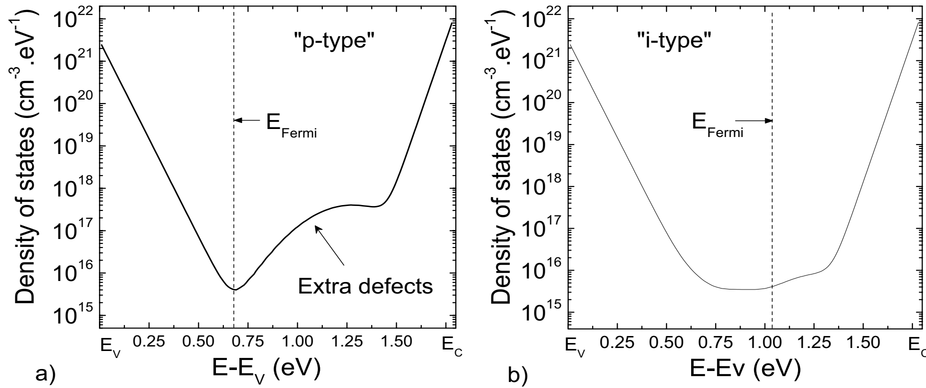

Figure 7.17: Simulations of a-Si:H material density of states based on the defect-pool model. a) DOS of the i-layer after deposition on the p-layer. b) DOS of the same i-layer after the annealing treatment.

Figure 7.17 (a) illustrates how the density of states (DOS) may look in that case. The Fermi level being situated close to the valence-band edge, the material has a p-type distribution of DOS. As the Fermi level is pinned in the i-layer, weak band bending is induced in this layer. Then, after the n-layer deposition, an internal electric field appears in the cell and the Fermi level, at the i-n interface, shifts in the upper part of the band gap. However, the defect-density distribution in the i-layer cannot equilibrate sufficiently quickly to adjust to this new situation. We think that the anneal step allows the density of states to re-equilibrate towards a distribution equivalent to that in intrinsic material, as shown in figure 7.17 (b). Therefore, the overall defect density in the layer is reduced, leading to a higher J_{sc} and *FF*. The positive effect of moderate temperature anneal can be further explained by the re-equilibration of the thermally generated defects, thanks to a redistribution of mobile hydrogen atoms [34,35]. The reduction in defect-state density at low temperature treatment was demonstrated by J. Hi *et al.* [36]. Hydrogen redistribution in the a-Si:H film may reduce the DOS by annihilation of dangling bonds. At higher temperatures, the anneal sample showed degradation due to out-diffusion of weakly bonded hydrogen. Panwar *et al.* [37] found a material quality improvement of the a-Si:H films with anneal treatment of the layers at temperatures up to 250°C. However, the films were deposited at room temperature, thus annealing was carried on a film far away from its equilibrium. In general, the annealing temperature should not exceed that of the film deposition.

Figure 7.18 shows the *JV* characteristics of the best cell at different stages: as-deposited, after the first and after the second anneal treatment. The first anneal step is carried out with a graded temperature (condition P). We observe in a first place that J_{sc} increases following the anneal step. The material relaxes and the DOS is rearranged as the Fermi level reaches a position at the center of the band gap, leading to fewer defects in the low part of the gap. The quality of the intrinsic layer is improved and a better carrier collection takes place from the i-layer. This improvement can also be noticed from the spectral response measurement (see figure 7.19). The second annealing step results in a higher V_{oc} and *FF*, which can be explained by a better contact between the active layers of the cells and the metal layers.

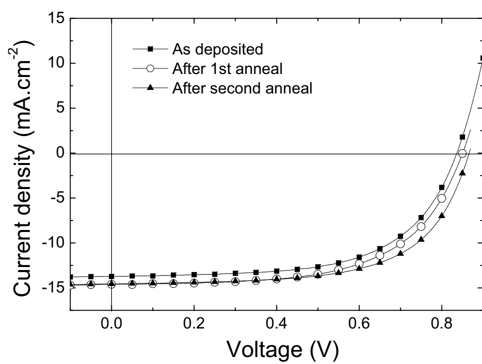

Figure 7.18: *JV* characteristics of solar cells deposited with rf biased ETP-CVD, in the as-deposited state and in the annealed state, before and after metallization.

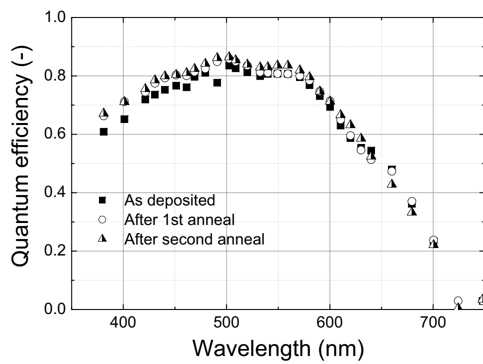

Figure 7.19: Quantum efficiency taken at −1 V reverse bias of rf biased ETP solar cells, in the as-deposited state and in the annealed state, before and after metallization.

Figure 7.20 summarises the results of the double annealing experiment on solar cells with an i-layer deposited by ETP-CVD with a moderate rf bias of 20 V on the substrate. The first annealing step (ramping down from 200° to 160°C), before metallization, enhances most of all the current density by improving the quality of the intrinsic layer, and therefore increasing the carrier collection from that region of the cell. The second annealing step results in the increase of the open-circuit voltage and the fill factor. The double annealing treatment leads to a significant solar cell improvement of 17%, to an average efficiency of 7.75% and a record efficiency of 8.0%.

In conclusion, we have demonstrated the positive effect of mild ion bombardment during ETP-CVD a-Si:H deposition, induced by rf bias on the substrate, on the solar cell performance. Double annealing of the cell further enhances the carrier collection and leads to initial cell efficiencies as high as 8.0% for an a-Si:H p-i-n single junction cell deposited at 11 Å/s and 250°C. This result constitutes the best efficiency obtained so far for an ETP cell.

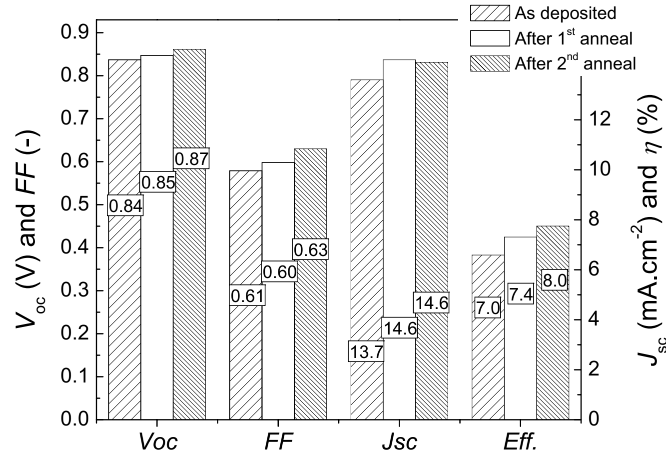

Figure 7.20: External parameters of solar cells deposited with rf-biased ETP-CVD in the as-deposited state and after annealing (first, anneal of the active layer; second, anneal of the metal contacts). The bars represent the average of the 10 best cells, whereas the best cell value is indicated on the bars.

7.4 Conclusions

In the first place, we have studied the effect of a buffer layer at the p-i interface on the performance of a-Si:H solar cells with a p-i-n structure and an intrinsic layer grown at high rate, high substrate temperature, with ETP-CVD. The experimental and simulation results show that initial device performance is enhanced with the insertion of an hydrogen-diluted a-Si:H layer at the p-i interface. A thickness of 10 nm is sufficient to improve the V_{oc} and the *FF*. Thanks to a stronger internal electric field at the p-i interface, the charge carriers are swept away faster from that region than when there is no buffer layer and the chance of recombination is then reduced. Moreover, the initial layer grown with ETP-CVD, so-called defect-rich layer, is moved away from the region where charge carrier generation is the highest. A lower defect density at the p-i interface results in less carrier recombination and thus higher *FF*. Finally, thermal damage of the p-layer, due to the high substrate temperature during deposition of the ETP intrinsic layer, is diminished and a dense buffer layer acts as a barrier against diffusion of hydrogen or boron from the p-layer.

Secondly, we have examined the influence of an external rf bias on the substrate during ETP-CVD. The addition of rf bias opens new possibilities for deposition of a-Si:H at high deposition rates. The assisting surface ion bombardment during high rate a-Si:H deposition at moderate substrate temperature (≥ 10 Å/s and 250°C) results

in a-Si:H with lower defect density, improved microstructure and opto-electronic properties. A mild substrate rf bias in the range of 20 to 30 V suffices to improve the material properties considerably. Furthermore, as a result of a double annealing treatment, the density of states re-equilibrates deep in the intrinsic ETP layer and the carrier collection in the cell improves. With an rf-biased ETP a-Si:H i-layer grown at 11 Å/s and an optimized cell structure we obtained a record single junction ETP a-Si:H solar cell: without highly reflective back contact employed, initial efficiencies of 8% have been achieved.

References

[1] P.K. Bhat, C. Marshall, J. Sandwisch, H. Chatham, R.E.I. Schropp, and A. Madan, 20th IEEE Photovoltaic Specialists Conference **1** (1988) 91

[2] S. Bauer, B. Schröder, W. Herbst, and M. Lill, Proceedings of the 2nd World Conference on PV Solar Energy Conversion (1998) 363

[3] R.H. Franken, C.H.M. van der Werf, J. Löffler, J.K. Rath, and R.E.I. Schropp, 3rd International Conference on Hot-Wire CVD Process (2004) 377

[4] U. Kroll, D. Fischer, J. Meier, L. Sansonnens, A. Howling, and A. Shah, Mater. Res. Soc. Proc. **557** (1999) 121

[5] H. Takatsuka, M. Noda, Y. Yonekura, Y. Takeuchi and Y. Yamauchi, Sol. Energy **77** (2004) 951

[6] W.M.M. Kessels, R.J. Severens, A.H.M. Smets, B.A. Korevaar, G.J. Adriaenssens, D.C. Schram, and M.C.M. van de Sanden, J. Appl. Phys. **89** (2001) 2404

[7] A.J.M. van Erven, R.C.M. Bosch, A.W. Weeber, and M.D. Bijker, 19th European Photovoltaic Solar Energy Conference and Exhibition, 2CV.2.20 (2004)

[8] B.A. Korevaar, Ph.D. thesis, Eindhoven University of Technology (2002)

[9] A.H.M. Smets, D.C. Schram and M.C.M. van de Sanden, Mat. Res. Soc. Proc. **609** (2000) A7.6

[10] D.M. Tanenbaum, A. Laracuente and A.C. Gallagher, Mat. Res. Soc. Proc. **336** (1994) 49

[11] A.H.M. Smets, J.H. van Helden and M.C.M. van de Sanden, Mat. Res. Soc. Proc. **664** (2001) A22.4

[12] T. Shimizu, X. Xu, H. Kidoh, A. Morimoto and M. Kumeda, J. Appl. Phys. **64** (1988) 5045

[13] I.M.P. Aarts, B. Hoex, J.J.H. Gielis, C.M. Leewis, A.H.M. Smets, R. Engeln, M. Nesladek, W.M.M. Kessels, M.C.M. van de Sanden, Mat. Res. Soc. Proc. **762** (2003) 111

[14] B.A. Korevaar, A.M.H.N. Petit, C. Smit, R.A.C.M.M. van Swaaij and M.C.M. van de Sanden, 29th IEEE Photovoltaic Specialists Conference (2002) 1230

[15] M. Zeman, J.A. Willemen, L.L.A. Vosteen, G. Tao, and J.W. Metselaar, Solar Energy Materials and Solar Cells **46** (1997) 81
[16] J. Zimmer, H. Stiebig and H. Wagner, J. Appl. Phys. **84** (1998) 15
[17] M.J. Powell and S.C. Deane, Phys. Rev. B **48** (1993) 10 815
[18] Q. Wang, E. Iwaniczko, Y. Xu, B.P. Nelson, A.H. Mahan, R.S. Crandall and H.M. Branz, 28th IEEE Photovoltaic Specialists Conference (2000) 717
[19] F.H. Karg, K. Dietrich, W. Kusian and H. Kausche, 20th IEEE Photovoltaic Specialists Conference **1** (1988) 149
[20] M. Hundhausen, P. Santos, L. Ley, F. Habraken, W. Beyer, R. Primig and G. Georges, J. Appl. Phys. **61** (1987) 556
[21] H. Sakai, T. Yoshida, S. Fujikake, T. Hama and Y. Ichikawa, J. Appl. Phys. **67** (1990) 3494
[22] G. Munyeme, M. Zeman, R.E.I. Schropp and W.F. van der Weg, Phys. Stat. Sol. **1**, n° 9 (2004) 2298
[23] H. Tanaka, N. Ishiguro, T. Miyashita, N. Yanagawa, M. Sadamoto, M. Koyama, K. Miyachi, Y. Ashida and N. Fukuda, 23rd IEEE Photovoltaic Specialists Conference (1993) 811
[24] H. Fujiwara, J. Koh, C.R. Wronski and R.W. Collins, Appl. Phys. Lett. **74** (1999) 3687
[25] X. Deng, W. Wang, S. Han, H. Povolny, W. Du, X. Liao and X. Xiang, Inter. J. Mod. Phys. B **16** (2002) 57
[26] A.H.M. Smets, W.M.M. Kessels and M.C.M. van de Sanden, Mat. Res. Soc. Symp. Proc. Vol. **808** (2004) A9.21
[27] S.B. Wang and A.E. Wendt, J. Appl.Phys. **88** (2000) 643
[28] R.E.I. Schropp and M. Zeman, *Amorphous and microcrystalline silicon solar cells*, Kluwer Academic Publishers, Dordrecht (1998)
[29] R.R. Arya, A. Catalano and R.S. Oswald, Appl. Phys. Lett. **49** (1986) 1089
[30] A.M.H.N. Petit, M. Zeman, R.A.C.M.M. van Swaaij and M.C.M. van de Sanden, Mater. Res. Soc. Proc. **762** (2003) 369
[31] Unpublished results
[32] S.Y. Myong and K. S. Lim, Appl. Phys. Lett. **86** (2005) 033506
[33] M.J. Powell and S.C. Dean, Phys. Rev. B **53** (1996) 10 121
[34] G.D. Cody, T. Tiedje, B. Abeles, B. Brooks and Y. Goldstein, Phys. Rev. Lett. **47** (1981) 1480
[35] D. Carlson, G. Ganguly and G. Lin, Mater. Res. Soc. Proc. **664** (2001) A25.4.1
[36] J. Hi, R. Wallace, J. Palmer and W.A. Anderson, 23rd IEEE Photovoltaic Specialists Conference (1993) 977
[37] O.S. Panwar, C. Mukherjee and R. Bhattacharyya, Sol. Energy Mat. & Sol. Cells **57** (1999) 373

Chapter 8

Illumination of ETP a-Si:H and subsequent material and device degradation

8.1 Introduction

Hydrogenated amorphous silicon (a-Si:H) is nowadays commonly used for the fabrication of thin film solar cells. A low-temperature production and a low material cost are the main reasons for a-Si:H solar cell production. Moreover the abundance of raw material and the relative simplicity of the production technique by chemical vapor deposition (CVD), compared to that for monocrystalline silicon solar cells, are advantageous aspects related to a-Si:H. However, a major drawback of this material compared to its crystalline counterpart is the slow degradation of the material properties when exposed to sunlight. This effect, called the Stabler-Wronski effect (SWE) after its discoverers [1], is characterized by the decrease of dark and light conductivities upon prolonged exposure to intense light, as well as by the increase of dangling bond-related spin density [2]. The SWE is a major problem for a-Si:H solar cells, as it deteriorates the cell's performance. In order to understand and control the Staebler-Wronski effect, numerous studies have been carried out over the last 25 years. The results obtained depend not only on the intensity of the illumination, but also on the temperature at which the illumination is carried out and the form of illumination, continuous wave or pulsed [3]. In spite of that research, there is still a considerable debate about the underlying mechanism [4]. However, the SWE is a self-saturating process and therefore the solar cells reach a stabilized efficiency after a certain time of

light soaking. Another characteristic of the SWE is its complete reversibility upon thermal annealing of a-Si:H in the dark at temperatures above 150°C.

The a-Si:H deposited by expanding thermal plasma CVD is also subject to the SWE and the study of ETP a-Si:H behavior upon light soaking constitutes the topic of this chapter. In the first section, the general features about the SWE microscopic origin are discussed. Then after giving the experimental details, the degradation upon illumination of single layers grown under various conditions is presented. Finally the degradation of these layers incorporated into single junction p-i-n solar cells is described. The correlation between initial material properties and degradation is studied, in particular the influence of plasma chemistry and of ion bombardment on the stability of the ETP material.

8.2 The Staebler-Wronski effect

What is the SWE?

The Staebler-Wronski effect is the light-induced degradation of undoped a-Si:H and its alloys. It describes a metastable process, the creation of additional states in the mobility gap, occurring during non-thermal equilibrium conditions. These reversible changes in density of localized gap states are observed mainly after illumination with intense light. However, metastable changes have also been observed after rapid quenching or charge accumulation [5], after keV electron bombardment [6] or after current stress of forward-biased p-i-p structures without illumination [7]. On the other hand, Staebler and Wronski showed that illumination does not cause degradation in diode-like devices when a strong reverse bias is applied [8].

The principal observations associated with the SWE are the decrease in conductivity and the generation of metastable defect configurations in the band gap [9]. These extra defects are indeed suspected to be responsible for the material and device degradation. Due to the location of these new defects in the band gap, below 1.4 eV, the Fermi level shifts towards mid gap, thereby decreasing the dark conductivity. The metastable defects act as recombination centers, thereby decreasing the lifetime of excess carriers and influencing the electronic and optical properties of a-Si:H. The creation of bulk dangling bond defects may not be the only process behind the SWE, but it is almost certainly the dominant one [10].

Next to these experimental observations, structural changes of the material, like material expansion, have been related to the SWE [11]. Internal compressive stress significantly increases upon exposure to intense light [12]. However, these structural changes seem to occur in parallel to the SWE, therefore they are not thought to be a precursor of it [13].

Another feature of the SWE is its self-limiting and reversible character. As a matter of fact, the light-induced degradation process stops after saturation is reached and both

material properties and solar cell efficiency stabilize. The performance can be recovered after an annealing step, where relaxation into the thermal equilibrium ground state occurs.

What gives rise to metastability? Physical model

The most generally accepted model describing the defects creation is the "bond-breaking" model, developed by Stutzmann, Jackson and Tsai [14]. The model is based on the non-radiative recombination of electron-hole pairs. The photo-excited excess carriers are first trapped at shallow or deep traps. Shallow trapping occurs in the valence and conduction band-tail states (regions II and IV of the density of states, see figure 8.1), at weak Si-Si bonds. Subsequently, in the course of bimolecular recombination of electrons and holes, weak Si-Si bonds are broken, creating a pair of dangling bonds in the amorphous network (defect situated at midgap, see region III in figure 8.1). The non-radiative recombination involves a multi-phonon process, where local phonons provide the energy necessary to overcome the potential barrier, E_B, of about 1 eV separating the stable ground state from the metastable defect state, as depicted in figure 8.2. The defect creation and annealing is described by the potential well model [10] and by the configuration-coordinate diagram represented in figure 2. The lower energy well E_0 in figure 8.2 represents the annealed state (the fully coordinated network), while the higher energy well E_1 represents the metastable state (a dangling-bond defect) [10]. E_A is the annealing potential barrier and is the energy needed for a defect to go from the metastable state to the ground state.

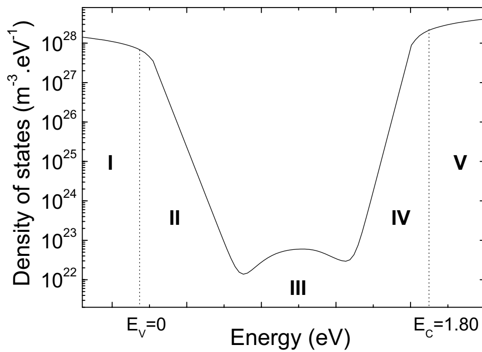

Figure 8.1: Schematic diagram of the DOS in a-Si:H showing the extended states regions (I and V), the tail regions (II and IV) and the midgap states region (III).

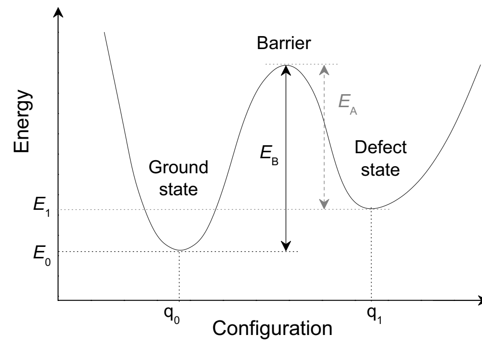

Figure 8.2: Configurational coordinate diagram of the equilibration between the ground state and the metastable state, separated by a potential energy barrier.

The defect density depends sublinearly on both the generation rate of photoexcited electrons and holes, *G*, and the illumination time, *t*, and is expressed as:

$$N_d(t) \propto c_{SW} G^{2/3} t^{1/3} \quad (1)$$

where N_d is the total defect density and c_{SW} a constant describing the average efficiency of tail-to-tail transitions for the creation of new dangling bonds. This equation is valid when sufficiently long illumination times are used (i.e., $N_d(t) > 2*N_d(0)$ [14]). The number of created metastable defects depends on illumination time and intensity, but is nearly independent of temperature [5]. However for temperature ≥ 90°C, the effects of simultaneous annealing (thermal and light-induced annealing) of the metastable defects cannot be neglected anymore [15]. In any case, the rate of creation of new dangling bonds depends on the density of already existing dangling bonds and is given by:

$$dN_d/dt \propto c_{SW} . (G/N_d)^2 \quad (2)$$

Up to now the SWE is not entirely understood and the microscopic details related to the defect creation process remain uncertain. Contamination by impurities like oxygen, nitrogen or carbon seems to be excluded, at least for concentrations below 10^{19} cm^{-3} [14, 16], although Crandall *et al.* [17] suggested first the opposite. The exact role of hydrogen in the metastability, despite the number of studies on that subject, is still not resolved. No experimental proof of H involvement in the formation of metastable dangling bonds is actually available. Stutzmann [4] postulates that as the thermal activation energy to return from a metastable state to a stable state is similar to the diffusion activation energy of H in a-Si:H (~1.1 eV), H is suspected to have a role in the SWE. It is widely accepted that the defect creation process can be mediated by H diffusion. Branz proposed the H collision model, based on the long-range diffusion of H and its mediation in the reconfiguration of dangling bonds through metastable complex [18, 19]. Dalal *et al.* found that the hydrogen chemistry of the reactive plasma during growth plays an important role in determining the stability of an a-Si:H layer [20] and the use of H-dilution plasma produces solar cells of higher stability than He-dilution plasma.

However, other mechanisms that do not require H have been put forward. Adler *et al.* [21, 22] proposed the charged defect precursor model, which involves reversible changes in charge or hybridization state of already existing dangling bonds. But this model is ruled out nowadays as no large concentration of charged defects has been found in illuminated a-Si:H. And Pantelides [23] presented a model involving floating bonds, which are fivefold-coordinated Si atoms with an extra nearest neighbor. Finally, saturation occurs either due to one of the following processes:

- simultaneous annealing during generation of defects,
- depletion of the available defects,
- or shunting of the tail-to-tail recombination process by the mono-molecular recombination (recombination through mid-gap states). On the basis of computer

simulations, it was demonstrated that an annealing term in the model was necessary to achieve saturation [24].

Improving stability

In default of understanding fully the causes of the SWE and to be able to prevent the degradation of a-Si:H material, researchers have found ways to reduce degradation and produce solar cells that are less susceptible to the SWE. Their efforts dealt with both material and device improvements. Among the successful paths, we can mention the following ones:

- To grow a-Si:H near the threshold of microcrystallinity by depositing a-Si:H under an excess of hydrogen [25]. In this manner substantial regions of intermediate range order are obtained, leading to a decrease in defect density. Moreover a high hydrogen dilution of the gas mixture etches from the growing surface the strained and weak bonds. However, an issue related to the growth of such material is that it turns microcrystalline with thickness.
- To employ deuterium (D_2 or SiD_4) in place of hydrogen during deposition [26]. The significant improvement in stability obtained is due to the improved medium-range order and the associated lower defect density. Here again the material is deposited at the onset of microcrystalline regime and nanometer size crystals are embedded in the amorphous network.
- To use silicon alloys that are less subject to the SWE, such as Si-Ge alloys [27]. It was suggested that, as a-SiGe:H materials have a lower band gap than a-Si:H, a smaller energy is associated with the electron-hole recombination, which reduces the light-induced defect creation. Moreover, Stutzmann *et al.* indicated [28] that the density of stable dangling bond defects increases with Ge content.
- To reduce the a-Si:H intrinsic layer thickness [5]. A solar cell with a thin intrinsic layer has a stronger internal electric field compared to that of a thick solar cell. Therefore the charge collection before recombination is enhanced. On the other hand, a thicker intrinsic layer absorbs more photons, which leads to an increase of J_{sc}. A compromise between charge collection and photon absorption has to be done in order to minimize the degradation.
- To apply the tandem or triple junction concept [15]. Two or three cells are deposited in a stack and electrically connected in series. In the very thin top cell, mainly the blue part of the spectrum is absorbed and the SWE do not disturb the charge collection. The bottom cell receives only filtered light, so that the SWE is less pronounced. Problems linked to current matching and pinholes (very thin cells) have led to use this concept with silicon alloys (Si-C, Si-Ge) to use the solar spectrum better and to avoid the large thickness variations between the top and the bottom cells. μc-Si is also used as material for the bottom cell.

These methods aim either at enhancing the material stability or at making solar cells less sensitive to ligh-induced degradation. This is achieved by either depositing a-Si:H

on the onset of microcrystallinity, thereby improving the microstructure, or by altering the cell design. In this chapter, the degradation of ETP material grown at high rate is studied. In particular the influence on material stability of deposition conditions where the polysilane radicals and the silicon-ion clusters in the plasma are believed to be reduced, like when hydrogen is injected in the nozzle or when an external rf bias is applied on the substrate, are investigated.

8.3 Experimental details

The degradation experiments were carried out with a white light from a halogen lamp, of 1.5-sun intensity. These conditions are closer to the degradation conditions a solar cell will undergo during use although it gives rise to non-homogeneous generation of carriers in the samples and non-homogeneous defect profiles. The degradation was carried out at a controlled temperature of 50°C. For more details about the degradation set-up, we refer to Chapter 2.

Light soaking on single layers:

The thin films were deposited on Corning glass 1737 under various conditions, as presented in table 8.1. The H_2 flow in the arc was 200 sccm, as well as the silane flow. The silane flow for the rf PE-CVD sample was 40 sccm. The selection of ETP-CVD conditions is as follows:

- sample A represents the standard ETP condition grown at the relatively high growth rate of ~9 Å/s,
- samples B and C are grown at high rate (~ 25 Å/s) and high temperature,
- samples D and E are also grown at high rate (~ 29 Å/s) but from a plasma with additional H_2 injected in the nozzle (H_{2Noz}),
- sample F is deposited with H_{2Noz} and under ion bombardment with an external rf bias on the substrate of 8 W, corresponding to a bias voltage of 24 V.

Finally, sample G is deposited with rf PE-CVD at low growth rate and low substrate temperature as a reference.

The growth rate, the layer thickness and the initial light conductivity, σ_{L0}, are also given in table 8.1. The thickness of the samples was larger than 500 nm to ensure that the light conductivity was determined by the bulk properties and not by the surface. During deposition, 400 sccm He was used as back flow in order to control the substrate temperature accurately. The arc current was set at 40 A, the voltage was between 149 and 161 V and the pressure in the reactor was p_{react} = 0.18-0.23 mbar.

Before degradation, the samples were annealed for 0.5 h at 150°C in order to ensure ohmic contacts and to start the degradation from a stabilized density of state. The samples were then exposed from the top side. The light conductivity, σ_L, was monitored as function of the illumination time, because σ_L is especially sensitive to any

change in the density of deep defect levels and therefore expresses the material changes due to prolonged light exposure.

Sample		Ar (sccm)	$H_{2\ Nozzle}$ (sccm)	Tempera-ture (°C)	Growth rate (Å/s)	Thickness (nm)	σ_{L0} ($\Omega^{-1}.cm^{-1}$)
A	Standard ETP	600	0	250	8.7	523	5.3x10-6
B	High rate ETP	850	0	350	25.4	685	3.4x10-6
C	High rate ETP	850	0	400	24.5	739	3.4x10-6
D	High rate H_{2Noz}	850	200	350	29.3	702	1.5x10-5
E	High rate H_{2Noz}	850	200	400	28.3	734	1.9x10-5
F	rf-biased ETP (8W)	600	150	250	10.3	555	3.2x10-6
G	rf PE-CVD	--	--	200	2.0	724	4.4x10-5

Table 8.1: Deposition conditions and few layer properties of a-Si:H thin films.

Light soaking on solar cells:

The solar cells are p-i-n single junction, deposited on Asahi U-type TCO glass substrate. Table 8.2 gives the nature of the intrinsic layer, as well as its thickness. Four solar cells contain an ETP a-Si:H i-layer, among which E2, E3 and E4 have a thin buffer layer incorporated at the p-i interface:

- cell E1 i-layer is the standard a-Si:H ETP layer ‘A’,
- cell E2 has the i-layer deposited with H_{2Noz} at high growth rate as ‘D’ but at 300°C,
- cell E3 has an rf-biased ETP i-layer ‘F’.
- cell E4 has also an rf-biased ETP i-layer ‘F’ and it has undergone an annealing step after the n-layer deposition (12 min from 200 down to 160°C) and after cell completion (10 min at 150°C). This solar cell has the record efficiency (8%) of the p-i-n solar cells made with an ETP-CVD intrinsic layer.

Finally, cell R1 is entirely deposited with rf PE-CVD. The back contacts are made of an Ag-Al layer and have an area of 0.16 cm^2.

Solar cell	E1	E2	E3	E4	R1
Intrinsic layer	A	D (300°C)	F	F (annealed)	G
i-layer thickness (nm)	420	450	280	280	450

Table 8.2: ETP-CVD and rf PE-CVD solar cells and corresponding intrinsic layer.

The solar cells were exposed from the p-side to white light together with corresponding single layers. The solar cells were degraded under open-circuit conditions at a controlled temperature of 50°C. The solar cell external parameters were monitored as function of the illumination time.

8.4 Results and discussion

8.4.1 Degradation of ETP a-Si:H single layers

The a-Si:H thin films have been exposed to light-soaking up to 10.000 hours, but as the light conductivity, σ_L, was stabilized after ~1000 h, we will present only the evolution of σ_L up to 1100 h for clarity in the graphs.

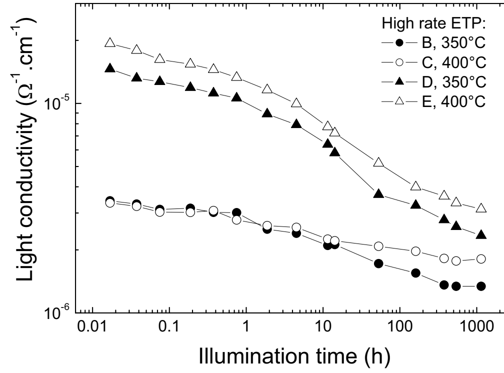

Figure 8.3: Evolution of the light conductivity, σ_L, during light soaking for a-Si:H samples B and C, deposited at 25 Å/s without H_{2Noz} and samples D and E deposited at 29 Å/s with H_{2Noz}. The substrate temperature during material growth is also indicated.

From figure 8.3, we can see that the injection of H_2 in the nozzle, H_{2Noz}, during deposition of high-rate ETP a-Si:H leads to an increase in both initial and stabilized light conductivities. However, the degradation rate is much faster for samples D and E, with H_{2Noz}, than for samples B and C, without H_{2Noz}. Further, we observe that layers deposited at a higher substrate temperature, T_{sub}, have higher stabilized light conductivities. In this case, another degradation pattern is found between samples with and without H_{2Noz}. In the first place, for samples without H_{2Noz} (B and C), it seems that at a T_{sub} = 400°C the σ_L degradation is limited. This behavior suggests that a more structured material is grown at 400°C compared to that at 350°C. Guha *et al.* suggested [25] that the improved properties of a-Si:H are related to the improved medium-range order and the associated lower defect density. However, both samples have a microstructure value, R^*, of 0.25 before illumination. In the second place, for samples with H_{2Noz} (D and E), the degradation rate is identical and does not depend on T_{sub}. The ratio of σ_L(E) / σ_L(D) remains constant throughout the whole range of illumination time. In that case, the R^* value was lowered from 0.28 to 0.20 with T_{sub} increased from 350° to 400°C.

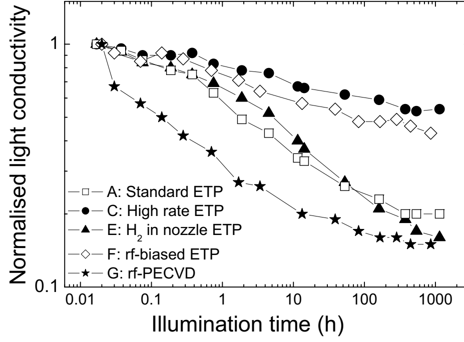

Figure 8.4: Evolution of σ_L, normalized to the annealed state, during light soaking. See table 8.1 for deposition conditions.

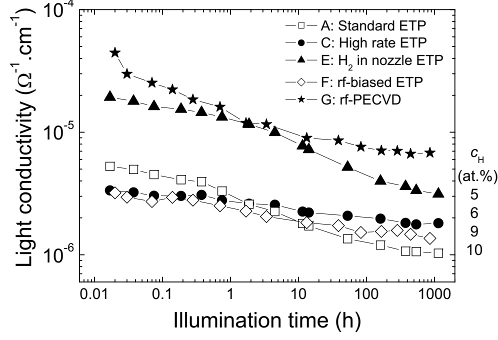

Figure 8.5: Evolution of the light conductivity, σ_L, during light soaking. The initial hydrogen content, c_{H}, of the ETP layers is given.

In figure 8.4, the degradation in σ_L, normalized to the annealed state, is presented. What strikes in figure 8.4 is that the reference sample G, deposited with rf PE-CVD, degrades much faster than any of the ETP-CVD samples and it degrades relatively more. Further it seems that samples C and F follow the same degradation kinetics, which is also the case for samples A and E. The degradation behavior upon exposure to light does not show a correlation with either the deposition rate, the R^* value (which is below 0.5 for all samples), nor the defect density, N_d, of the samples in the annealed state (which is more or less 2×10^{15} cm^{-3} for all samples). It was suggested by Stutzmann *et al.* [14] that samples with higher initial defect density degrade slower than samples with lower N_d, because the creation of new dangling bonds is inhibited by the already existing dangling bonds. This reasoning explains the fact that the SWE is a 'self-limiting' process. In our case, N_d being similar for the different samples, we could expect a similar degradation behavior, but this is not observed.

Considering the evolution of the normalized σ_L, we see that the rf PE-CVD sample degrades relatively more and stabilizes faster than the ETP samples. However, if we examine the absolute value of σ_L, presented in figure 8.5, we observe that although sample G degrades faster, it has a higher stabilized σ_L, which is due to the fact that the initial σ_L is higher than that of the ETP samples. Likewise, sample E, with $H_{2\mathrm{Noz}}$, degrades to a large extent, but it has the highest initial and stabilized σ_L of the ETP sample series. For sample A the lowest light conductivity after degradation was obtained. We remark that this sample was deposited at 250°C, and so was sample F, although the latter was deposited with an external rf bias on the substrate. Finally sample C, high rate and no $H_{2\mathrm{Noz}}$, is the condition under which the SWE is the less pronounced. It is interesting to note that the stabilized σ_L seems to be correlated to

the hydrogen content, c_{H}, of the thin films. The layer containing the highest c_{H} stabilizes at the lowest σ_L of the series and the one with the lowest c_{H} ends up with the highest σ_L of the series (see Fig. 8.5). The rf PE-CVD sample does not follow this trend found for the ETP samples, as the H content is approximately 15 at.% whilst it stabilizes at about $7 \times 10^{-6}\ \Omega^{-1}.\mathrm{cm}^{-1}$, which is higher than the stabilized ETP samples σ_L.

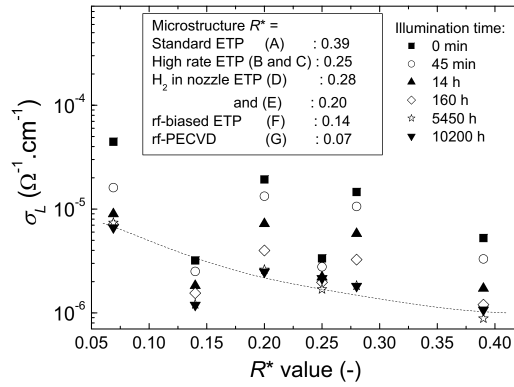

Figure 8.6: Variation of σ_L versus microstructure as a function of illumination time and sample deposition conditions. The line is a guide to the eye. The microstructure of the a-Si:H layers is indicated in the inset.

The variation of σ_L as a result of increasing light-soaking time versus the R^* value is presented in figure 8.6. The sample deposition conditions related to each R^* value are indicated in the inset. We observe that the samples B and C with $R^* = 0.25$, which degraded less upon light soaking, have a quite low initial light conductivity, σ_{L0}, compared to the other ETP samples. However, the stabilized σ_L follows the trend line of the stabilized σ_L of the other samples. This behavior seems to indicate that first of all, the stabilized σ_L of an a-Si:H layer is depending on its microstructure (as suggested by the line in figure 8.6) and secondly, if the material is highly defective in the initial state, due e.g. to the non-optimum deposition conditions, it will degrade less. Sample F deposited by rf-biased ETP-CVD is not in line with the other data points, as its σ_{L0} is rather low ($3.2 \times 10^{-6}\ \Omega^{-1}.\mathrm{cm}^{-1}$), but in spite of that, the associated R^* value, equal to 0.14, is not large. We think that the light conductivity is limited by the electron mobility (which was found, by time-of-flight, to be lower in those samples than in rf PE-CVD a-Si:H samples, as mentioned in chapter 5). Subsequently, σ_{L0} and stabilized σ_L are relatively low and they are not in line with the other ETP samples. It appears that the degradation process involves more than the hydrogen content and repartition in the material.

8.4.2 Degradation of solar cells with an ETP intrinsic layer

In order to investigate the degradation behavior of ETP-CVD material in a device, solar cells in which ETP intrinsic material was implemented, were exposed to illumination from a halogen lamp for more than 1000 hours. The evolution of the standard ETP solar cell (E1) fill factor, *FF*, upon prolonged illumination is presented in figure 8.7. The changes in open-circuit voltage, V_{oc}, and in short-circuit current, J_{sc}, are far less prominent than that in *FF*. Therefore the evolution of the *FF* is used to quantify the degradation behavior of the solar cells. The *FF* follows an S-shape curve, but after 5000 h of light soaking, it drops very quickly instead of stabilizing. This second drop of *FF* is in fact due to the degradation of the metal contacts as the solar cell was not encapsulated for the experiment. Pinholes, either caused by the Ag-Al layer deterioration or by the needle during measurements, have been observed in the metal layers. The *FF* decay as a function of illumination time can be fitted with a stretched exponential, as shown in figure 8.7. Street has shown [10] that such a function can describe the relaxation of the light-induced defect density, which in turn was related to the *FF* [24]. The time dependence of the *FF* follows the relation:

$$FF = \left(FF_0 - P_1\right) * \exp\left[-\left(t/P_2\right)^{P_3}\right] + P_1 \tag{3}$$

with FF_0 the initial *FF*, P_1, P_2 and P_3 the fitting parameters among which P_1 is the estimated value of the stabilised *FF*.

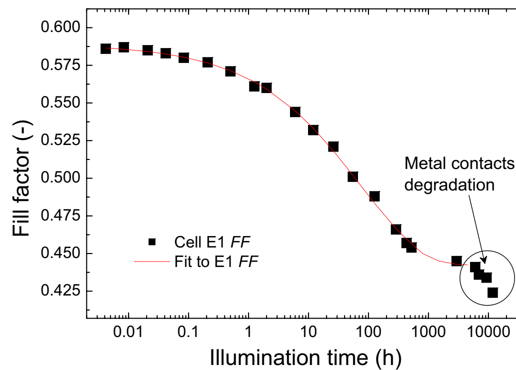

Figure 8.7: Evolution of cell E1 fill factor upon light soaking. The line is a stretched exponential fit to the *FF*.

We obtain a sub linear dependence of the *FF* on the illumination time. The estimated value of the *FF* degradation from the stretched exponential fit is found to be 24.4%, whereas the experimental value was 27.3%. However, if we do not consider the last few points, because this further degradation of the *FF* is due to the deterioration of the contacts, the *FF* decay becomes 23.7%, which is in good

agreement with the fitted results. It is then concluded that it is not possible to distinguish between metal contact degradation and solar cell degradation for illumination time longer than 2000 hours. Therefore we will limit our study to these 2000 hours.

In figure 8.8, the *J-V* characteristic of cell E1 is presented after various stages of light soaking. After 2 days of exposure, V_{oc} decreased and J_{sc} remained virtually unchanged. After 20 days, J_{sc} has significantly decreased, as well as the *FF*. Further exposure beyond 20 days does not reduce further the external parameters significantly and we conclude that solar cell E1 has then reached its stabilized state.

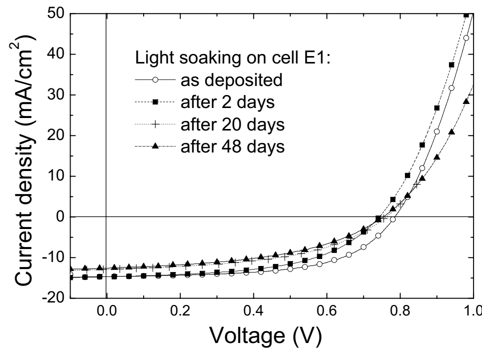

Figure 8.8: *J-V* characteristics of solar cell E1 (ETP-CVD at 250°C and 8.9 Å/s) during light soaking.

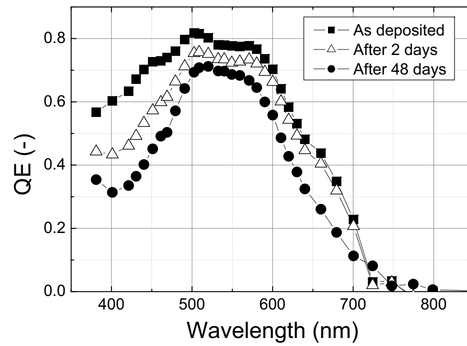

Figure 8.9: Quantum efficiency at 0 V bias of solar cell E1 (ETP-CVD at 250°C and 8.9 Å/s) during light soaking.

In figure 8.9, the variation of cell E1 quantum efficiency, taken at zero bias voltage, is shown. It is interesting to compare the QE at 0 V bias to study changes in the cell. It appears that the response, after two days exposure, is mainly reduced in the blue part of the spectrum. Therefore we believe that at first, the degradation mainly affects the upper part of the solar cell, and in particular near the p-i interface, where the photon absorption is the highest. After 48 days of light soaking, the spectral response is reduced for all wavelengths, meaning that the carrier collection from deep in the cell is also limited. Following these results, we think that after prolonged light soaking, degradation mainly occurs in the bulk of the intrinsic material in accordance with Munyeme *et al.* [29], who found that then the interface related degradation is reduced and the bulk degradation becomes dominant. Moreover, Hack *et al.* [30] showed that bulk recombination was related to the reduction of the carrier diffusion length and the carrier lifetime.

In figure 8.10 the evolution of the external parameters of the solar cells towards light soaking is presented. Figure 8.10 (a) shows the *FF* during light exposure. As a reference, the *FF* light-soaking behavior of a solar cell made entirely by rf PE-CVD (R1) is also presented. First of all, we observe that three ETP solar cells (E1, E3 and

E4) have a similar degradation behavior as the rf PE-CVD cell. However, this is not the case for E2, the cell with the i-layer deposited at very high growth rate (29 Å/s) and higher substrate temperature (300°C).

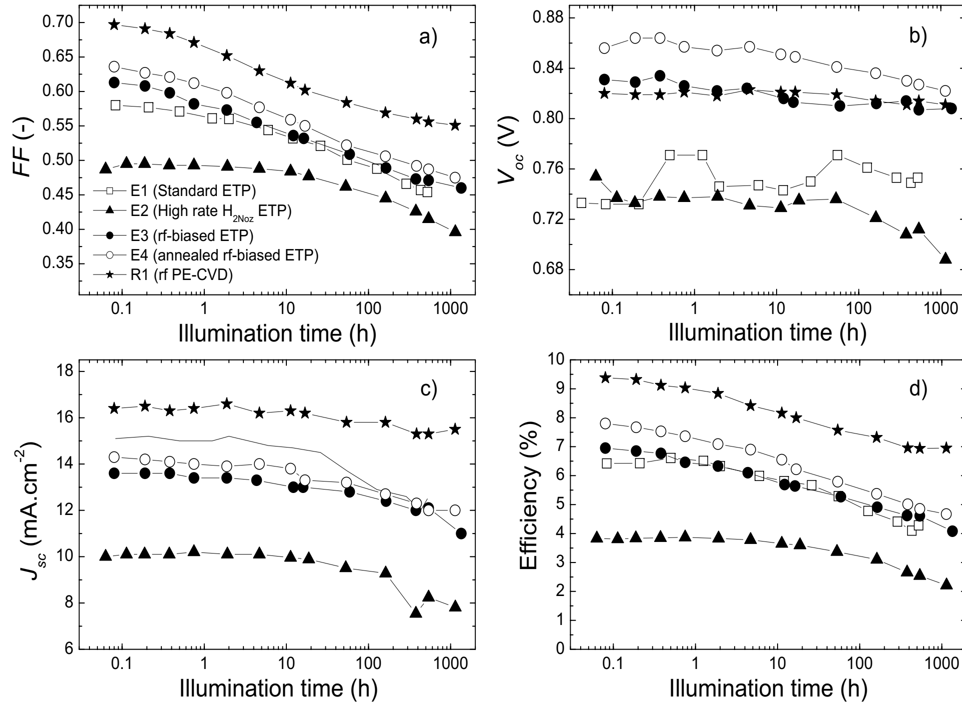

Figure 8.10: Evolution in time of the external parameters of ETP solar cells during light soaking. (a) Fill factor, (b) open-circuit voltage, (c) short-circuit current and (d) efficiency.

In the beginning this cell seems not to degrade at all and the *FF* even increases slightly. However, the initial *FF* was rather low and after approximately 10 hours, it starts to drop quite quickly. We have to note that the i-layer in this solar cell has a high microstructure value, $R^* = 0.43$, compared to the other i-layers. This result corroborates the idea that light-induced defect creation depends on the initial quality of the intrinsic layer and that samples with higher initial defect density degrade slower [14]. Beside that, we observe that an external rf bias on the substrate during ETP-CVD (cell E3) and annealing after deposition of the active layers (cell E4) improves the cell performance, but the *FF* of these cells remains low compared to that of a cell deposited five times slower by standard rf PE-CVD (R1, 2 Å/s). Moreover, we can see that although cell E3 degrades faster than cell E1 (standard ETP i-layer), the initial and stabilized *FF* are higher. The improvement in stabilised *FF* might be related to the lower density of nano-sized voids in the material, due to ion-bombardment, as

concluded from lower R^* values (R^*(E1) = 0.39, whereas R^*(E3) = 0.14). Cell E4 shows the highest initial and final *FF* obtained for the ETP cells. We note, however, that the *FF* variation of the ETP solar cells as a function of light-soaking time do not always show a clear sign of stabilization.

The V_{oc} evolution upon the illumination time is plotted in figure 8.10 (b). The ETP solar cells have their V_{oc} decreased due to the light soaking. This behavior seems to be characteristic of ETP cells, but not of rf PE-CVD cells. V_{oc} of R1 remains virtually constant after up to thousand hours of illumination. We note that E1, deposited at low growth rate and low T_{sub}, has its V_{oc} increased.

The short-circuit current density of the illuminated cells is given in figure 8.10 (c). J_{sc} is almost constant throughout the experiment and, for ETP solar cells, it starts to diminish after 100 hours of light soaking. Figure 8.10 (d) shows the evolution of the cell efficiencies. After more than 1000 hours light exposure, the record cell E4 has an efficiency of 4.7%, which represents a higher degradation (39%) than the rf PE-CVD cell R1 (30%), but a somewhat lower degradation compared to both the high rate ETP cell E2 (42%), the conventional ETP cell E1 (41%) or the rf-biased ETP-CVD cell E3 (40%). This implies that the degradation is apparently more or less similar for all ETP cells.

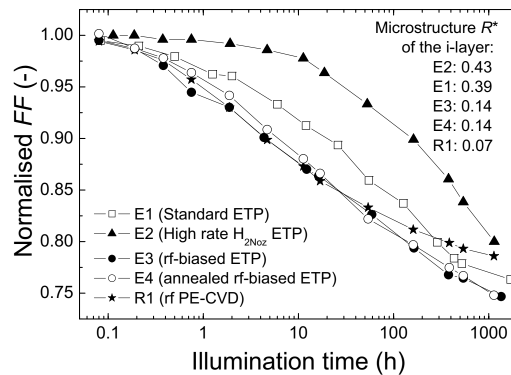

Figure 8.11: Degradation kinetics of solar cells with different intrinsic layer.

The normalized *FF* of the solar cells is presented in figure 8.11. From this figure it is clear that the ETP solar cells follow different degradation kinetics depending on the i-layer deposition conditions and cell E2 displays the longest period before the onset of degradation. Furthermore, it does not show stabilization after 1000 hours exposure to light. Cells E3 and E4, deposited under additional ion bombardment, present the same pattern as cell R1, at least concerning the 50 first hours of the experiment. They degrade further than cell R1, but stabilize after 2000 h. Finally, cell E1 has a degradation behavior in between that of cell E2 and cell E3. It is interesting to note that the *FF* degradation onset is correlated to the microstructure parameter R^* of the

intrinsic layers: the higher the R^* of the i-layer is, the later the *FF* starts to drop. The i-layer R^* values are indicated in figure 8.11. Moreover a lower R^* value leads to higher initial and stabilized *FF*, as pointed out by Guha *et al.* [31], who found that increasing microvoid density and microstructure leads to the decrease of both initial and light-degraded solar cell performance. The stabilized *FF* of cells E3 and E4 is higher than that of cells E1 and E2, but so was already the initial *FF* (see Fig. 8.10 (a) and 8.10 (d)). Finally we can note that the *FF* degradation pattern does not correlate to that of the corresponding single-layer light conductivity.

In conclusion it appears that conditions under which powder formation is restrained, like by introducing hydrogen in the nozzle and applying an external rf bias in the substrate (see chapters 4 and 5), lead to a degradation behavior of the ETP solar cells similar to that of an rf PE-CVD solar cell. However, the ETP cells degrade relatively more than their rf PE-CVD counterparts. Further effort should concentrate on the improvement of the stabilized efficiency of the ETP cells and for that purpose the influence of carrier mobility on both material properties and solar cell performance should be investigated.

The SWE can be reversed by carrying out a thermal annealing treatment in the dark at temperatures above 150°C. However in our case, the metal contacts of the cells presented here were deteriorated and it was not possible to evaluate the degree of recovery of the solar cells after annealing. However, we did observe improvement of all external parameters of a solar cell that was not degraded but kept as-deposited in the dark at room temperature (see table 8.3). In eight months, the cell with an ETP i-layer deposited at 9 Å/s and 250°C self-annealed and hence has its efficiency improved by 16% from 6 to 7%.

Date of measurement	V_{oc} (V)	J_{sc} (mA/cm^2)	*FF* (-)	η (%)
April 2003	0.737	14.6	0.559	6.01
September 2003	0.761	14.9	0.581	6.58
December 2003	0.789	15.2	0.582	6.97

Table 8.3: Self-annealing of an ETP cell preserved in the dark at room temperature.

8.5 Conclusions

In this chapter, the degradation of ETP a-Si:H thin films and single junction solar cells upon prolonged light exposure were presented. First of all, the effect of light-induced defects in single layers was studied by following the evolution of the light conductivity. We found that the plasma chemistry plays an important role in the degradation kinetics of a-Si:H, and layers deposited with additional hydrogen in the nozzle degrade faster than their H_{2Noz}-less counterpart. However, both their initial and stabilized light conductivities are enhanced. Material deposited at a higher

substrate temperature is less sensitive to the SWE. Ion bombardment during film growth does not reduce material degradation, but the films were deposited at a substrate temperature of 250°C. None of the ETP deposition conditions has a degradation behavior similar to that of rf PE-CVD, which degrades very fast. It seems that a material with low initial defect density and higher medium-range order degrades faster than a more disordered material. As a matter of fact the creation of new dangling bonds is thought to be inhibited by the preexisting dangling bonds. Finally, the microstructure and the total hydrogen content of the ETP material seems to correlate with the stabilized light conductivity, a lower R^* and c_H leading to a higher stabilized σ_L.

Secondly, the SWE on solar cells was studied by monitoring the external parameters and the quantum efficiency as a function of light-soaking time. Quantum-efficiency results show that degradation occurs first at the p-i interface, where most of the photons are absorbed and hence, where recombination is highest. After prolonged illumination, degradation takes place mainly in the bulk of the intrinsic layer, due to a reduction of the internal electric field. Comparing the degradation of several solar cells with an ETP i-layer to that of a rf PE-CVD solar cell, it was observed that the ETP cells are more sensitive to the SWE and stabilize to a relatively lower *FF* and efficiency than an rf PE-CVD cell. However, applying an rf bias on the substrate during ETP a-Si:H growth, and annealing the solar cell before metallization, leads to an increase in stabilized efficiency. Finally, the R^* value influences the period before the onset of degradation, but not the final performance of the solar cell. In order to improve the stabilized efficiency of ETP solar cells deposited at high deposition rates and high substrate temperature, more knowledge about carrier mobility and diffusion length should be acquired and the evolution of these parameters upon light exposure should be studied.

References

[1] D.L. Staebler and C.R. Wronski, Appl. Phys. Lett. **31** (1977) 292
[2] H. Dersch, J. Stuke and J. Beichler, Appl. Phys. Lett. **38** (1980) 456
[3] M. Stutzmann, M.C. Rossi and M.S. Brandt, Phys. Rev. B **50** (1994) 11592
[4] M. Stutzmann, Mat. Res. Soc. Symp. Proc. Vol. **467** (1997) 37
[5] H. Fritzsche, Annu. Rev. Mater. Res. **31** (2001) 47
[6] U. Schneider, B. Schröder and F. Finger, J. Non-Cryst. Solids **114** (1989) 633
[7] W. den Boer, M.J. Geerts, M. Ondris and H.M. Wentinck, J. Non-Cyst. Solids **66** (1984) 363
[8] D.L. Staebler and C.R. Wronski, J. Appl. Phys. **51** (1980) 3262
[9] V. Nádazdy and M. Zeman, Phys. Rev. B **69** (2004) 165213

[10] R.A. Street, *Hydrogenated amorphous silicon*, Cambridge Solid State Science Series, Cambridge University Press (1991) pg 203
[11] T. Gotoh, S. Nonomura, M. Nishio, N. Masui, S. Nitta, M. Kondo and A. Matsuda, J. Non-Cryst. Solids **227** (1998) 263
[12] E. Spanakis, E. Stratakis, P. Tzanetakis and Q. Wang, J. Appl. Phys. **89** (2001) 4294
[13] S. Nonomura, N. Yoshida, T. Gotoh, T. Sakamoto, M. Kondo, A. Matsuda and S. Nitta, J. Non-Cryst. Solids **266** (2000) 474
[14] M. Stutzmann, W.B. Jackson and C.C. Tsai, Phys. Rev. B **32** (1985) 23
[15] Y. Ichikawa, S. Fujikake, T. Takayama, S. Saito, H. Ota, T. Yoshida, T. Ihara and H. Sakai, 23rd IEEE Photovolatic Specialists Conference (1993) 27
[16] S. Yamasaki, T. Umeda, J. Isoya, A. Matsuda and K. Tanaka, Mater. Res. Soc. Proc. **420** (1996) 587
[17] R.S. Crandall, D.E. Carlson, A. Catalano and H.A. Weakliem, Appl. Phys. Lett. **44** (1984) 200
[18] H.M. Branz, Phys. Rev. B **59** (1999) 5498
[19] H.M. Branz, J. Non-Cryst. Solids **266** (2000) 391
[20] V.L. Dalal, T. Maxson, K. Han and S. Haroon, J. Non-Cryst. Solids **227** (1998) 1257
[21] D. Adler, M.E. Eberhart, K.H. Johnson, and S.A. Zygmunt, J. Non-Cryst. Solids **66** (1984) 273
[22] D. Adler, Solar Cells **9** (1983) 133
[23] S.T. Pantelides, Solid State Comm. **84** (1992) 221
[24] G. Munyeme, Ph.D. thesis, Utrecht University (2003)
[25] S. Guha, J. Yang, D.L. Williamson, Y. Lubianiker, J.D. Cohen and A.H. Mahan, Appl. Phys. Lett. **74** (1999) 1860
[26] S. Sugiyama, J. Yang and S. Guha, App. Phys. Lett. **70** (1997) 378
[27] G. Nakamura, K. Sato and Y.Yukimoto, Solar Cells **9** (1983) 75
[28] M. Stutzmann, R.A. Street, C.C. Tsai, J.B. Boyce and S.E. Ready, J. Appl. Phys. **66** (1989) 569
[29] G. Munyeme, M. Zeman, R.E.I. Schropp and W.F. van der Weg, Phys. Stat. Sol. C **1** (2004) 2298
[30] M. Hack and M. Shur, J. Appl. Phys. **58** (1985) 1656
[31] S. Guha, J. Yang, S.J. Jones, Y. Chen and D.L. Williamson, Appl. Phys. Lett. **61** (1992) 1444

Chapter 9

General conclusions

In this thesis some issues concerning a-Si:H thin films grown by expanding thermal plasma chemical vapor deposition (ETP-CVD) and the relation between plasma conditions, material properties and solar cell performance are addressed. The two first chapters give a short introduction to the a-Si:H material, the ETP deposition set-up and the methods used to characterise the a-Si:H layers and the solar cells. In Chapter 3 the reproducibility of a-Si:H layers grown with the ETP technique is investigated as a function of the pressure in the arc, the plasma source, as well as the voltage across the arc. The temperature control of the substrate and thus of the growing surface is crucial for the reproducibility of the layers. Therefore a He back flow is used to bring the substrate at the desired temperature. A variation of less than 5% is found for the ETP a-Si:H layer properties, such as growth rate and mass density, whereas the variation in the Urbach energy is less than 6%.

Polysilane radicals and silicon cluster ions, large silicon-related species present in the plasma, affect negatively the properties of the grown layers for solar-cell application and in order to minimize their growth contribution, two routes are considered.

The first approach is discussed in Chapter 4 and aims at reducing the ion density (mainly Ar^+ ions) emanating from the arc by injecting hydrogen directly in the reactor chamber via the nozzle, in addition to H_2 flow in the arc. We found that the growth rate is increased compared to material grown without H_2 in the nozzle (up to 60 Å/s

in this study), partly due to an increase in reactor pressure and reduction of the ETP beam diameter, but also due to the formation of extra radicals in the plasma. It appears that the light conductivity, and thus the defect density, is strongly correlated to the microstructure of the material, R^*. We think that a-Si:H containing a high content of high-stretching mode configurations is less conductive due to defects, which operate as recombination centers, on the surface of nano-voids incorporated in the material. By studying the hydrogen bonding type in a-Si:H, it turns out that the transition between vacancy- and void-dominated a-Si:H can be monitored with R^*. For moderate reactor pressures ($\leq$ 0.21 mbar) this transition is observed for a critical c_H of 14 at.%. This critical c_H shifts to lower values when higher reactor pressures are used.

In the second approach, discussed in Chapter 5, rf bias is applied to the substrate during ETP-CVD, leading to ion bombardment of the surface. As a result of this ion bombardment the polysilanes and cluster ions are broken up in smaller particles and/ or their surface mobility is increased. In the latter case, the adsorbed particles can diffuse better to a favourable growth site. Two effects are competing: surface-mobility enhancement, dominant at low power, and atom sputtering from the film surface, dominant at high power. For solar-cell application, the first-mentioned effect is considered as beneficial, whereas the latter seems to have deleterious consequences. The application of a mild bias (~20-30 V) improves the film density, the bonding configuration of hydrogen to silicon atoms and reduces the incorporation of defects. As a result, the substrate temperature can be reduced by about 50°C while keeping the same material properties.

An issue related to the growth of high-rate a-Si:H is the high substrate temperature ($\geq$ 300°C) that is needed to obtain solar-grade material. When those layers are integrated in a p-i-n solar cell, the p-layer properties can deteriorate because of the high temperature. In Chapter 6 we discuss the incorporation of microcrystalline silicon p-doped (p-μc-Si:H) thin film in solar cells. These films combine heat resistance, high conductivity and low absorption, making them a suitable candidate as window layer in high-rate ETP solar cells. However, when incorporated in a solar cell with the i-layer deposited at 3.3 nm/s and 400°C, it appears that the transparent conductive oxide used as front contact (SnO_2:F) is reduced during the p-μc-Si:H layer deposition by exposure to H_2 plasma. Therefore no improvement in the performance of the solar cell is observed with a microcrystalline Si layer compared to an amorphous one. To prevent that effect, a thin ZnO layer should be applied on the SnO_2:F, and a buffer layer should be introduced at the p-i interface.

In Chapter 7 the effect of such a buffer layer at the p-i interface on the performance of a-Si:H solar cells was investigated in cells with an a-SiC:H p-layer. The experimental and simulation results show that initial device performance is enhanced with a hydrogen-diluted a-Si:H layer of 10-nm thick. With a strong internal electric field, the charge carriers are swept away from the interface region faster than when no buffer layer is applied and the carrier-recombination probability is then reduced. Moreover,

the initial layer grown with ETP-CVD, the so-called defect-rich layer, is moved away from the region where most charge carriers are generated. Finally, thermal damage of the p-layer, due to the high substrate temperature during deposition of the ETP i-layer, is diminished. Ion bombardment as a result of rf biasing during high rate a-Si:H deposition at moderate substrate temperature ($\geq$ 10 Å/s and 250°C) gives rise to a-Si:H with lower defect density, improved microstructure and opto-electronic properties. The solar-cell performance is also improved. Furthermore, a double annealing treatment permits to re-equilibrate the density of states deep in the intrinsic ETP layer of the p-i-n cell and thus the carrier collection improves. With the above-mentioned rf biased ETP a-Si:H i-layer and an optimized cell structure we obtained a record single junction ETP solar cell: without highly reflective back contact, initial efficiencies of 8.0% have been achieved.

The effect of light-induced defects in single layers and in solar cells was studied in Chapter 8 by following the evolution of the light conductivity and the external cell parameters, respectively. Additional hydrogen in the nozzle enhances initial and stabilized light conductivities, so does a higher substrate temperature. Ion bombardment during film growth at 250°C does not reduce material degradation. It seems that a material with low initial defect density and higher medium-range order degrades faster than a more disordered material. As a matter of fact the creation of new dangling bonds is thought to be inhibited by the already existing dangling bonds. Concerning the light-induced degradation of solar cells, it appears that first the p-i interface is deteriorated, where most of the photons are absorbed, hence where recombination is highest. After prolonged illumination, degradation takes mainly place in the bulk of the intrinsic layer. The R^* value influences the period before degradation onset, but not the final performance of the solar cell. ETP solar cells are more sensitive to the Staebler-Wronski effect and stabilize to a somewhat lower *FF* and efficiency than an rf PE-CVD cell. However, applying an rf bias on the substrate during ETP a-Si:H growth and annealing the solar cell before metallization lead to an increase in stabilized efficiency.

Finally, the results show that the expanding thermal plasma CVD technique is suitable for the deposition of hydrogenated amorphous silicon at high growth rates and these layers can be successfully integrated into solar cells. So far, the record conversion efficiency obtained with this technique and a single junction a-Si:H solar cell is similar to that obtained with other thin film deposition methods. In order to increase the performance of the ETP solar cells further, we recommend the following:

- To investigate the carrier lifetime-mobility as a function of the deposition parameters, to understand the limited light conductivity with rf-biasing (it was shown by Time-Of-Flight that, although holes have a higher mobility in ETP-CVD material than in rf PE-CVD a-Si:H, the electron mobility is lower [*Brinza, Ph.D. thesis, Catholic University of Leuven, Belgium (2004)*].)

- To control the ion energy better during rf-biased ETP-CVD, by applying, i.e., a modulated signal.
- To develop tandem or even triple junction cells, to enhance stabilized cell efficiency and reduce the SWE.

Summary

Title: **Expanding Thermal Plasma Deposition of Hydrogenated Amorphous Silicon for Solar Cells**

by: Agnès Petit

At this time a breakthrough on the energy market of electricity generated by solar cells depends on the cost reduction of the module production process. In that view, thin-film solar cells are promising devices because of the possibility to use inexpensive material, like hydrogenated amorphous silicon (a-Si:H) and relatively well-known fabrication techniques for the photovoltaic part of the cells based on chemical vapor deposition (CVD). However, the growth rate of the semiconductor thin layer remains one of the issues affecting the costs. With expanding thermal plasma (ETP) CVD high deposition rates (up to 100 Å/s) have been achieved and material with good properties was obtained. In order to implement this high-rate material successfully into solar cells, more insight into the a-Si:H properties depending on the plasma conditions is required. In this thesis, the a-Si:H film properties deposited by ETP-CVD are studied, as well as a-Si:H single junction solar cells containing an ETP intrinsic layer.

Under the conditions studied, silane (SiH_4) is mainly dissociated by hydrogen atoms present in the reactor, resulting in a domination of silyl (SiH_3) radicals as growth precursors of a-Si:H. However, large silicon-containing species, such as polysilane and cluster ions, are present in the plasma as well, especially at high reactor pressures. The work described in this thesis aims to gain a better understanding of the relation between plasma conditions and a-Si:H material properties, and the performance of the related single junction solar cells. The bonding configuration of hydrogen in a-Si:H, determined by infrared spectroscopy, is found to have an important role in the material properties. It was demonstrated before that the a-Si:H structure can be divided into two distinct regions in the hydrogen concentration: one region for low hydrogen concentration which is dominated by vacancies and one region for high hydrogen concentration which is dominated by voids. Moreover, the incorporation of vacancies and voids in the film depends on growth rate and substrate temperature. In this thesis it is shown that also the reactor pressure in addition to the growth rate and substrate

temperature determines the transition between the vacancy- and void-dominated regions. The results suggest that dust formation, or large-particle generation in the plasma, is the underlying principle of this dependence of optimal material properties on reactor pressure. It is demonstrated that the critical hydrogen content, at which the transition between the vacancy- and void-dominated regions is found, is lowered for higher reactor pressure. The light conductivity and defect density show a relation with the a-Si:H network structure. Furthermore, the high substrate temperature needed to obtain optimal material properties for deposition rates larger than 10 Å/s is an issue for the fabrication of p-i-n solar cells as it induces deterioration of the underlying layers. The effect of hydrogen injected in the nozzle and that of an rf bias applied on the substrate on material properties are discussed in this thesis. Because of the remote generation of the ETP plasma, no significant ion bombardment occurs on the surface. The addition of a mild rf bias on the substrate entails an improvement in film density and a reduction in defect incorporation. It is found that the substrate temperature can be reduced while keeping the same material properties.

Finally, the feasibility of making a working single junction solar cell, with as intrinsic layer a high rate ETP layer, is addressed. The performance of solar cells does not depend only on the material properties of each individual layer that forms the cell, but also on the device structure and post-treatment. In this thesis it is demonstrated that a 10-nm thick buffer layer, situated at the p-i interface, enhances the fill factor and the open-circuit voltage. The results indicate that a H-diluted buffer layer protects the p-layer from thermal damage and ensures a low defect density at the p-i interface where most of the carriers are generated. An annealing treatment of the cell before metallization improves the cell performance further, although the stabilised efficiency is not significantly improved. With these conditions, a record single junction a-Si:H solar cell, with the intrinsic layer prepared with the ETP technique at 11 Å/s and at 250°C, has been obtained: the initial efficiency was 8.0%, which stabilised at 4.7% after 1100 h illumination.

Samenvatting

Titel: Depositie van Zonnecellen van Amorf Silicium met behulp van Expanderend Thermisch Plasma

Door: Agnès Petit

Op dit moment hangt een doorbraak op de energiemarkt van elektriciteitsopwekking met zonnecellen af van de kostenverlaging van het productieproces van modules. Vanuit dit oogpunt zijn dunne-film zonnecellen veelbelovende devices, omdat het mogelijk is om goedkope materialen, zoals amorf silicium (a-Si:H), te gebruiken en relatief bekende fabricagetechnieken toe te passen die gebaseerd zijn op chemisch opdampen (*chemical vapor deposition*, CVD), voor het maken van het fotovoltaïsche deel van de cel. De groeisnelheid van de halfgeleidende dunne lagen blijft echter één van de belangrijke onderwerpen die de kosten beïnvloeden. Met expanderend thermische plasma (ETP) CVD zijn hoge groeisnelheden (tot 100 Å/s) gehaald en is materiaal met goede eigenschappen verkregen. Om dit materiaal dat bij hoge groeisnelheden is verkregen in zonnecellen te implementeren, is meer inzicht nodig hoe de eigenschappen van a-Si:H afhangen van de plasma-omstandigheden. In dit proefschrift worden de eigenschappen van dunne lagen van a-Si:H bestudeerd die gegroeid zijn met ETP-CVD, alsook enkelvoudige junctie zonnecellen van a-Si:H waarin een intrinsieke laag is opgenomen die gemaakt is met ETP-CVD.

In de bestudeerde groei-omstandigheden wordt silaan (SiH_4) voornamelijk gedissocieerd door waterstofatomen die in de reactor aanwezig zijn, wat leidt tot een groeiproces van a-Si:H dat gedomineerd wordt door SiH_3 radicalen. Grote silicium-bevattende deeltjes, zoals polysilanen en clusterionen, zijn echter ook aanwezig in het plasma, in het bijzonder bij een hoge reactordruk. Het doel van het werk dat in dit proefschrift is beschreven, is een beter begrip te verkrijgen van de relatie tussen de plasma-omstandigheden enerzijds, en de materiaaleigenschappen van a-Si:H en de prestatie van enkelvoudige junctie zonnecellen anderzijds. We hebben gevonden dat bindingsconfiguraties van waterstof in a-Si:H, bepaald met behulp van infrarood spectroscopie, een belangrijke invloed hebben op de materiaaleigenschappen. Eerder is aangetoond dat op basis van de waterstofconcentratie de structuur van a-Si:H

verdeeld kan worden in twee aparte regios: een regio voor lage waterstofconcentraties waarin de structuur bepaald wordt door vacante plaatsen (*vacancies*) in het silicium netwerk en een regio voor hoge waterstofconcentraties waarin de structuur bepaald wordt door gaten (*voids*) in het materiaal. Het is gebleken dat het inbouwen van deze vacante plaatsen en gaten in het materiaal bepaald wordt door de groeisnelheid en de substraattemperatuur. Uit de resultaten die gepresenteerd zijn in dit proefschrift blijkt dat ook de reactordruk een belangrijke parameter is. Er wordt aangetoond dat de kritische waterstofconcentratie waar de overgang plaatsvindt van de ene naar de andere regio, lager is naarmate de reactordruk hoger wordt. De lichtgeleiding en de defectdichtheid laten een relatie zien met de structuur van het a-Si:H netwerk. Verder blijkt dat de hoge substraattemperatuur die nodig is om optimale materiaal-eigenschappen te verkrijgen voor groeisnelheden hoger dan 10 Å/s een onderwerp van discussie is voor het maken van p-i-n zonnecellen, omdat de eigenschappen van de onderliggende lagen hierdoor verslechteren. Het effect van waterstof dat via de uitstroomopening in het plasma wordt geïnjecteerd en het effect van een rf spanning die op het substraat wordt aangelegd op de materiaaleigenschappen wordt bediscussieerd in dit proefschrift. Omdat de plaats waar het plasma gecreëerd wordt niet in direct contact staat met het substraat, vindt er geen ionenbombardement plaats op het oppervlak van de groeiende laag. Het aanleggen van een beperkte rf spanning op het substraat leidt tot een verbetering van de dichtheid van de laag en een verlaging van de defectdichtheid. Het blijkt dat met het aanleggen van een rf spanning op het substraat de substraattemperatuur verlaagd kan worden met behoud van de materiaaleigenschappen.

Als laatste is de haalbaarheid onderzocht om een werkende enkelvoudige junctie zonnecel te maken waarin een intrinsieke laag van a-Si:H is ingebouwd die gemaakt is met ETP-CVD. De prestatie van de zonnecellen hangt niet alleen af van de materiaaleigenschappen van de individuele lagen van de cel, maar ook van de devicestructuur en de processtappen na de depositie van de cel. In dit proefschrift wordt aangetoond dat een bufferlaag met een dikte van 10 nm tussen de p- en i-laag de vulfactor en de open-klemspanning vergroot. De resultaten laten zien dat een bufferlaag die gegroeid is gebruikmakend van een sterke waterstofverdunning van het plasma, de p-laag beschermt tegen nadelige effecten van de hoge temperatuur die nodig is voor de ETP i-laag. Verder zorgt deze laag ervoor dat de defectdichtheid laag is bij de p-i overgang waar de meeste ladingsdragers worden gegenereerd. Een warmtebehandeling van de cel voordat het metalen achtercontact wordt opgedampt, verbetert het initiële rendement van de cel nog meer, al heeft het nauwelijks een significant effect op het gestabiliseerde rendement. Op deze manier is een enkelvoudige junctie zonnecel van a-Si:H gemaakt met een record rendement, waarvan de intrinsieke laag gegroeid is met ETP-CVD bij een groeisnelheid van 11 Å/s en een substraattemperatuur van 250°C: het initiële rendement was 8.0%, welke stabiliseerde op 4.7% na 1100 uur belichting.

List of publications related to this work

Improvement of expanding thermal plasma amorphous silicon solar cell by means of substrate rf-biasing
A.M.H.N. Petit, V. Nádazdy, A.H.M. Smets, M. Zeman, M.C.M. van de Sanden and R.A.C.M.M. van Swaaij, 20th European Photovoltaic Solar Energy Conf. and Exhib., Barcelona, Spain (2005) 1616

On the reproducibility of a-Si:H deposited with an expanding thermal plasma
A.M.H.N. Petit, A.H.M. Smets, R.A.C.M.M. van Swaaij and M.C.M. van de Sanden, Proc. SAFE Conf., Veldhoven, the Netherlands (2004) 714

Hydrogen injection in ETP plasma jet for fast-deposition of high-quality a-Si:H
A.M.H.N. Petit, R.A.C.M.M. van Swaaij and M.C.M. van de Sanden, Mater. Res. Soc. Symp. Proc. **808** (2004) 359

Simualtions of buffer layers in a-Si :H thin film solar cells deposited with an expanding thermal plasma
A.M.H.N. Petit, M. Zeman, R.A.C.M.M. van Swaaij and M.C.M. van de Sanden, Mater. Res. Soc. Symp. Proc. **762** (2003) 369

High temperature CVD deposition of thin polycrystalline silicon layers
A.M.H.N. Petit and M. Zeman, Proc. SAFE Conf., Veldhoven, the Netherlands (2001) 150

Integration of expanding thermal plasma deposited hydrogenated amorphous silicon in solar cells
B.A. Korevaar, C. Smit, A.M.H.N. Petit, R.A.C.M.M. van Swaaij and M.C.M. van de Sanden, Mater. Res. Soc. Symp. Proc. **715** (2002) 595

Effect of buffer layers on p-i-n a-Si:H solar cells deposited at high rate utilizing an expanding thermal plasma
B.A. Korevaar, A.M.H.N. Petit, C. Smit, R.A.C.M.M. van Swaaij and M.C.M. van de Sanden, 29th IEEE Photovoltaic Spec. Conf., New Orleans, Louisiana (2002) 1230

High-rate microcrystalline silicon for solar cells
C. Smit, B.A. Korevaar, A.M.H.N. Petit, R.A.C.M.M. van Swaaij, W.M.M. Kessels and M.C.M. van de Sanden, 29th IEEE Photovoltaic Spec. Conf., New Orleans, Louisiana (2002) 1170

Determining the material structure of microcrystalline silicon from Raman spectra
C. Smit, R.A.C.M.M. van Swaaij, H. Donker, A.M.H.N. Petit, W.M.M. Kessels and M.C.M. van de Sanden, J. Appl. Phys. **94** (2003) 3582

High-rate deposition of microcrystalline silicon with an expanding thermal plasma
C. Smit, A. Klaver, B.A. Korevaar, A.M.H.N. Petit, D.L. Williamson, R.A.C.M.M. van Swaaij and M.C.M. van de Sanden, Thin Solid Films **491** (2005) 280

External rf substrate biasing as a tool to improve the material properties of hydrogenated amorphous silicon at high deposition rates by means of the expanding thermal plasma
A.H.M. Smets, A.M.H.N. Petit, V. Nádazdy, W.M.M. Kessels, R.A.C.M.M. van Swaaij and M.C.M. van de Sanden, 31st IEEE Photovoltaic Spec. Conf., Orlando, Florida (2005) 1389

Improvement of the material properties by employing external RF substrate bias during a-Si:H deposition by a remote expanding thermal plasma
A.H.M. Smets, A.M.H.N. Petit, V. Nádazdy, W.M.M. Kessels, R.A.C.M.M. van Swaaij and M.C.M. van de Sanden, 20th European Photovoltaic Solar Energy Conf. and Exhib., Barcelona, Spain (2005) 1639

Acknowledgments

Here it is, the last page of my thesis. I wish to look back to the last years I spent in Dimes and to take the opportunity to thank all the people that contributed in one way or another to this work. Without them, I wouldn't have been able to carry out the work that led to this thesis.

First of all, I am grateful to Dr. René van Swaaij and Prof. Richard van de Sanden for their support throughout my whole Ph.D. project. René, I want to thank you for your supervising on a daily basis. Even if we didn't always agree, it led in fact to quite useful discussions. I thank you also for correcting my 'French-English' and for taking time to translate the summary and the propositions into Dutch. Richard, I really appreciated to work with you. Somehow you always managed to keep me on good tracks and boost up my motivation. Thank you for that.

I would also like to thank Professor Kees Beenakker for granting me a Ph.D. position in the Electronic Components, Technology and Material Laboratory. The well-equipped lab of Dimes offers a great opportunity to carry out research. Furthermore, I would like to thank my colleagues of the solar cell group: Wim Metselaar and Miro Zeman for the management of the group; Arjan Driessen and Martijn Tijssen for the technical support and for taking fast action when I ran in with: "the spectral response equipment is blocked!!" or "the turbo-pump is down again!!"; and of course the wise post-docs, Vojto and Raùl, and my fellow Ph.D. students, the 'old ones': Bas, Martin, Ad, Joost and Chiel - we had great scientific conversations! - and the 'new ones': Bart, Arjen, Gijs, Michael and Bas. In particular, I want to thank Arjen and Bart for our talks during the coffee breaks. I know much more about computers now than I ever dreamed of!

Much appreciation is also owed to the Equilibrium and Transport in Plasmas group of Eindhoven University. Besides Richard, I would like to thank Prof. Daan Schram

for being my second promoter, as well as Arno Smets, who played an important role in the completion of this project. Thanks for your patient explanations on plasmas, growth mechanism and rf-biasing. Furthermore, I want to thank Adriana for her friendship and Ries van de Sande and Herbert Fiedler for the technical support on the ETP set-up. I must give my special thanks to Dr. Gert-Jan Jongerden from Akzo Nobel and the whole Helianthos team for their collaboration over the past years. I acknowledge EET for supporting this work. I also thank members of my doctoral committee for taking the time out of their busy schedules to review this thesis, providing useful suggestions and comments on the manuscript.

Many thanks go to all my colleagues of the ICP-process group. You provided me with a pleasant research environment. In particular, I want to thank Tom for his good advices on chemicals handling and the relaxed coffee breaks, John, who unveiled to me the world of the clean room, Mario, for teaching me how to use the SEM, Cassan and Alex for helping me out with the 'Jipepech', Alfred for his positive spirit and technical skills, but also Jos, Charles, Jan G., Ruud, Lawrence, Kasper, Hugo, Wim vdV., Wim W., Peter, Henk and Bert for the good atmosphere. It would be a big omission to forget my room-mates Silvana and Loek; thank you for providing me with a nice working environment!

I would like to thank Dr. Harry Donker from the Faculty of Applied Sciences for performing Raman measurements and Dr. W. Arnold Bik from Utrecht University for the RBS measurements. I am grateful to Jelle, Marco, Jan W. and Peter for the general functioning of the labs. I won't forget the enthusiastic secretaries for assisting me with the administrative tasks: a special thank to Marian, Marysia and Jeanne.

I want to thank all the Ph.D. students and post-docs: Barry, Paul, Marcel, Artyom, Wibo, Léon, Nga, Hoa, Nebojsa, Alexander, Mark, Marco, Vittorio, Frederik, Qiwei, Vikas, Viktor, He Ming and the ones that I might have forgotten. I really enjoyed working in such an international group. Special thanks go to the 'French connection' of the university that prevented me from being homesick: Christophe, Charles, Frédéric, Séb, Xavier, Yann K. and Yann C. and also Gilles.

Moreover, I want to thank all my family and my friends for being there despite the distance. Papa, Maman, je crois qu'on peut dire que les petits cochons ne m'ont pas mangée finalement. Merci de m'avoir poussée, malgré ma paresse légendaire, et de m'avoir soutenue dans toutes mes entreprises. Cette thèse en fait partie. Merci de m'avoir permis de devenir la personne que je suis aujourd'hui.

Finally, I want to address a special thank to my husband Erik-Jan and our daughter Mathilde, for distracting me from my work, supporting me when my spirits were down and giving me so much love. This whole thesis couldn't have been completed without you.

Biography

Born in the south of France (Cavaillon, Vaucluse) in October 1975, Agnès Petit studied material science in Lyon at ISTIL (Claude Bernard University, France) from September 1993 to September 1998. She carried out her graduation project at Shell International Chemicals in the Shell Research and Technology Centre of Amsterdam (SRTCA), the Netherlands, where she worked on the optimisation of injection-moulding of Carillon polymer. End 1998, after obtaining her engineering degree (*Ingénieur en multimalteriaux et interfaces*), she came back to the Netherlands to join the Carillon group of Shell International Chemicals for an additional year and a half. During that period, she worked on hot-plate welding of the same Carillon polymer.

In August 2000, she joined the laboratory of Electronic Components, Technology and Materials of DIMES (Delft Institute of Microelectronics and Submicrontechnology), Delft University of Technology in the Netherlands, to work on the development of thin-film polycrystalline silicium deposited on heat-resistant substrates by AP-CVD (atmospheric pressure chemical vapor deposition) for solar-cell application within the European project SUBARO.

In January 2002, Agnès started research towards her Ph.D. degree at DIMES, Delft University of Technology. She focused her research on the deposition of hydrogenated amorphous silicon with an expanding thermal plasma (ETP) CVD technique, at high deposition rates (> 1 nm/s). Her work was part of the Helianthos project, which was a collaboration between Akzo Nobel, Shell Solar, Delft and Eindhoven Universities of Technology, Utrecht University and the research institute TNO-TPD. This project aimed to develop a-Si:H thin-film solar cells on flexible substrate in a roll-to-roll process. The results of this research are reflected in this thesis.

Besides her research, she actively took part in the organization of a symposium of the Microelectronics Ph.D. students' association MEST, on Space Electronics in 2002. In particular, she was responsible for finding sponsors and she arranged all financial aspects of the event. She was also involved in the MEST committee and controlled the budget balance of the association for three years.